Earth-Science Reviews 271 (2025) 105274

Contents lists available at ScienceDirect

Earth-Science Reviews

journal homepage: www.elsevier.com/locate/earscirev

Review Article

Planetary albedo and reflected shortwave flux: Basic characteristics, mechanisms of change and future projections

Ruixue Li [1], Bida Jian [1], Jiming Li [*], Jiayi Li, Zhenyu Cao, Yang Wang, Yuan Wang, Jianping Huang

Key Laboratory for Semi-Arid Climate Change of the Ministry of Education, College of Atmospheric Sciences, Lanzhou University, Lanzhou 730000, China

A R T I C L E I N F O

Keywords:
Planetary albedo
Reflected solar radiation
Hemispheric symmetry
Mechanisms of change
Future projection

A B S T R A C T

The Earth's planetary albedo (PA) and reflected solar radiation (RSR) are critical for energy distribution and variability, significantly influencing the climate system and its response to climate change. This review presents an updated assessment of the characteristics, mechanisms, model simulations, and future projections of PA and RSR, providing valuable insights into their implications for the Earth's climate system. We summarize the trends and long-term variations in PA/RSR and their key drivers. Over the past two decades, global mean PA/RSR has significantly decreased, exacerbating Earth's energy imbalance, which is attributed to reduced low/mid-level cloud cover in tropical and subtropical oceans, retreating snow/ice cover at high latitudes, and reduced aerosol scattering at Northern Hemisphere mid-latitudes. Note that cloud fraction dominates RSR variations in most areas, but snow/ice coverage plays a larger role in polar coastal regions. Furthermore, we review the potential mechanisms that maintain hemispheric PA symmetry, highlighting the combined effects of tropical cloud movement and asymmetries in extratropical baroclinic activities. By applying the emergent constraint method and observations, we reduce the uncertainty of future projected RSR by 76 %. We find a significant decline in both global and hemispheric RSR this century, with trends slowing under low and medium emission scenarios, but accelerating under high emission scenarios. Finally, we emphasize future challenges in paleoclimatic radiation studies and the need for accurate long-term radiation data, and we suggest that strategies like emission reductions and reforestation may be vital for stabilizing Earth's PA on a long-term scale.

Contents

* Corresponding author.
E-mail address: lijiming@lzu.edu.cn (J. Li).
[1] These authors contributed equally to this work.

https://doi.org/10.1016/j.earscirev.2025.105274
Received 29 November 2024; Received in revised form 23 August 2025; Accepted 9 September 2025
Available online 11 September 2025

1. Introduction

Solar energy, as the primary driving force of the Earth's climate system, profoundly influences atmospheric and oceanic circulation and energy transfer (Benestad, 2006). A portion of the globally averaged solar radiation incident at the top of the atmosphere (TOA) is reflected back into space, while the remainder is absorbed by the atmosphere and the Earth's surface. The Earth's planetary albedo (PA), which is defined as the ratio of reflected solar radiation (RSR) to incident solar radiation (ISR) at the TOA, is one of the key factors in regulating the absorption and distribution of solar energy (Fu et al., 2000; Stephens et al., 2015) and in determining the temperature of the atmosphere and the surface (Ångström, 1962). It also plays a crucial role in the Earth's energy balance and climate change (Wielicki et al., 2005; Stephens et al., 2015). For example, a 5 % change in PA can lead to an approximate 1 K change in global average temperature in the absence of climate feedbacks (North et al., 1981; Stephens et al., 2015); a change of 0.01 in PA can result in radiative forcing equivalent to a doubling of carbon dioxide concentration in the atmosphere (Wielicki et al., 2005; Bender et al., 2006; Shepherd, 2009; Kravitz et al., 2013; IPCC, 2021). Furthermore, based on a simplified energy balance model, even a change in PA of less than 0.02 units is sufficient to drive the development of Quaternary glaciations (Budyko, 1969; Donohoe and Battisti, 2011). Moreover, changes in PA can trigger chain reactions in the Earth-atmosphere system. For instance, variations in global albedo are directly linked to changes in global average temperature, which in turn determines the water vapor content in the atmosphere, subsequently influencing cloud distribution (Perkins, 2019). Changes in cloud cover then affect Earth's PA, creating a closed-loop system. Generally, PA results from the combined reflection of solar radiation by clouds, atmospheric gases, aerosols, land, and ocean surfaces. Conversely, PA also impacts these major interactive spheres of the Earth's climate system (Atmosphere, Hydrosphere, Lithosphere, Cryosphere, and Biosphere), which contain various complex climate feedback mechanisms.

1. Atmosphere: When solar radiation is incident on the atmosphere, a large proportion is scattered, absorbed, or reflected by atmospheric constituents, aerosols, and clouds (Liou, 1976; Lu and Khalil, 1996). The energy absorbed by the atmosphere ultimately regulates atmospheric temperature and regional energy balance, which in turn influences atmospheric circulation and climate patterns. Changes in albedo can alter land-sea temperature differences and modulate monsoon intensity and variability (Sud and Smith, 1985). In the atmosphere, clouds are the largest contributors to PA (Ramanathan et al., 1989; Donohoe and Battisti, 2011), and their variability involves complex radiative feedback mechanisms. These cloud feedbacks, whether positive or negative, are the primary source of spread among climate sensitivity in models (Ceppi et al., 2017; IPCC, 2021). For example, observational evidence indicates positive feedback in cloud albedo over the subtropical stratocumulus region of the northeastern Pacific. Here, increased sea surface temperatures (SSTs) lead to a reduction in low clouds, which in turn decreases regional albedo and further warms the ocean (Clement et al., 2009). Additionally, the interactions between clouds and aerosols influence each other's properties (Twomey, 1974; Twomey, 1977; Albrecht, 1989; Ackerman et al., 2004; Kuniyal and Guleria, 2019), thereby affecting the overall albedo.

2. Hydrosphere: By regulating surface temperature, PA indirectly influences evaporation and precipitation, thereby modulating the cloud formation and hydrological cycle (Wild and Liepert, 2010; Bala et al., 2011). A reduction in snow and ice cover can lead to increased absorption of solar radiation by water bodies (due to decreased albedo), which accelerates melting and raises sea level and river flow. The relatively low albedo of oceans allows them to absorb more solar radiation, which affects ocean temperatures and current patterns. Additionally, precipitation affects cloud thickness and thus cloud albedo by influencing the entrainment process (Pincus and Baker, 1994), and it can also suppress positive snow-albedo feedback, thereby increasing snow albedo in polar regions (Picard et al., 2012).

3. Lithosphere (Land surface): PA directly influences the amount of solar radiation received at the surface, which affects surface temperatures and subsequently impacts vegetation growth and land cover types, resulting in different surface albedo. Although the PA's direct impact on geological activity is limited, long-term climate changes related to changes in PA (such as glacial advances and retreats, and sea-level fluctuations) can indirectly affect surface stress distribution and shape geological patterns (Lambeck, 2004).

4. Cryosphere: Snow and ice have relatively high albedo, which largely determines the climate of the cryosphere and even affects global albedo and climate change. The albedo plays a crucial role in the energy balance and maintenance of the cryosphere (Hotaling et al., 2021). Changes in albedo are crucial for glacier melting (Box et al., 2012), as the decline in albedo due to melting ice and snow creates a positive ice-albedo feedback mechanism that accelerates the melting process, particularly in the Arctic (Kellogg, 1975; Screen and Simmonds, 2010; Jenkins and Dai, 2021), thus exacerbating regional warming.

5. Biosphere: Variations in PA affect temperature, light, and moisture conditions within the biosphere, influencing ecological processes such as vegetation growth and animal migration (Upadhyay, 2020; Zarnetske et al., 2021). A stable and suitable value of PA is crucial for maintaining Earth's habitability, holding immeasurable value for the survival and development of human society (Spiegel et al., 2008; Del Genio et al., 2019). Historically, albedo plays a significant role in maintaining warm climates, such as during the Cretaceous period (Thompson and Barron, 1981). Conversely, biological activities, particularly human activities such as industrial operations, urbanization, and agricultural expansion, significantly alter PA through changes in atmospheric composition and surface properties.

Clearly, there exists a dynamic relationship between global climate and PA. Given this, the analysis of PA has become a key tool for understanding global warming. However, the complex interactions of uncertain influencing factors, such as aerosols and clouds, pose challenges for current climate models in fully capturing the dynamic features of PA (Stephens et al., 2015; Perkins, 2019; Jian et al., 2020). Accurately monitoring the temporal and spatial variations in PA on both local and global scales is crucial for optimizing predictive models and forecasting future temperature changes and climate trends. Although the previous review by Stephens et al. (2015) has provided valuable insights, it is limited by the time span of the observational data. Moreover, many new discoveries and significant studies have emerged since then. In particular, the PA is currently experiencing a significant decline (Stephens et al., 2022; Li et al., 2024; Nikolov and Zeller, 2024), which contributes to the Earth's energy imbalance (EEI) and the ongoing increase in global temperatures (Trenberth and Fasullo, 2009; Loeb et al., 2021a; Raghuraman et al., 2021; Goessling et al., 2024; Hodnebrog et al., 2024; Loeb et al., 2024). Building on this foundation, Section 2 provides a comprehensive update of the distribution and variation characteristics of PA and RSR across multiple spatial and temporal scales in terms of overall, components and key features. A deep understanding of these features and their underlying influencing factors and mechanisms is essential for improving model accuracy. In Section 3, we systematically summarize the various atmospheric and surface factors affecting RSR and the potential maintenance and compensation mechanisms underlying the hemispheric symmetry of PA. The core objective is to strengthen predictive capabilities regarding future climate change, providing solid scientific support for the preservation of the human living environment. Following this logic, Section 4 focuses on the performance and improvements of climate models in simulating characteristics in PA and RSR. Based on the latest generation models from the Coupled Model Intercomparison Project Phase 6 (CMIP6), we predict the trajectories of RSR changes under different emission scenarios and employ emergent constraint methods to reduce the uncertainties in model predictions. Finally, this paper outlines several exploratory directions for future research of PA, aiming to promote continued advancement in this area.

2. Basic characteristics of PA and RSR

2.1. General characteristics and spatio-temporal variations of PA and RSR

2.1.1. Global and hemispheric characteristics

Since the early 20th century, scholars have employed various methods to estimate the magnitude of the Earth's PA, but their results exhibit large differences over time with considerable uncertainty (Hunt et al., 1986). However, the advancement of satellite remote sensing and its application in radiation observation since the 1960s has greatly improved the accuracy of PA estimation. In particular, the Earth Radiation Budget Experiment (ERBE), which involved instruments on three spacecraft, was the first multi-satellite system designed to measure the Earth's radiation budget (Barkstrom, 1984; Barkstrom and Smith, 1986), and it provided the first robust global estimates of cloud radiative effects (Ramanathan et al., 1989). Subsequently, with the increasing number and enhanced capabilities of on-orbit satellites, broadband, and multispectral sensors, various Earth's energy budget products have been generated (House et al., 1986; Stephens et al., 2015; Liang et al., 2019; Loeb et al., 2022). Among them, the Clouds and the Earth's Radiant Energy System (CERES) Energy Balanced and Filled (EBAF) radiant flux product (Kato et al., 2018; Loeb et al., 2018a) based on the CERES broadband scanning radiometer is an invaluable source of information for exploring the Earth's energy budget and climate change and is widely used for characteristics and mechanisms studies of PA and RSR (Voigt et al., 2013; Stephens et al., 2015; Jian et al., 2020; Datseris and Stevens, 2021; Jönsson and Bender, 2022; Stephens et al., 2022; Crueger et al., 2023).

The CERES instrument is onboard multiple satellites (TRMM, Terra, Aqua, Suomi National Polar-orbiting Partnership (Suomi NPP) and NOAA-20) operated by the National Aeronautics and Space Administration (NASA), and represents an improved and upgraded version of the Earth Radiation Budget Experiment radiometer (Wielicki et al., 1996; Loeb et al., 2018a). It consists of three spectral channels: shortwave (0.3–5 μm), window (8–12 μm), and total (0.3–200 μm). The CERES instrument first converts the received radiance from digital counts to calibrated "filtered" radiances. Next, these filtered radiances are adjusted to unfiltered radiances to account for the instrument's spectral response imperfections using time-dependent spectral response function values (Loeb et al., 2001) and in turn to instantaneous TOA radiative fluxes using empirical angular distribution models (ADMs) (Su et al., 2015). Finally, the instantaneous fluxes are averaged to daily fluxes by applying Sun-angle-dependent diurnal albedo models (Loeb et al., 2018a). The EBAF product provides global monthly average radiation flux data at a resolution of $1^\circ \times 1^\circ$ from March 2000 to the present, including observed TOA and computed surface longwave, shortwave, and net radiation fluxes under all-sky and clear-sky conditions, along with cloud parameters based on MODIS. Importantly, EBAF's TOA shortwave and longwave fluxes undergo energy balance adjustments

Table 1
Multi-year annual mean (Mean), detrended and deseasonalized monthly anomaly standard deviations (STD), and decadal trends (Trend) of ISR, RSR, and PA for the SH, NH, and globe based on CERES EBAF from January 2001 to December 2023.

		All-sky			Clear-sky		
		SH	NH	Global	SH	NH	Global
ISR	Mean (W m^{-2})	340.15	340.17	340.16	340.15	340.17	340.16
	STD (W m^{-2})	0.49	0.41	0.11	0.49	0.41	0.11
	Trend (W m^{-2} $decade^{-1}$)	0.03	0.03	**0.03**	0.03	0.03	**0.03**
RSR	Mean (W m^{-2})	98.90	98.92	98.91	50.64	56.88	53.76
	STD (W m^{-2})	0.91	0.82	0.55	0.46	0.56	0.33
	Trend (W m^{-2} $decade^{-1}$)	**−0.66**	**−0.90**	**−0.78**	**−0.14**	**−0.55**	**−0.34**
PA	Mean	0.291	0.291	0.291	0.150	0.167	0.158
	STD (10^{-3})	2.4	2.3	1.6	1.2	1.5	1.0
	Trend (10^{-3} $decade^{-1}$)	**−2.02**	**−2.65**	**−2.32**	**−0.26**	**−1.48**	**−1.02**

Note. **Bold** indicates trend is above the 95 % confidence level.

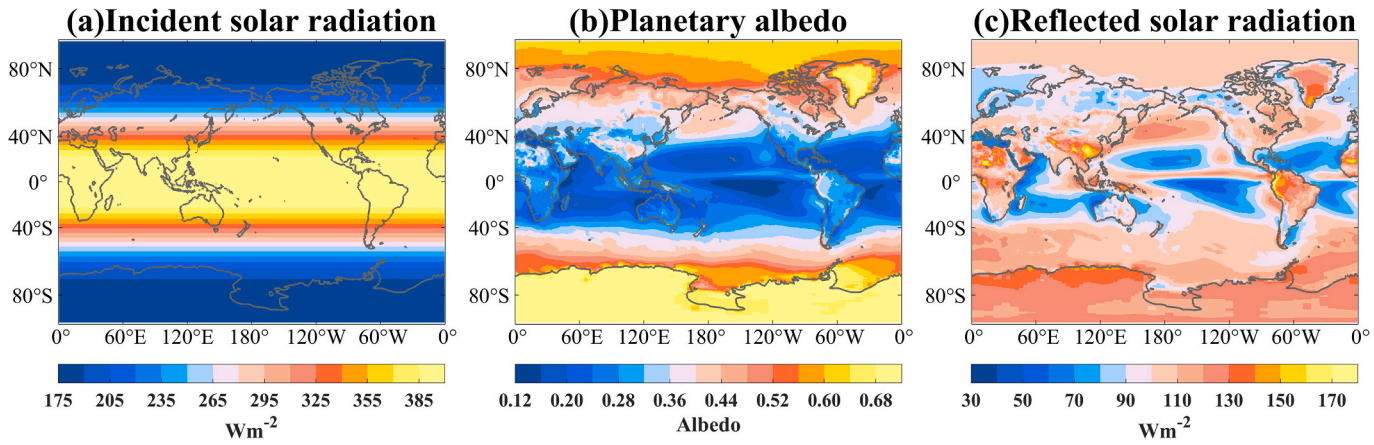

Fig. 1. Global distributions of the annual mean climatological (a) ISR flux, (b) PA, and (c) all-sky RSR flux.

within their uncertainty bounds based on ocean heat storage by using an objective constraint algorithm (Loeb et al., 2009). Surface fluxes are computed based on a radiation transfer model considering the state and composition of the atmosphere, surface, and ISR from reanalysis and satellites (Kato et al., 2018).

In this paper, the basic characteristics of PA and RSR are updated based on the latest version of the CERES EBAF ed4.2 product from January 2001 to December 2023 (23 full years) (Table 1). Note that annual averages for all variables are the sum of monthly averages weighted by the ratio of the number of days in each month to the total number of days in that year (Wielicki et al., 1996; Loeb et al., 2009), and regional averages are area-weighted (Li et al., 2024). Globally, 340.16 W m^{-2} of solar radiation enters the earth-atmosphere system, of which 98.91 W m^{-2} is reflected into cosmic space under all-sky conditions, resulting in a multi-year average PA of 0.291. Under clear-sky conditions, the RSR flux is 53.76 W m^{-2}, with an albedo of 0.158, which is nearly half of the all-sky value, indicating a significant contribution of clouds. From a hemispheric perspective, it is interesting to note that the all-sky PA exhibits hemispheric symmetry (Vonder Haar and Suomi, 1971; Ramanathan, 1987; Zhang and Rossow, 1997; Stevens and Schwartz, 2012; Voigt et al., 2013; Stephens et al., 2015; Datseris and Stevens, 2021; Jönsson and Bender, 2022; Jönsson and Bender, 2023; Li et al., 2024), with a value of 0.291 for both hemispheres. The annual average ISR (RSR) at the TOA is 340.17 (98.92) W m^{-2} for the Northern Hemisphere (NH) and 340.15 (98.90) W m^{-2} for the Southern Hemisphere (SH). This symmetry is surprising, given that the hemispheric differences in clear-sky PA and RSR reach 0.017 and 6.24 W m^{-2}, respectively. The characteristics and potential mechanisms of this hemispheric symmetry are reviewed and discussed in detail in Sections 2.3 and 3.2.

Fig. 1 provides the climatological spatial patterns of annual averaged ISR, all-sky RSR, and their ratio, known as PA. As shown in Fig. 1a, the ISR has a latitude-dependent spatial pattern, decreasing from the equator to the poles and remaining nearly uniform at the same latitude. However, the distribution of land, sea, vegetation, clouds, and aerosols, which have different characteristics and albedo values, leads to large regional differences in PA (Fig. 1b). Low albedo values are typically found in low-latitude seas, while high values are observed in ice/snow-covered high-latitudes or cloudy low/mid-latitudes (Bender et al., 2006). Most areas between 40°N and 40°S have an albedo less than 0.32, except for regions such as northern Africa, the Tibetan Plateau (TP), southern China, and northwest South America, where PA exceeds 0.36. A distinct "bright band" exists over the equatorial Pacific, where cloud systems in the Intertropical Convergence Zone (ITCZ) exhibit higher albedo than the surrounding ocean surface. In the mid to high latitudes, areas with snow cover and sea ice can have PA values exceeding 0.44, especially in Greenland and Antarctica, where PA even exceeds 0.68 due to the extensive ice sheets. The spatial distribution of RSR (Fig. 1c) is influenced by both PA and ISR patterns. For example, although the PA is higher in the Arctic than in most mid- to low-latitude areas, RSR values are comparable due to lower ISR levels in the Arctic.

2.1.2. *Diurnal variation*

The diurnal variation in the absorbed solar radiation, which is controlled by the ISR and modulated by the PA, drives diurnal cycles of local circulations and other processes. It has been noted that neglecting the diurnal cycle due to the incomplete sampling of sun-synchronous orbit satellites could result in an approximately 1 % reduction in the global mean reflected shortwave flux at the TOA (Doelling et al., 2013). Therefore, it is necessary to pay attention to the diurnal variation characteristics of PA and RSR and their drivers. Previously, Briegleb and Ramanathan (1982) constructed a radiative transfer model and pointed out that the clear-sky PA over two tropical grids exhibit a U-shaped diurnal cycle during July, showing symmetry around noon. This pattern is influenced by the diurnal variation of the solar zenith angle (SZA), which has a more pronounced impact on the ocean than on land. However, the diurnal variation of all-sky PA is not only governed by the SZA cycle but also affected by the diurnal variations in atmospheric, cloud, and surface properties. Rutan et al. (2014) conducted a principal component (PC) analysis of five-year radiation measurements from the Earth Radiation Budget Satellite to examine the diurnal cycle characteristics of albedo between 55°N and 55°S. The first PC of the diurnal variation in albedo exhibits a minimum value around noon, displaying a symmetrical pattern about midday and accounting for 90 %–92 % (84 %–89 %) of the variance in albedo over the ocean (land). This statistical result indicated that the diurnal cycle of albedo is primarily driven by its dependence on SZA and also encompasses the diurnal variation of clouds. The strong dependence of TOA albedo on the SZA can be well reflected in empirically based ADMs (Loeb et al., 2003; Su et al., 2015). In general, larger SZAs imply that solar radiation undergoes longer extinction paths and more scattering, leading to higher observed albedo (Cronin, 2014; Gristey et al., 2018; Balmes and Fu, 2020). In addition, at large SZAs, the forward-peaked scattering phase function of cloud particles and aerosols causes a greater fraction of the scattered radiation to be directed upwards, further contributing to increased albedo (Boucher, 1998). Furthermore, diurnal variations in cloud properties, especially cloud fraction (CF) (Bergman and Salby, 1997), cloud water, and cloud height (Gristey et al., 2018), significantly affect the diurnal changes in PA and RSR. Ignoring these variations can introduce substantial errors in radiative forcing calculations within model simulations (Wilson and Mitchell, 1986; Rozendaal et al., 1995; Yin and Porporato, 2017).

Although the sampling by polar-orbiting satellites is instantaneous, the differences in data collected at various fixed times can partially reflect the diurnal variations of PA and RSR. Specifically, the differing

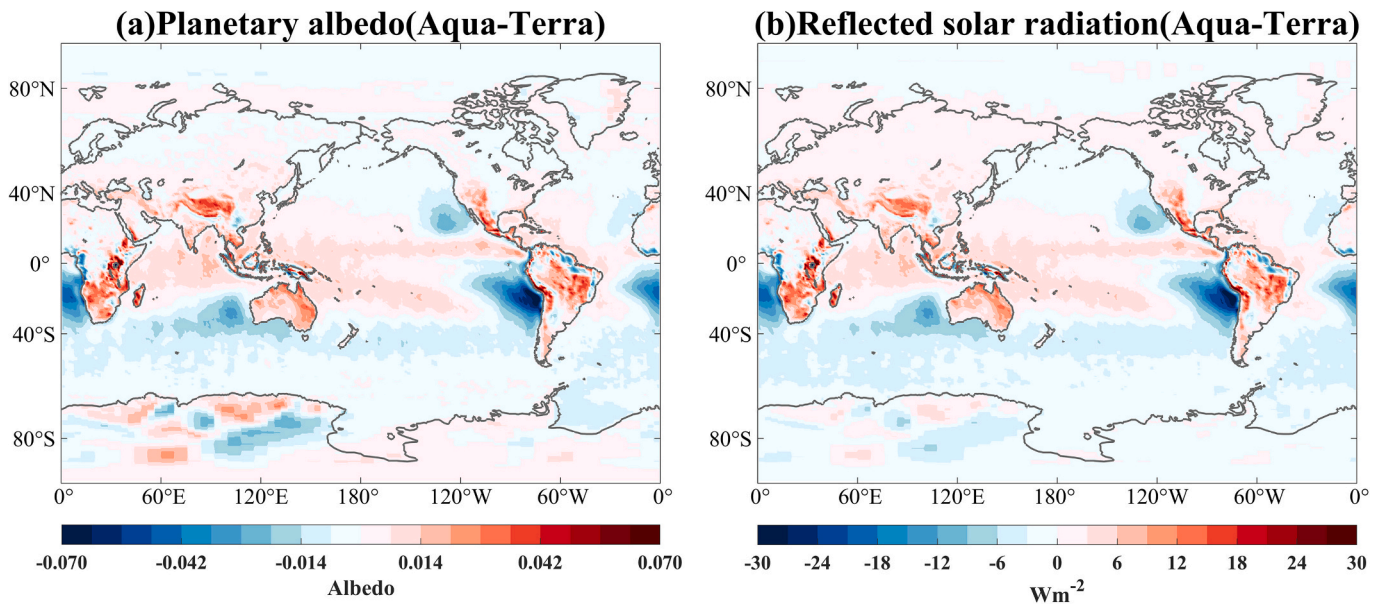

Fig. 2. Global distributions of the annual mean differences of (a) PA and (b) RSR between Aqua and Terra based on CERES_SSF1deg Ed4.1 for 2003–2022. [Adapted from Jian et al., 2018]. (For interpretation of the references to colour in this figure legend, the reader is referred to the web version of this article.)

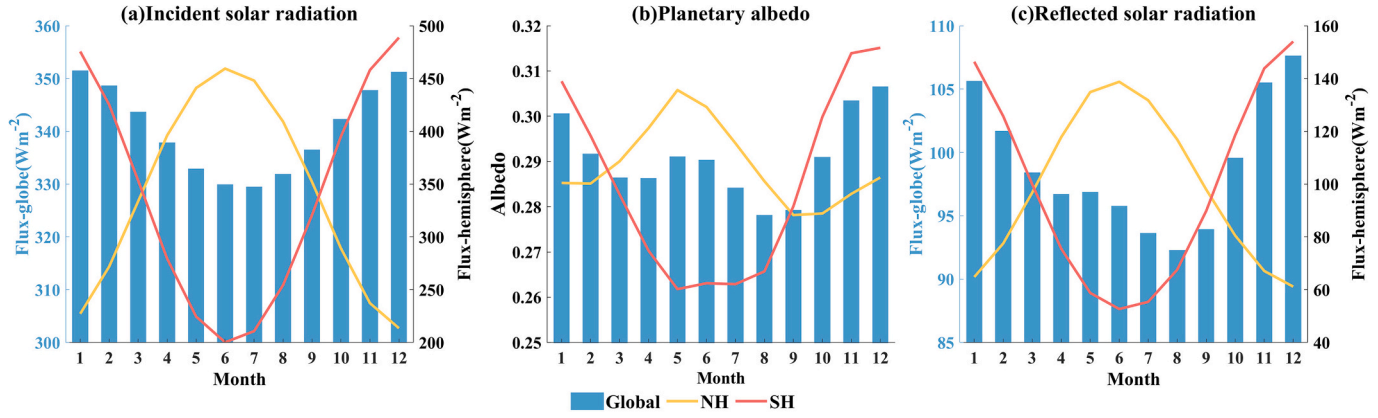

Fig. 3. Annual cycles of (a) ISR, (b) PA, and (c) RSR for the globe (blue bars), NH (yellow lines), and SH (red lines). Please note that the global average fluxes in panels a and c correspond to the left y-axis, while the hemispheric average fluxes correspond to the right y-axis. (For interpretation of the references to colour in this figure legend, the reader is referred to the web version of this article.)

overpass times of Terra and Aqua enable us to highlight the difference between PA at two moments of the day by comparing the data from these two satellites. The CERES Single Scanner Footprint 1° (SSF1deg) products are processed separately for each satellite: Terra (available from March 2000 to April 2024) orbits in a descending sun-synchronous path, crossing the equator at 10:30 AM local time, while Aqua (available from July 2002 to February 2023) follows an ascending path, crossing at 1:30 PM local time. To address sampling gaps, daily average fluxes are calculated from instantaneous measurements using an empirical daily albedo model, which assumes constant scene properties throughout the day (Loeb et al., 2003; Doelling et al., 2013; Loeb et al., 2018a). Following Jian et al. (2018), we illustrate the global distribution of the annual average PA and RSR differences between Aqua and Terra from 2003 to 2022 based on CERES_SSF1deg Ed4.1 data (Fig. 2). The results indicate that, in most regions, the difference in PA between morning and afternoon typically falls within ±0.01, with larger variations observed between 40°N and 40°S. Over some typical marine stratocumulus regions, such as Namibian, Australian, and Peruvian, PA is observed to be lower in the afternoon than in the morning, which can be attributed to the differences in the cloud macro-properties (Jian et al., 2018). Indeed, previous studies have indicated that the amount of stratocumulus clouds decreases from dawn to afternoon (Klein et al., 1995; Garreaud and Muñoz, 2004). Conversely, afternoon increases in cloud albedo forcing (CAF) (Jian et al., 2018), which may be associated with enhanced afternoon convection over land (Cairns, 1995; Yang et al., 2004; Hong et al., 2006; Protat et al., 2010) or increased CF and ice water path (IWP) (Jian et al., 2018), may explain why PA is higher in the afternoon than in the morning over southern Africa, the TP, Australia, tropical rainforests, northern South America, and the western United States. The distribution of RSR difference between afternoon and morning (Fig. 2b) is quite similar to that of PA (Fig. 2a), with only slight variations observed in regions such as northern Eurasia and Antarctica, which may be influenced by the different ISR at two times. Moreover, the differences over high latitudes appear slightly less pronounced in RSR than in PA, which could be attributed to the annual mean ISR being lower at high latitudes compared to the tropics.

2.1.3. *Annual cycle*

The tilt of the Earth's axis and its orbit around the Sun creates a pronounced seasonal cycle in the TOA ISR. Seasonal changes in

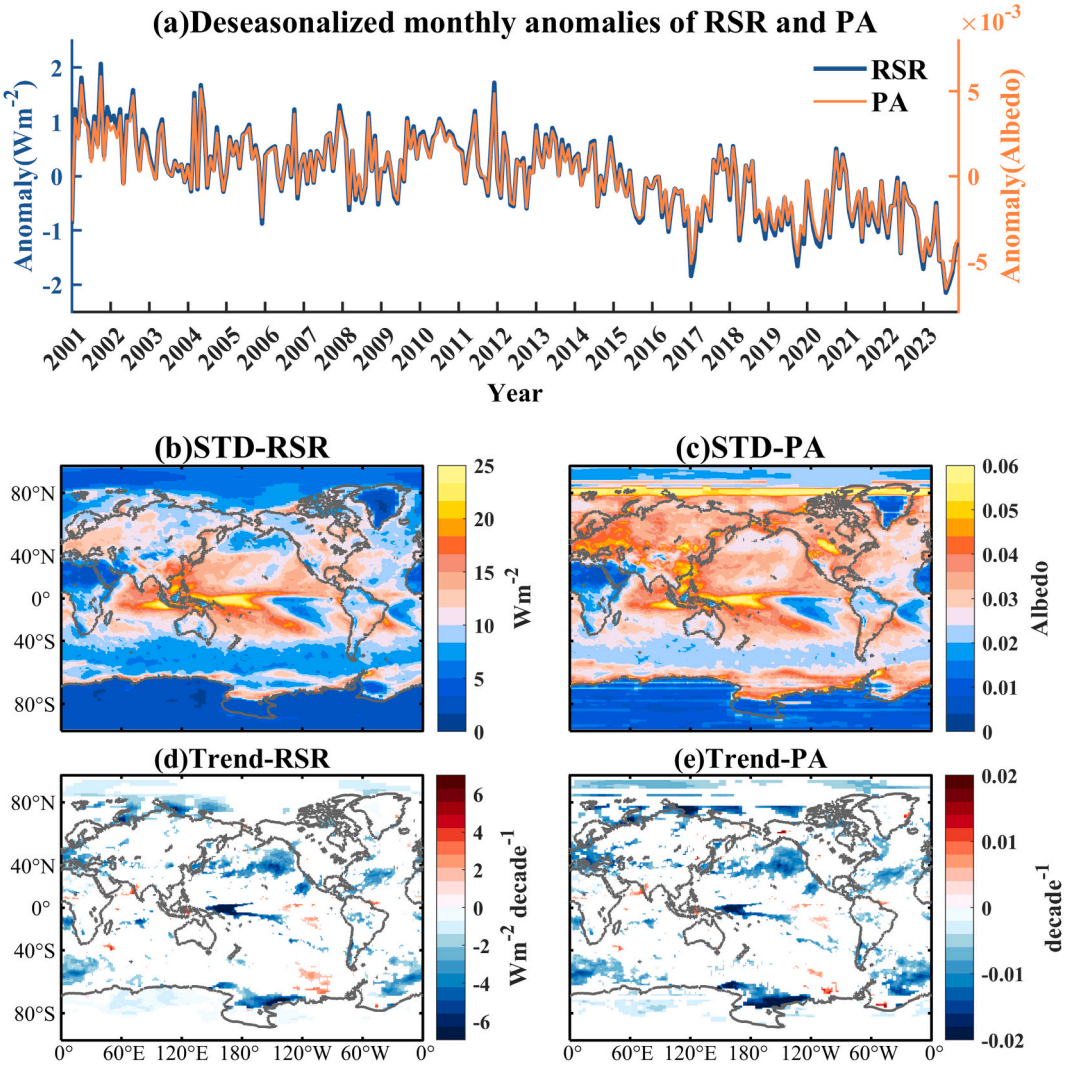

Fig. 4. (a) Deseasonalized monthly anomalies in global mean TOA RSR flux (blue line) and PA (orange line). The global distribution of the (b-c) detrended STD and (d-e) long-term trends in RSR and PA on a 1° × 1° latitude/longitude scale. Grid boxes with shading in panels (d) and (e) indicate the trend is significant at the 95 % confidence level. (For interpretation of the references to colour in this figure legend, the reader is referred to the web version of this article.)

atmospheric and surface properties lead to variations in PA, which in turn result in distinct annual patterns in RSR that directly influence energy distribution. The annual cycles of the global and hemispheric mean ISR, PA, and RSR are shown in Fig. 3. The average ISR in both hemispheres shows a single-peak structure with high summer and low winter, but the low values are lower in the SH (Fig. 3a). Moreover, the global average ISR exhibits a U-shaped annual cycle, with a minimum occurring in July, due to the largest Earth-Sun distance. The SH's mean PA also shows a single-peak annual cycle, with the minimum value in May and the maximum value in December (Fig. 3b). In contrast, the annual cycle of PA in NH has two peaks, featuring a prominent peak in May and a smaller one in December, with its minimum in September. Notably, the SH's maximum value is about 0.01 higher, while its minimum is 0.02 lower than those in the NH. Thus, the global mean PA displays a distinct double-peaked pattern (Bender et al., 2006; Loeb et al., 2007; Kato, 2009; Jian et al., 2020), with peaks in May and December that correspond to the maximum albedo in the NH and SH, respectively. These peaks may be related to the higher albedo of ice-covered areas at high latitudes during the sunlit season (Bender et al., 2006), as well as increased cloud cover during summer months. The annual cycle of RSR is primarily shaped by the ISR (Stephens et al., 2015; Li et al., 2024), whereas local variations in atmospheric and surface properties have a secondary effect. As a result, the hemispheric averaged RSR shows a single-peaked structure and the global mean RSR exhibits a similar but less pronounced double-peaked annual cycle pattern to that of global mean PA (Fig. 3c). The comparison of the annual cycles of radiation flux and albedo reveals that the annual cycle of ISR has a greater impact on RSR during the winter in the NH. Moreover, it is necessary to explore the annual cycle characteristics of PA and RSR on a regional basis to reveal some of the signals that are easily masked. Li et al. (2024) decomposed the annual cycle of RSR and PA over different latitudinal zones (10° intervals) and found clear monthly variations with a single peak, typically reaching maximum values in June/July for the NH and in December/January for the SH.

2.1.4. *Interannual variability and trends*

Previous studies based on shorter observational records have revealed a small interannual variability in PA and RSR on both global and annual scales (Kato, 2009; Stephens et al., 2015; Stephens et al., 2022), as well as within latitude zones (Stevens and Schwartz, 2012). Especially, given that the global mean albedo is the main determinant of surface temperature, Bender et al. (2006) argued that the relatively stable global average surface temperature during the Holocene climate suggests that the PA also remains stable. To quantify interannual variability, the standard deviation (STD) of the deseasonalized monthly series has been employed (Kato, 2009; Stephens et al., 2015). Fig. 4a

presents the deseasonalized monthly anomalies in global mean RSR flux and PA. In this study, given the significant changes in PA and RSR over the past two decades, we use the STD of the detrended monthly anomalies in PA and RSR to quantify their interannual variability. The detrended STDs of the global mean PA and RSR are 1.6×10^{-3} and 0.55 Wm^{-2}, respectively, which are only 0.56 % of the global averages (Table 1). Moreover, the STDs during the first and second decades of the 21st century are very similar, indicating that the interannual variability of PA and RSR has remained quite stable on a global scale. Regionally, the interannual variability in RSR (Fig. 4b) is remarkably large over oceans, especially over the tropical western and central Pacific, the tropical Indian Ocean, eastern Asia, and the South Atlantic near the eastern coast of South America. Additionally, considerable interannual variability in PA (Fig. 4c) is also observed in continental areas north of 40°N and along the Antarctic coast. In contrast, regions with very stable interannual variations in RSR and PA are concentrated in northern Africa, Greenland, and Antarctica.

Using the least squares method to fit the deseasonalized monthly RSR anomalies from 2001 to 2023, we observe a trend of −0.78 W m^{-2} $decade^{-1}$ for global mean RSR (Table 1). Given the relatively stable ISR, which even shows a positive trend of 0.03 W m^{-2} $decade^{-1}$ due to the near-maximum intensity of the 11-year solar cycle (Kopp, 2016; Goessling et al., 2024), the decline in RSR can be attributed to a reduction in PA of -2.32×10^{-3} $decade^{-1}$. In 2023, the annual mean PA is only 0.286, marking the lowest value recorded since 2001 (Goessling et al., 2024). Furthermore, the decline in RSR and PA is faster in the NH compared to the SH, especially under clear-sky conditions. Fig. 4d and e further illustrate the long-term trend distributions of RSR and PA at a 95 % confidence level, which are nearly identical, with most of the significant trends over oceans. Significant decreasing trends are observed in the western tropical Pacific, northeastern Pacific, northern Pacific, western Europe, eastern Asia, parts of the Arctic, certain areas of the Southern Ocean, and eastern Antarctica. Conversely, sporadic increases are observed in western India, the southeastern Pacific, and the Southern Ocean south of the Pacific. We provide a detailed attribution of these trends in section 2.2.2.

It is reminded that the above foundational characteristics of the PA and RSR, including the climatology, spatial distributions, and variability across different time scales, are derived from CERES observations. In Section 4.1, we further review the reproduction of these features by the model simulations.

2.2. Decomposition of PA and RSR

2.2.1. A simple radiation model

To deeply analyze the specific effects of various factors on the RSR or the PA, it is particularly important to accurately distinguish the individual contributions of the atmosphere, clouds, and the surface. Until now, scholars have provided different decomposition methods based on various assumptions in single-layer solar radiation transfer models. Taylor et al. (2007) assumed that absorption by the atmosphere occurs only during the first downward passage of ISR through the atmosphere (after which it is assumed that the energy in the spectral bands where significant absorption occurs has been largely depleted). Subsequently, Donohoe and Battisti (2011) constructed a model that also simplified the atmosphere into a single-layer system, considering only three isotropic and proportionally fixed processes: atmospheric absorption (*a*: the percentage of absorption during each pass through the atmosphere), atmospheric reflection (*r*: the percentage of reflection during each pass through the atmosphere), and surface reflection. After the solar radiation reaches the TOA, it undergoes these processes an infinite number of times, with a portion of it eventually being reflected into space. After derivation, the RSR at TOA can be decomposed into atmospheric contribution $F^{\uparrow}_{atm}$ and surface contribution $F^{\uparrow}_{surf}$ (unit: W m^{-2}).Stephens et al. (2015) also regarded the atmosphere as a single absorbing and scattering layer above a reflective surface and linked the characteristics of the atmosphere to the radiative fluxes at the TOA and the surface. This model does not specify the absorption rate of the single-layer atmosphere *a*, but rather defines the intrinsic reflectance *r* and transmittance *t* of the atmosphere. In practice, the layer absorption $a = 1\text{-}r\text{-}t$, so their decomposition is consistent with that of Donohoe and Battisti (2011), with only a difference in the form of expression.

For ease of calculation, the atmospheric and surface contributions, expressed only in terms of the known TOA and surface shortwave radiative fluxes, can be expressed as:

$$F^{\uparrow}_{atm} = \frac{S\left(SF^{\uparrow}_{TOA} - F^{\uparrow}_{S}F^{\downarrow}_{S}\right)}{S^2 - F^{\uparrow 2}_{S}} \tag{1}$$

$$F^{\uparrow}_{surf} = F^{\uparrow}_{TOA} - F^{\uparrow}_{atm} = F^{\uparrow}_{TOA} - \frac{S\left(SF^{\uparrow}_{TOA} - F^{\uparrow}_{S}F^{\downarrow}_{S}\right)}{S^2 - F^{\uparrow 2}_{S}} \tag{2}$$

The incident solar radiation at the TOA (S), the RSR ($F^{\uparrow}_{TOA}$), and the upwelling and downwelling shortwave radiation fluxes at the surface ($F^{\uparrow}_{S}$ and $F^{\downarrow}_{S}$) are all provided by CERES EBAF. The derivation of these simplified expressions from the foundational formulas in Stephens et al. (2015) is provided in Appendix A.

These formulations can also be applied to clear-sky conditions, from which the clear-sky surface and atmospheric contributions can be decomposed ($F^{\uparrow}_{surf,clear}$ and $F^{\uparrow}_{atm,clear}$). Note that the clear-sky TOA and surface fluxes from CERES EBAF ed4.2 used in this study are determined for the entire region instead of cloud-free portions of a region. The clear-sky fluxes over a grid box are calculated using a radiative transfer model where clouds are removed from the atmospheric column (Loeb et al., 2020a), which are more consistent with how clear-sky fluxes are represented in the climate models. On this basis, the cloud contribution can be separated from the all-sky atmospheric contribution. The difference between the all-sky atmospheric contribution $F^{\uparrow}_{atm}$ and the clear-sky atmospheric contribution $F^{\uparrow}_{atm,clear}$ is considered as the cloud contribution $F^{\uparrow}_{cloud}$. That is,

$$F^{\uparrow}_{TOA} = F^{\uparrow}_{atm} + F^{\uparrow}_{surf} = F^{\uparrow}_{cloud} + F^{\uparrow}_{atm,clear} + F^{\uparrow}_{surf} \tag{3}$$

$$F^{\uparrow}_{cloud} = F^{\uparrow}_{atm} - F^{\uparrow}_{atm,clear} \tag{4}$$

It is crucial to recognize that this approach relies on the simplification that atmospheric absorption and reflection are equivalent for both downward and upward radiation. In reality, there is less absorption of upward radiation as highly absorbing wavelengths are consumed during downward transmission (Taylor et al., 2007). The impact of this approximation is complex and might be particularly problematic in regions with high surface albedo, where downward and upward radiation terms are of similar magnitude. As a result, some uncertainties, especially in polar regions, partly stem from the inherent limitations of this decomposition method. Nonetheless, due to its simplicity and practicality, this simplified model has been widely used in the study of RSR characteristics, providing a powerful tool for a deeper understanding of the impact of the atmosphere, clouds, and surface on the PA (Loeb et al., 2019; Jönsson and Bender, 2022; Lv et al., 2022; Stephens et al., 2022; Li et al., 2024).

In the following analysis, we decompose the RSR at TOA under all-sky conditions using Eq. 3. The decomposition is expressed in terms of three components: cloud component ($F^{\uparrow}_{cloud}$), clear-sky atmospheric component ($F^{\uparrow}_{atm,clear}$), and surface component ($F^{\uparrow}_{surf}$). It is important to note that although the clear-sky atmospheric component is derived from RSR under clear-sky conditions, it represents a portion of the all-sky contribution, reflecting the impact of a cloud-free atmosphere on the all-sky RSR.

Table 2
Multi-year annual mean (Mean), detrended and deseasonalized monthly anomaly standard deviations (STD), and decadal trends (Trend) of clear-sky atmospheric, surface, and cloud components of RSR and PA for the SH, NH, and globe based on CERES EBAF Ed4.2 from January 2001 to December 2023.

		Clear-sky atmosphere			Surface			Cloud		
		SH	NH	Global	SH	NH	Global	SH	NH	Global
RSR	Mean ($W\ m^{-2}$)	31.07	34.95	32.98	11.56	13.41	12.49	56.27	50.56	53.44
	STD ($W\ m^{-2}$)	0.33	0.52	0.31	0.28	0.3	0.19	1.01	0.86	0.62
	Trend ($W\ m^{-2}\ decade^{-1}$)	**0.14**	**−0.22**	−0.05	**−0.09**	**−0.14**	**−0.12**	**−0.73**	**−0.55**	**−0.62**
PA	Mean	0.091	0.103	0.097	0.034	0.040	0.037	0.165	0.149	0.157
	STD (10^{-3})	0.97	1.44	0.90	0.69	0.81	0.57	2.78	0.41	1.81
	Trend ($10^{-3}\ decade^{-1}$)	**0.43**	**−0.53**	−0.15	**−0.20**	**−0.39**	**−0.34**	**−2.30**	**−1.71**	**−1.85**

Note. **Bold** indicates trend is above the 95 % confidence level.

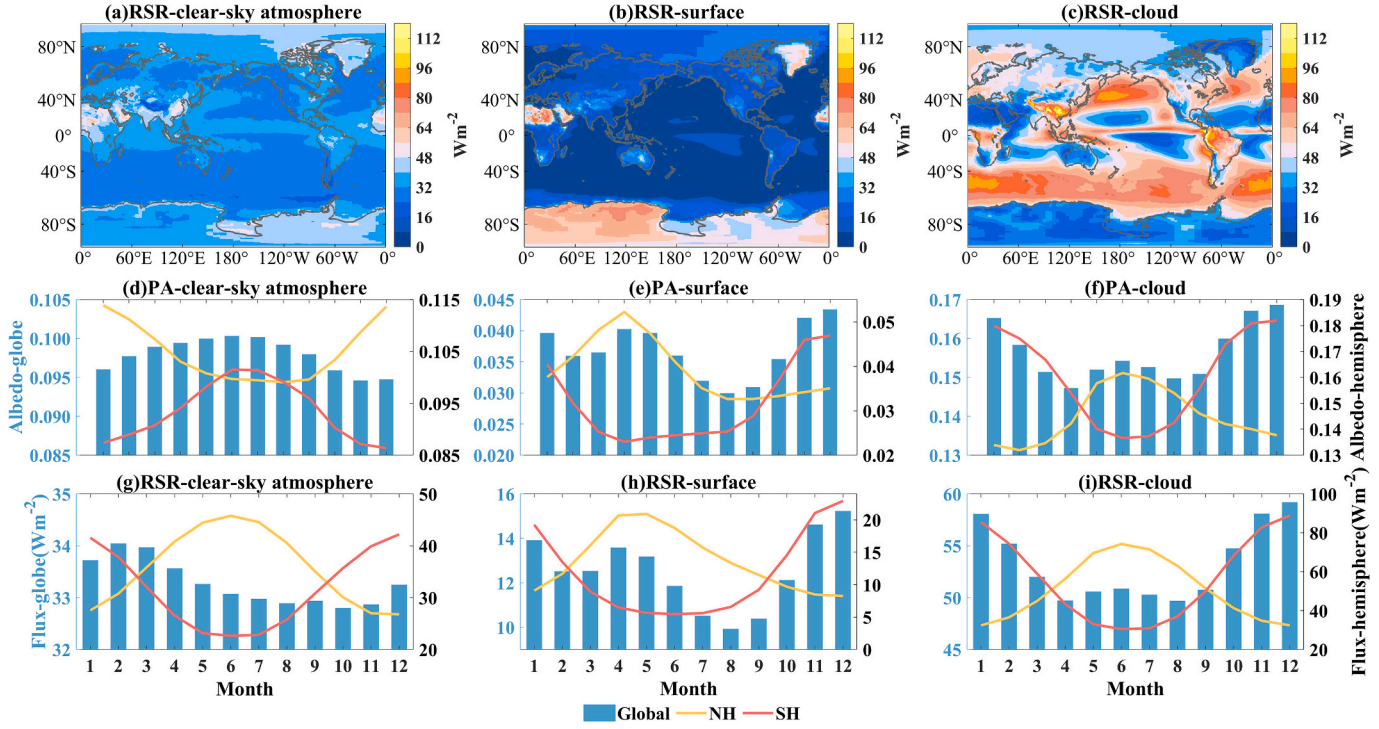

Fig. 5. Global distributions of the annual mean climatological (a) clear-sky atmospheric, (b) surface, and (c) cloud components. (d-i) Annual cycles of global (blue bar), SH (red line), and NH (yellow line) average clear-sky atmospheric components (left), surface components (middle), and cloud components (right) of PA and RSR, respectively. Please note that the global average corresponds to the left y-axis, while the hemispheric averages correspond to the right y-axis. (For interpretation of the references to colour in this figure legend, the reader is referred to the web version of this article.)

2.2.2. Contributions of clear-sky atmosphere, surface, and cloud and their variability

The statistical results of the climatology and variations of different components of PA and RSR are presented in Table 2. From 2001 to 2023, the global annual mean all-sky RSR flux is 98.91 W m^{-2}, with the cloud component contributing over 50 % (about 53.44 W m^{-2}). The contributions from the clear sky atmosphere and surface are 32.98 W m^{-2} and 12.49 W m^{-2}, respectively. As the global average PA is 0.291, the cloud, clear sky atmosphere, and surface components contribute 0.157, 0.097, and 0.037, respectively. As expected, even though the PA and total RSR are nearly the same between the two hemispheres, the contributions from different components vary obviously with the hemispheres. In particular, the clear-sky atmospheric and surface components in the NH are higher than those in the SH, thus effectively compensating for the lower contribution of the cloud component in the NH compared with that of SH (Voigt et al., 2013; Stephens et al., 2015).

Fig. 5 (a-c) further illustrates the regional distribution of the climatological contributions from the three components of RSR. The clear-sky atmospheric component generally ranges from about 24 to 40 W m^{-2} across most of the globe (Fig. 5a). Low values, around 16 to 32 W m^{-2}, are observed over the TP and the Southern Ocean south of South America. Over the TP, this can be attributed to both the reduced atmospheric mass at high elevations (leading to weaker Rayleigh scattering) (Tomasi et al., 2010) and relatively clean atmospheric conditions. The low values over the Southern Ocean are primarily associated with low aerosol loading. In contrast, regions with abundant dust aerosols, such as northern Africa, the Arabian Peninsula, and Central Asia (Kahn and Gaitley, 2015), areas rich in mixed aerosols, such as eastern and southern China (Tie and Cao, 2009) and India (Dey and Di Girolamo, 2011; Krishna Moorthy et al., 2013), as well as regions with frequent biomass burning, such as the Amazon (Reddington et al., 2019), experience clear-sky atmospheric components exceeding 40 W m^{-2} and even reaching 64–72 W m^{-2}. Surprisingly, in Greenland and West Antarctica, clear-sky atmospheric components reach 40–48 W m^{-2}, second only to the surface component (Fig. 5b) and exceeding the cloud component (Fig. 5c). On the one hand, the larger SZA at high

latitudes, combined with the large amount of upward shortwave radiation due to high surface albedo, leads to a longer atmospheric extinction path; on the other hand, the passive satellites have difficulties in distinguishing between snow and optically thin clouds, which may mislead the calculation of the clear-sky SW fluxes. Furthermore, the assumptions inherent in the component decomposition method concerning atmospheric absorption and reflection may contribute to uncertainties in component estimates over high-albedo areas. Moreover, since the subvisual clouds with optical depths less than ~0.3 frequently occur over tropical oceans and are generally not detected by MODIS (Minnis et al., 2008; Sun et al., 2011), some scenes containing these clouds might be misclassified as clear, potentially introducing errors in the radiative fluxes. However, the CERES EBAF clear-sky fluxes used in this study are computed using a radiative transfer model where clouds are removed from the atmospheric column (Loeb et al., 2020a, 2020b), so this misclassification may not substantially impact the RSR decompose. The spatial distribution of the surface component (Fig. 5b) typically shows larger contributions over land than over ocean, with significant high values in exposed areas, such as the Sahara and Saudi Arabia, as well as in snow/ice-covered regions such as Greenland and Antarctica. Over oceans, particularly at low and mid-latitudes, the surface component often remains below 8 W m^{-2} due to lower surface albedo and extensive cloud cover. However, in regions with minimal cloud cover, such as the tropical southeastern Pacific, the surface component is larger compared to the surrounding area. The cloud component dominates the total RSR over most of the oceans, as well as over Asia, Europe, and the Americas (Fig. 5c), with notable high values in mid-latitude storm tracks, the ITCZ, the TP, southern China, southern tropical Africa, and northern South America. Meanwhile, it is important to note that in areas with high cloud components, the other two components are generally lower. This is due to the masking effect of clouds (Qu and Hall, 2005; Donohoe and Battisti, 2011; Voigt et al., 2014; Stephens et al., 2015; Stephens et al., 2016; He et al., 2019), which limits the potential contributions and variability of the surface and aerosol to the total RSR. This masking effect is particularly pronounced in areas with high surface reflectivity, such as the cryosphere. According to Stephens et al. (2015), clouds can reduce the surface contribution to the RSR at the TOA by approximately 50 % in high-latitude regions.

Fig. 5 (d-i) further decompose the annual cycles of PA and RSR into three components. There are marked differences in the annual cycle of the global averaged clear-sky atmospheric components between radiation flux and albedo (Fig. 5d and g), with single peaks in February and June, respectively. Additionally, the hemispheric average clear-sky atmospheric contributions to PA exhibit a reversed pattern compared to RSR. For the clear-sky atmospheric component of PA, the peaks in both hemispheres occur in winter (Fig. 5d), likely due to increased atmospheric extinction from anthropogenic sulphate emissions, biomass burning, dust storms, and more sea-salt aerosols amplified by increased winter wind speeds (Gui et al., 2021a). Moreover, the larger SZA in winter allows for longer extinction paths, which may lead to greater clear-sky atmospheric reflections. In contrast, for the clear-sky atmospheric component of RSR, the peak in both hemispheres is in summer (Fig. 5g). This is because ISR is much larger in summer than in winter, and this seasonal difference outweighs the opposite seasonal difference in albedo, resulting in higher radiative fluxes in summer. The surface and cloud components display similar double-peak patterns in their global mean albedo and radiation flux (Fig. 5e, f, h, i). The surface component peaks in April and December, corresponding to the maxima in NH and SH, respectively (Fig. 5e, h). Meanwhile, the cloud component peaks in June and December (Fig. 5f, i). Together with Fig. 3b and c, these results indicate that the seasonal variability of global PA and RSR is predominantly influenced by the surface and cloud components. Similarly, at the hemispheric scale, in the NH, the PA does not peak in April (Fig. 3b) despite a peak in the surface component (Fig. 5e), because

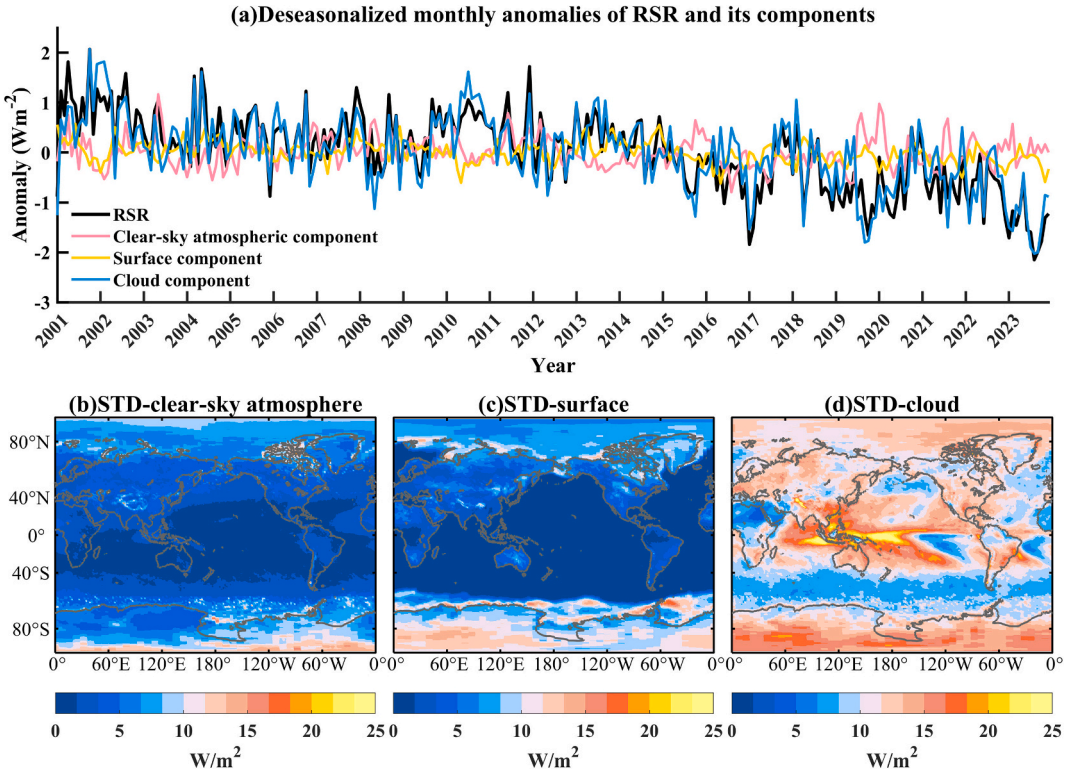

Fig. 6. Deseasonalized monthly anomalies in global mean RSR (black line) and its clear-sky atmospheric (pink line), surface (yellow line), and cloud (blue line) components (Similar to Lv et al. (2022), which separated the anomalies of PA into atmospheric and surface contributions). (b-d) The global distribution of the detrended STD in three components of RSR. (For interpretation of the references to colour in this figure legend, the reader is referred to the web version of this article.)

the cloud component remains small (Fig. 5f). Instead, PA reaches one of its annual peaks in May, when both surface and cloud contributions are relatively large, highlighting the combined influence of surface and atmosphere processes on Earth's energy budget.

Fig. 6 illustrates the deseasonalised monthly series of RSR and its three components. Noting that the deseasonalized monthly series of PA closely resembles that of RSR (Fig. 4a), we only present the decomposition of RSR. Visually, the fluctuations in the cloud component anomalies closely align with the anomalies in total RSR. Statistically, the correlation coefficient between cloud component anomalies and RSR anomalies is 0.87, significantly higher than the correlations with clear-sky atmospheric (0.21) and surface component (0.18) anomalies. It has been pointed out that most of the monthly variations in TOA RSR are related to changes in clouds (Loeb et al., 2007), which could increase the STD of TOA RSR anomalies by over twofold (Kato, 2009). Moreover, according to the CERES EBAF 4.0 product, Loeb et al. (2019) found that 81 % of the monthly variations in global mean RSR flux anomalies are linked to atmospheric changes, predominantly due to clouds, while surface changes account for 6 %, and atmosphere-surface covariation contributes 13 %. Here, our findings also indicate that the interannual variability of global mean RSR is primarily driven by the cloud component, which exhibits a detrended STD of 0.62 W m^{-2}—two to three times greater than that of the clear-sky atmospheric component (0.31 W m^{-2}) and the surface component (0.19 W m^{-2}).

To explore the sources of interannual variability in RSR, Fig. 6 (b-d) further illustrates the spatial distribution of detrended STDs for the three components, which are modulated by the variability of atmospheric and surface drivers (see Section 3.1 for detailed analysis). The STDs of the clear-sky atmospheric and surface components are very small at low and middle latitudes, especially over oceans. Note that the lower interannual variability in these components despite high mean values likely results from the persistence of aerosol sources and land surface conditions. The surface component (Fig. 6c) exhibits large STD values over the Arctic Ocean along continental coasts, which indicates the changes in sea ice and snowpack. In addition, the interannual variability of the cloud component dominates that of RSR across much of the globe (Fig. 4b and Fig. 6d). In particular, the maximum STDs of RSR and PA in the tropical Pacific correlate closely with the STDs of the cloud component, which may be attributed to the cloud variability associated with the El Niño-Southern Oscillation (ENSO) (Kato, 2009). Previous studies (Smith et al., 1990; Jönsson and Bender, 2022) have emphasized the significance of the ENSO-induced cloud variability as the primary source of interannual variations in global-scale RSR. Furthermore, we find suspiciously large STDs of three RSR components over the Antarctic continent, which is inconsistent with the typically stable conditions in this region (low cloudiness, low aerosols (Chen et al., 2024), permanent snowpack) and low interannual variability of total RSR (although there may be partial compensation between components). Moreover, the interannual variability of these components in Antarctica is much larger than in other regions with components of similar magnitude. Therefore, these unusually large STDs may stem from errors associated with the sensitivity of high surface albedo regions to the component decomposition methods. Additionally, the challenges of cloud detection by passive satellite sensors in polar regions may also contribute to some of the observed inaccuracies.

Fig. 7 illustrates the decadal trends of RSR and its components on global and hemispheric scales. Global mean RSR shows a significant downward trend from 2001 to 2023 at a rate of 0.78 W m^{-2} per decade. In particular, from the end of 2013 to the end of 2016, both global mean PA and RSR have declined rapidly (Fig. 4a). The timing of this turnaround coincides with the end of the global "warming hiatus". The so-called "global warming hiatus" refers to the period between approximately 1998 and 2013 when the rate of increase in global mean surface temperature slowed down relative to the latter half of the 20th century (Hartmann et al., 2013; Trenberth, 2015; Yan et al., 2016). After the beginning of 2014, the global mean surface temperature significantly increased again coinciding with the phase reversal of Victoria Mode (VM) (Xiao and Ren, 2023) and a shift in the Pacific Decadal Oscillation (PDO) index from negative to positive (Loeb et al., 2018b; Loeb et al., 2021a), which contributed to a warmer eastern Pacific SSTs and reduced low cloud cover. As the strong 2015/2016 El Niño developed, deep convection shifted from the western to the central Pacific (Pinker et al., 2017; Jönsson and Bender, 2022). Given the sensitivity of eastern Pacific low clouds to SST changes and the reorganization of tropical convection, these processes likely contributed to the pronounced decline in global mean RSR from 2014 to 2016. Additionally, the decreasing trend in RSR is significant in both the NH (−0.90 W m^{-2} $decade^{-1}$) and SH (−0.66 W m^{-2} $decade^{-1}$), with a more rapid decrease in the NH. Analyzing the individual components reveals that both the global mean cloud and surface components demonstrate notable decreasing trends, with values of −0.62 W m^{-2} $decade^{-1}$ and -0.12 W m^{-2} $decade^{-1}$, respectively, while the decreasing trend in the clear-sky atmospheric component is not statistically significant (Fig. 7). This is because the surface and cloud components decrease significantly in both hemispheres, while the clear-sky atmospheric component decreases significantly in the NH but increases significantly in the SH. These trends have been widely examined in terms of distribution and underlying reasons (Loeb et al., 2021a; Loeb et al., 2022; Stephens et al., 2022; Li et al., 2024; Loeb et al., 2024).

Large RSR/PA variations on regional and monthly scales may cancel each other out when averaged globally or annually, which may obscure

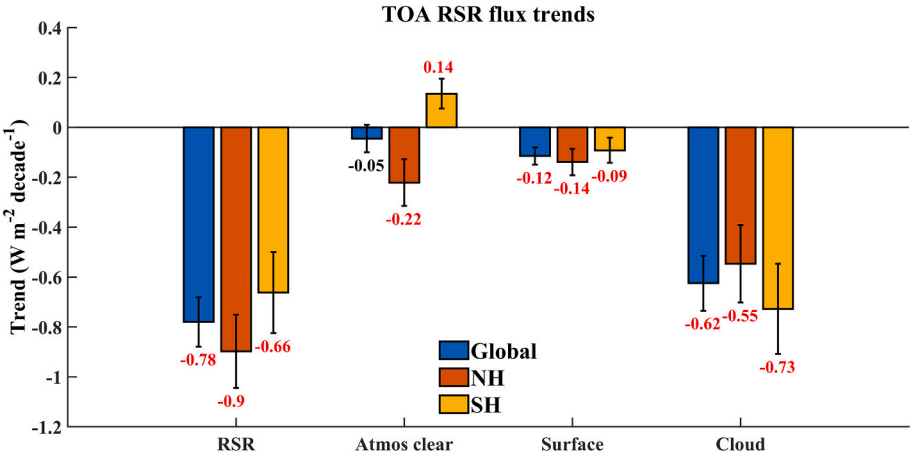

Fig. 7. Trends in global, NH, and SH average RSR and its clear sky atmospheric, surface, and cloud components from 2001 to 2023. Error bars represent the 95 % confidence intervals for the trends; if the interval includes zero, the trend is not significantly different from zero. Red numbers indicate trends that passed the 95 % significance test. (For interpretation of the references to colour in this figure legend, the reader is referred to the web version of this article.)

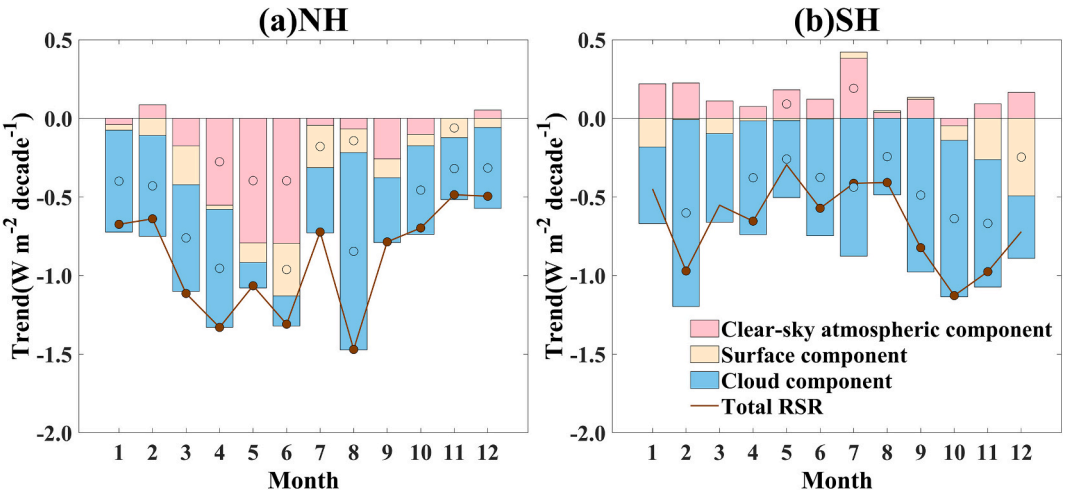

Fig. 8. The hemispheric averaged trends in RSR and its components in the (a) NH and (b) SH for different months from 2001 to 2023. Pink, yellow, and blue bars indicate trends in the clear-sky atmospheric, surface, and cloud components, respectively. The brown line indicates the trend of total RSR. Dots of different colors indicate that the trend of the corresponding variable is significant at the 95 % confidence level. [Adapted from Li et al., 2024.] (For interpretation of the references to colour in this figure legend, the reader is referred to the web version of this article.)

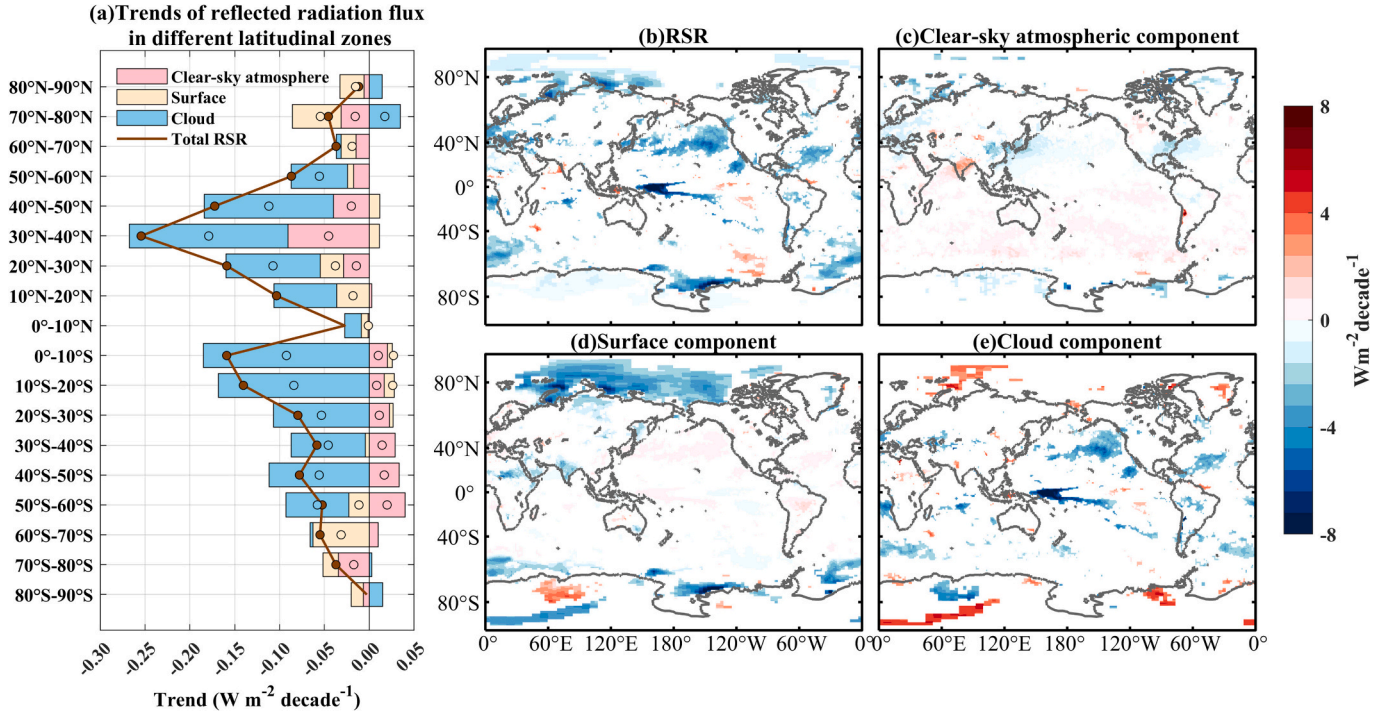

Fig. 9. (a) The zonal mean trends at different latitudinal zones from 2001 to 2023. Pink, yellow, and blue bars indicate trends in the clear-sky atmospheric, surface, and cloud components, respectively. The brown line indicates the trend of total RSR. Dots of different colors indicate that the trend of the corresponding variable is significant at the 95 % confidence level. [Adapted from Li et al. (2024).] Trends in (b) the TOA RSR flux (same as Fig. 4d) and its (c) the clear-sky atmospheric, (d) surface, and (e) cloud components for January 2001–December 2023. All points with colour pass the 95 % significance test; non-significant trends are not marked. (For interpretation of the references to colour in this figure legend, the reader is referred to the web version of this article.)

important signals. Moreover, there are significant regional and seasonal differences among various influencing factors. Decomposing RSR variations into finer spatial and temporal scales can help to identify driving factors and further improve model simulations. Therefore, following Li et al. (2024), we conduct a detailed analysis of the annual and hemispheric trends of RSR and its components at monthly (Fig. 8) and latitude scales (Fig. 9). Note that our results differ somewhat from those of Li et al. (2024) due to different study time periods. Fig. 8 shows that RSR in both hemispheres has exhibited a significant downward trend in nearly all months. In July in the NH and in December in the SH, the decline of RSR is primarily driven by the significant decrease of surface albedo, possibly linked to the reduction of snow and ice cover in polar regions (Noël et al., 2015; Wang et al., 2018; Rantanen et al., 2022). Although the soil moisture has decreased across many regions during summer (Peng et al., 2023), the expected increase in surface albedo is not observed, indicating a limited role of soil wetness in the overall surface albedo trend. Additionally, in the NH (Fig. 8a), the decrease in RSR from April to June is mainly attributed to a reduction in clear-sky atmospheric components, influenced by decreased dust activity in the mid-latitude dust belt (Shao et al., 2013; An et al., 2018; Zhao et al.,

2018; Jiao et al., 2021; Shi et al., 2021; Zhou et al., 2023) and reduced pollution aerosols, such as sulfate aerosols, in Europe, central and eastern China, and North America (Zhao et al., 2017; Li et al., 2020; Tao et al., 2020; Yu et al., 2020; Gui et al., 2021b; Cui et al., 2022; Tang et al., 2022). For the remaining months, the decrease is largely influenced by reduced cloud components due to changes in cloud properties. In the SH (Fig. 8b), a significant and dominant downward trend in the cloud component is observed for all months except January, March, and December.

When examining the long-term trends in different latitude zones and at regional scales (Fig. 9), more detailed insights can be gained. The most pronounced decreasing trends in RSR in the NH are observed in the latitude zones of 30°-50°N, driven by declines in both cloud and clear-sky atmospheric components (Fig. 9a). Loeb et al. (2024) distinguished the contributions of different cloud types to trends in shortwave radiation. They noted that in the subtropical regions of the NH, the CF of low and mid-level clouds and their reflection of solar radiation have decreased, which correlates well with rising SST. Specifically, a significant decreasing trend in the cloud component can be observed over the northern Pacific, especially the northeastern Pacific and North Atlantic close to North America (Fig. 9e) (Loeb et al., 2018b; Loeb et al., 2020a, 2020b). The decreased reflected radiation by cloud component over the northeast Pacific may be associated with increased SST and weakened temperature inversion intensity, which markedly reduces low cloud cover (Loeb et al., 2018b; Loeb et al., 2020a, 2020b; Andersen et al., 2022). Elevated SSTs are linked to extratropical processes, such as the VM phase transition (Xiao and Ren, 2023), and local oceanic dynamics, like mixed-layer shoaling, which reduces heat capacity (Hu et al., 2024). The increased SST reduces the stability of the marine boundary layer (MBL), resulting in MBL deepening and decoupling between cloud cover and surface moisture supply, ultimately reducing cloud cover (Loeb et al., 2018b). The reduction in cloud component over the North Atlantic may be related to a reduction in the optical thickness of low clouds due to a decrease in aerosol optical depth (AOD) (Park et al., 2024), which is associated with industrial emission reductions (Zhao et al., 2017; Feng et al., 2020; Gupta et al., 2022) and a decline in sulfur emissions from shipping (Jin et al., 2018; Gryspeerdt et al., 2019; Watson-Parris et al., 2022). Furthermore, the reduced scattering of aerosol particles due to anthropogenic aerosol emission reduction may be responsible for the reduction of the clear-sky atmospheric component in the NH (Zheng et al., 2018; Loeb et al., 2021b; Stephens et al., 2022; Hodnebrog et al., 2024). Additionally, there is a significant decreasing trend in the surface component in 10–30°N (Fig. 9a), primarily concentrated in northern tropical Africa and India (Fig. 9d), which may be related to notable greening since the 21st century (Chen et al., 2019). The former (northern tropical Africa) is likely due to increased vegetation from precipitation, while the latter (India) is attributed to the expansion of agricultural land (Chen et al., 2019). Besides, the reduction of snow/ice coverage contributes to the decline in the surface component over high latitudes in the NH (Fig. 9d) (Zhang et al., 2019). In the latitude zones of 70–80°N (Fig. 9a), there is a significant positive trend in the cloud components, likely due to an increase in polar CF, although its contribution to the hemispheric RSR trends is relatively small (Loeb et al., 2024).

In the SH, the decreasing trend in RSR gradually weakens from low to high latitudes (Fig. 9a). This decline is primarily driven by cloud components, mainly due to the reduction of mid-level clouds, along with a smaller decrease in low-level clouds (Loeb et al., 2024). The decrease in the cloud component in the western tropical Pacific region (Fig. 9e) can be linked to the shift of the convective zone from the warm pool in the western Pacific to the central Pacific under El Niño conditions (Pinker et al., 2017; Jönsson and Bender, 2022). The significant decrease in the cloud components over the Southern Ocean off the east coast of South America (Fig. 9e) is well aligned with the rising trend in SSTs, and there is a notable reduction in the mid-level CF in this area (Loeb et al., 2024). It is important to note that the clear-sky atmospheric component exhibits increasing trends in the 20°-60°S zones (Fig. 9a). This increase may be partly attributed to the rising aerosol loading, including dust, smoke aerosols produced by biomass burning (Reisen et al., 2013; Gui et al., 2021a; Pan et al., 2020; Li et al., 2021; Miinalainen et al., 2021; Yang et al., 2021), as well as sea salt aerosols and phytoplankton-produced sulfate aerosols over the Southern Ocean (Fig. 9c) (Bhatti et al., 2022). In addition, in the region of 60–70°S along the Antarctic continent (Fig. 9d), there is a significant downward trend in surface components, indicating a notable retreat of sea ice coverage (Wu et al., 2020).

2.3. Hemispheric symmetry

2.3.1. Definition and understanding of the hemispheric symmetry of PA

The first satellite-based observations of Earth's radiative balance in the 1960s revealed that the Earth-atmosphere system reflects nearly equal amounts of shortwave radiation in both hemispheres (Vonder Haar and Suomi, 1971). This finding has been supported by subsequent studies (Ramanathan, 1987; Zhang and Rossow, 1997). However, the accuracy of the measurements at that time was not sufficiently robust. The availability of CERES, which provides more accurate satellite measurements of Earth's TOA radiation budget, further confirms this feature. Notably, the difference in PA between the hemispheres is only 0.03 % of the global average PA (Jönsson and Bender, 2022). This raises the question: how does this occur? In fact, the hemispheric symmetry of the PA results from the cancellation of its asymmetric components. That is, the hemispheric asymmetry in clear-sky albedo caused by the distribution of land and sea as well as aerosols, is counterbalanced by the asymmetry in clouds, resulting in a near-symmetric multiyear mean all-sky albedo within measurement uncertainty (Voigt et al., 2013; Datseris and Stevens, 2021). By estimating the spatial degrees of freedom in the RSR, Voigt et al. (2013) emphasized that this symmetry is a significant characteristic of the Earth-atmosphere system rather than a negligible one. They randomly divided the Earth into halves of equal area, but found that only 3 % of the random hemisphere pairs show a hemispheric difference in RSR of less than 0.1 W m^{-2}, as observed by satellites. Furthermore, this characteristic has been consistently documented across multiple versions of the CERES dataset, suggesting that the symmetry of PA is not a trivial property and may imply the presence of underlying dynamical mechanisms. The potential mechanisms that may explain the hemispheric albedo symmetry and the related maintenance or compensation processes involving clouds are reviewed in Section 3.2.

Given that interannual anomalies in RSR closely resemble those in PA, RSR is often used to study the hemispheric symmetry of PA for convenience in calculations. Due to updated data versions, varying time record lengths, and differing calculation methods, the calculated magnitude of the hemispheric difference in RSR has varied, with estimates ranging from 0.1 W m^{-2} (Voigt et al., 2013), and 0.2 W m^{-2} (Stephens et al., 2015), up to 0.35 W m^{-2} (Stevens and Schwartz, 2012). Datseris and Stevens (2021) further explored the range of hemispheric differences using a bootstrapping approach on monthly mean RSR data. Specifically, they constructed numerous surrogate time series by randomly sampling different monthly data with put-backs, which yielded a range of 0.1 ± 0.28 W m^{-2} for the hemispheric difference in RSR. Recently, Li et al. (2024) examined the applicability of various datasets in studying the hemispheric symmetry of RSR based on different symmetry criteria. When considering a hemispheric difference in RSR of less than 0.1 or 0.2 W m^{-2} as an indicator of symmetry, they found that the CERES EBAF dataset demonstrates symmetry over time scales of 15 years and 9 years, respectively. Additionally, the annual average hemispheric difference in RSR from CERES consistently remains below 1 W m^{-2} and falls within the data uncertainty range. In addition to CERES, the performance of other datasets (Cloud_cci Advanced Very High Resolution Radiometer (AVHRR) PMv3, International Satellite Cloud Climatology Project (ISCCP), the Fifth Generation of ECMWF Atmospheric Reanalysis (ERA5), and Modern-Era Retrospective Analysis

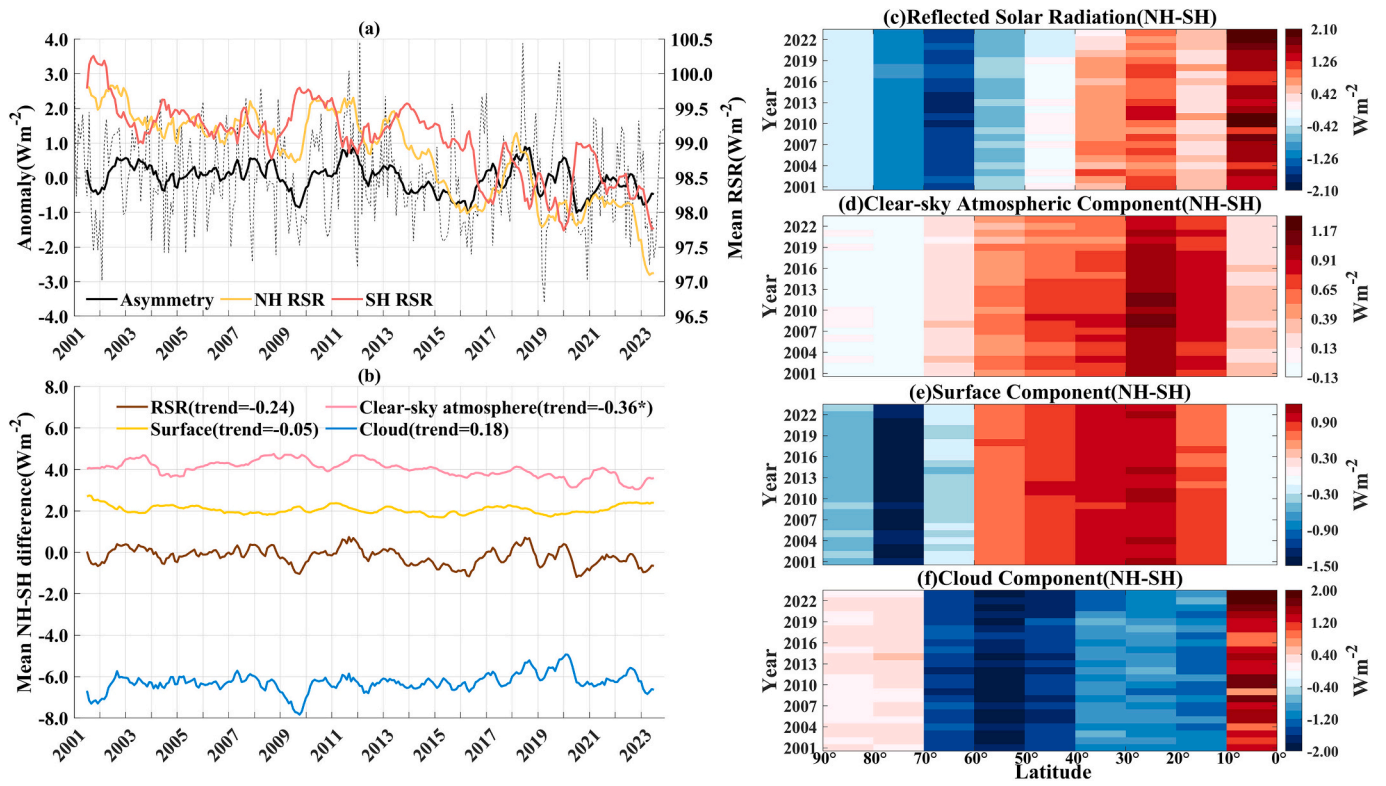

Fig. 10. (a) Left y-axis: Monthly anomalies in hemispheric differences (NH-SH) of deseasonalized RSR (black dashed line) and their 12-month running-mean (black solid line). Right y-axis: the 12-month running-mean RSR for the NH (yellow line) and SH (red line). (b) Monthly average hemispheric differences in RSR and its components, presented as 12-month running-mean. Their long-term trends (W m^{-2} $decade^{-1}$) are marked on the upper labels, and numbers with asterisks indicate that they pass the 95 % significance test. All 12-month running-mean series display only the portions with complete 12-month averages. The Annual-averaged interhemispheric differences (NH–SH) between corresponding zones of (c) total RSR and its (d) clear-sky atmospheric, (e) surface, and (f) cloud components. [(a) and (b) are adapted from Jönsson and Bender, 2022; (c)-(f) are adapted from Li et al., 2024.] (For interpretation of the references to colour in this figure legend, the reader is referred to the web version of this article.)

for Research and Applications, version 2 (MERRA-2)) that provide long-term data on TOA RSR in terms of hemispheric symmetry is discussed in Section 5.

This hemispheric symmetry of the Earth's PA plays a potentially crucial role in the global energy balance (Stephens et al., 2015; Loeb et al., 2021a), cross-equatorial heat transport (Voigt et al., 2014; Stephens et al., 2015), the hydrological cycle (Stephens et al., 2016), and the atmospheric-oceanic circulation (Kang et al., 2008). While the ISR and RSR at the TOA exhibit hemispheric symmetry, the outgoing longwave radiation is not equal between the two hemispheres. Consequently, the hemispheric asymmetry in net radiation drives cross-equatorial energy transport, through both atmospheric and oceanic pathways (Stephens et al., 2015). For example, northward oceanic heat transport, driven by the Atlantic meridional overturning circulation (AMOC), is partially counterbalanced by southward atmospheric heat transport, which is associated with the northward average position of the ITCZ (Diamond et al., 2022). This oceanic energy transport may influence the location of the ITCZ (Kang et al., 2008; Frierson et al., 2013; Marshall et al., 2014), and the resulting changes in tropical cloud systems can further modify the hemispheric differences in RSR. Therefore, understanding how the hemispheric albedo symmetry varies over time can provide valuable insights into the response of clouds to changes in climate forcing, thereby helping reduce uncertainties in model simulations and climate predictions (Jönsson and Bender, 2022).

2.3.2. *Persistence, variability, and decadal trends of Earth's hemispheric RSR symmetry*

The anomalies in the hemispheric differences of RSR and the average RSR time series for both hemispheres are illustrated in Fig. 10. The monthly anomalies in the hemispheric difference of RSR can reach nearly 4 W m^{-2} (Fig. 10a, black dashed line), highlighting that hemispheric symmetry is not a characteristic observed on a monthly scale. Fig. 10b presents the 12-month running-mean time series of hemispheric differences for each component of RSR. Quantitative analysis indicates that the hemispheric symmetry in RSR results from a delicate balance and mutual offset among the contributions from the surface (average hemispheric difference from 2001 to 2023: 1.85 W m^{-2}), clear-sky atmospheric (3.88 W m^{-2}), and cloud (−5.71 W m^{-2}) components (Fig. 10b). Under clear-sky conditions, Diamond et al. (2022) emphasized that the atmosphere contributes approximately 80 % to the hemispheric asymmetry in RSR, while the surface accounts for only 20 %. This suggests that clear-sky hemispheric asymmetry is predominantly regulated by aerosols, and the relatively small contribution of the surface is due to the highly reflective Antarctic partially offsetting the hemispheric albedo contrast caused by uneven land cover. Further analysis reveals that the NH reflects more solar radiation in the 0°-40° latitude zone than the corresponding zone in the SH, but the SH reflects more radiation in the 50°-90°S latitude zone, compensating for this difference (Fig. 10c) (Li et al., 2024). The dominance of RSR in the NH for the equator to 40° can be attributed to two main factors: first, the greater cloud component in the 0–10° latitude zone due to the mean position of the ITCZ being north of the equator (Fig. 10f); second, the combined effect of clear-sky atmospheric and surface components in the 10–60° latitude zone due to the abundant dust and sulfate aerosols (Diamond et al., 2022) as well as extensive land cover in the NH (Fig. 10d and e). In contrast, the SH exhibits a larger cloud component in the 10–70° latitude zone (Fig. 10f), and surface component in polar regions with high ice and snow albedo (Fig. 10e).

Besides, some studies have pointed out that the annual cycle pattern of hemispheric RSR differences is dominated by the cloud component at mid-low latitudes and the surface component at high latitudes (Li et al., 2024). The interannual variability of hemispheric asymmetry in RSR is primarily driven by clouds (Stephens et al., 2015; Seinfeld et al., 2016). From Fig. 10b, it is evident that changes in the hemispheric differences of the total RSR closely align with that of the cloud component. Jönsson and Bender (2022) conducted composite analyses of monthly anomalies in RSR under extremely bright conditions in both the NH and SH, and found that extreme changes in hemispheric asymmetry in RSR are mainly influenced by variations in tropical cloud cover, particularly in response to the phases of ENSO (Loeb et al., 2007), followed by changes in subtropical cloud cover. They observed that the spatial distribution of RSR in months with significant hemispheric RSR asymmetries exhibit signals corresponding to different ENSO phases: a prominent El Niño signal in months with more SH reflection, while a La Niña signal is detected in months with more NH reflection (Jönsson and Bender, 2022).

Despite the observed decrease in global and hemispheric RSR over recent decades, along with the higher and faster-increasing temperatures in the NH compared to the SH, the difference in hemispheric RSR has not demonstrated a statistically significant long-term trend, indicating that the symmetry remains relatively stable (Stevens and Schwartz, 2012; Voigt et al., 2013; Stephens et al., 2015; Datseris and Stevens, 2021; Jönsson and Bender, 2022; Diamond et al., 2024; Li et al., 2024). However, there has been a significant reduction in the hemispheric asymmetry of the clear-sky atmospheric component of −0.36 W m^{-2} $decade^{-1}$ from year 2001 to 2023 (Fig. 10b), which can be attributed to a significant decrease in the NH (−0.22 W m^{-2} $decade^{-1}$) and a significant increase in the SH (0.14 W m^{-2} $decade^{-1}$) (Fig. 7). Notably, the surface and cloud components are decreasing in both hemispheres (Fig. 7). But the reduction of the surface component in the NH is occurring at a faster rate, which may be closely linked to the decline in polar ice and snow cover, as well as the phenomenon of Arctic amplification (Sweeney et al., 2023). In contrast, the cloud component in the SH is decreasing more rapidly, particularly in the mid and low latitudes. However, the hemispheric differences in the surface and cloud components show non-significant decreasing and increasing trends, respectively (Fig. 10b).

3. Influencing factors of long-term changes in RSR and potential maintenance mechanisms of hemispheric symmetry

3.1. Influencing factors of RSR changes

In the preceding sections, we have analyzed the contributions of three components to PA and RSR, whose variations are linked to the atmospheric and surface characteristics (Loeb et al., 2007; Voigt et al., 2014; Jian et al., 2018; Lv et al., 2022). Specifically, changes in the clear-sky atmospheric component are closely associated with key atmospheric elements such as water vapor and aerosols (Grassl and Newiger, 1982; Held and Soden, 2000; Christopher and Zhang, 2002; Che et al., 2024), while the surface component is significantly affected by vegetation cover, land use, desertification, and ice/snow cover (Myhre and Myhre, 2003; Qu and Hall, 2005; Barnes and Roy, 2008; Zeng and Yoon, 2009; Kashiwase et al., 2017). The macro-physical properties of clouds — such as CF, liquid water path (LWP), and IWP — are critical in determining changes in the cloud component (Hanna, 2007; Engström et al., 2015; Stephens et al., 2015; Seinfeld et al., 2016). The spatiotemporal distribution patterns and dynamic evolution of these factors directly shape and regulate the variations in RSR and its components (Hu and Stamnes, 1993; Loeb et al., 2007; Voigt et al., 2014; Letu et al., 2018; Li et al., 2018a; Zhao et al., 2019; Yang et al., 2020; Lv et al., 2022). Fig. 11 highlights the factors and significant natural and anthropogenic activities that may influence RSR components. The subsequent parts will elaborate on the changes and impacts associated with these factors.

3.1.1. Impact of cloud properties on RSR changes

Generally, the shortwave radiative effect of clouds contributes to cooling the Earth, primarily achieved by low-level clouds (Hartmann and Doelling, 1991; Wood, 2012). The macro-properties of clouds exhibit positive correlations with PA, which indicates that increases in CF, LWP, and IWP enhance the PA. Loeb et al. (2007) and Bender et al. (2017) have highlighted the critical role of CF changes in driving variations of TOA shortwave radiation. Meanwhile, the microphysical characteristics of clouds can directly or indirectly influence their shortwave radiative effects (Bellouin et al., 2020). For instance, with a constant cloud water content, a smaller effective radius leads to higher droplet number concentration and thus increased cloud albedo, which is known as the Twomey effect (Twomey, 1974). Moreover, changes in droplet number concentration can affect the dispersion of the cloud drop size distribution, where a wider dispersion results in decreased cloud albedo (Peng and Lohmann, 2003). On the other hand, the

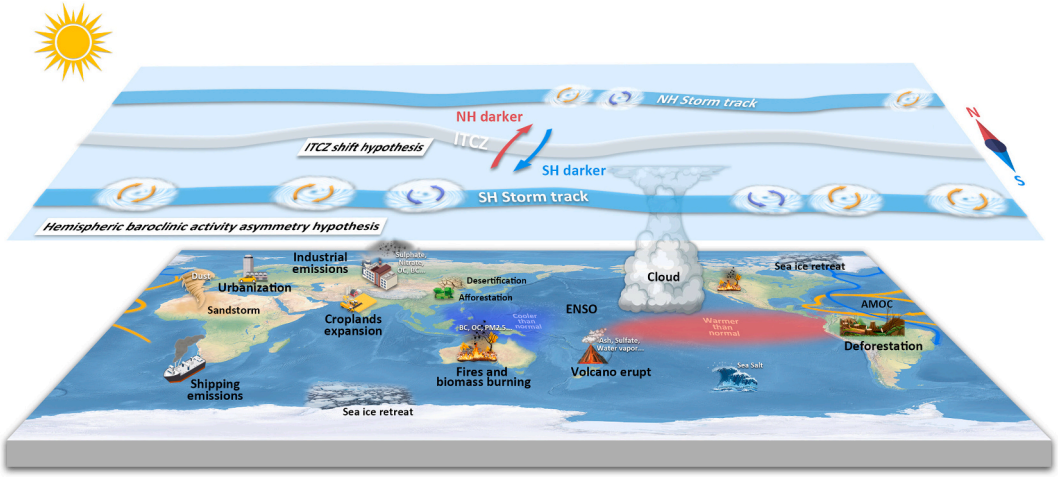

Fig. 11. The schematic illustrates the factors and activities that influence variations in PA and RSR, including cloud, clear-sky atmospheric, and surface components (as detailed in Section 3.1), as well as two hypotheses regarding large-scale circulation patterns that may maintain the hemispheric symmetry of PA (upper layer) (as detailed in Section 3.2).

Table 3
The atmospheric and surface parameters correspond to the three components of RSR used in this study for January 2001–December 2023 and their data sources. All variables are provided at monthly temporal resolution and spatially interpolated to 1° × 1° grids. Note that, to ensure consistency with the EBAF data and to minimize errors from the diurnal cycle of clouds, we average the cloud properties data from the Terra and Aqua sources over their overlapping period (July 2002 to February 2023). For the remaining periods, the cloud properties are sourced from Terra.

Components of RSR	Parameter	Dataset
Cloud component	Cloud Fraction (CF)	CERES SSF1deg
	Ice Water Path (IWP)	CERES SSF1deg
	Liquid Water Path (LWP)	CERES SSF1deg
	Ice/snow Coverage (ISC)	CERES SSF1deg
Surface component	Normalized Difference Vegetation Index (NDVI)	MODIS MOD13C2
	Surface Albedo (SA)	CLARA-A3
Clear-sky atmospheric component	Aerosol Optical Depth (AOD)	MERRA-2
	Total Column Water Vapor (TCWV)	ERA5

microphysical properties of clouds can alter their macro-properties, thereby impacting albedo. Specifically, an increase in droplet number concentration can either enhance or reduce cloud water (CF/cloud depth/LWP) and cloud albedo by suppressing precipitation (Albrecht, 1989) or by intensifying the entrainment process (Ackerman et al., 2004), respectively. Additionally, large-scale atmospheric and ocean circulations can alter RSR by redistributing heat globally and then regulating the distribution and types of clouds, as well as influencing climate feedback processes (Zhou et al., 2017). For instance, the increased SSTs and reduced low cloud cover can partly explain the decreased RSR (Loeb et al., 2018b; Loeb et al., 2021a). Additionally, previous studies have indicated that the ENSO-driven cloud changes not only serve as a major source of interannual variability in the global mean RSR but also contribute to variations of hemispheric asymmetries in RSR (Loeb et al., 2007; Jönsson and Bender, 2022). Furthermore, the AMOC is a key component of the Earth's thermohaline circulation (Weijer et al., 2019), and studies indicate that the AMOC has slowed (Rahmstorf et al., 2015; Smeed et al., 2018; Caesar et al., 2021; Kilbourne et al., 2022). This slowdown of AMOC, along with reduced northward transport of warm surface water and southward transport of cold deep water, may slow the decline of Arctic sea ice and cause a southward shift of the ITCZ and associated tropical cloud systems (Liu et al., 2020), which significantly impact the variation of PA and RSR.

To better understand the relative contributions of various factors affecting long-term variations in RSR, following Jian et al. (2018), we adopt a stepwise multiple linear regression approach. This analysis focuses on several predictor variables: CF, IWP, and LWP, which are associated with changes in the cloud component; AOD and total column water vapor (TCWV), which relate to changes in the clear-sky atmospheric component; and normalized difference vegetation index (NDVI) and ice/snow coverage (ISC), which are linked to surface component variations. In the absence of NDVI and ISC as predictor variables, surface albedo (SA) is used as a substitute. The specific data sources are listed in Table 3, and the detailed methodologies can be referenced in Jian et al. (2018). By comparing the relative contributions of these factors (Fig. B1), we can map the global spatial distribution of the dominant and secondary factors explaining the long-term variability of RSR, as illustrated in Fig. 12. The results indicate that CF is the predominant factor

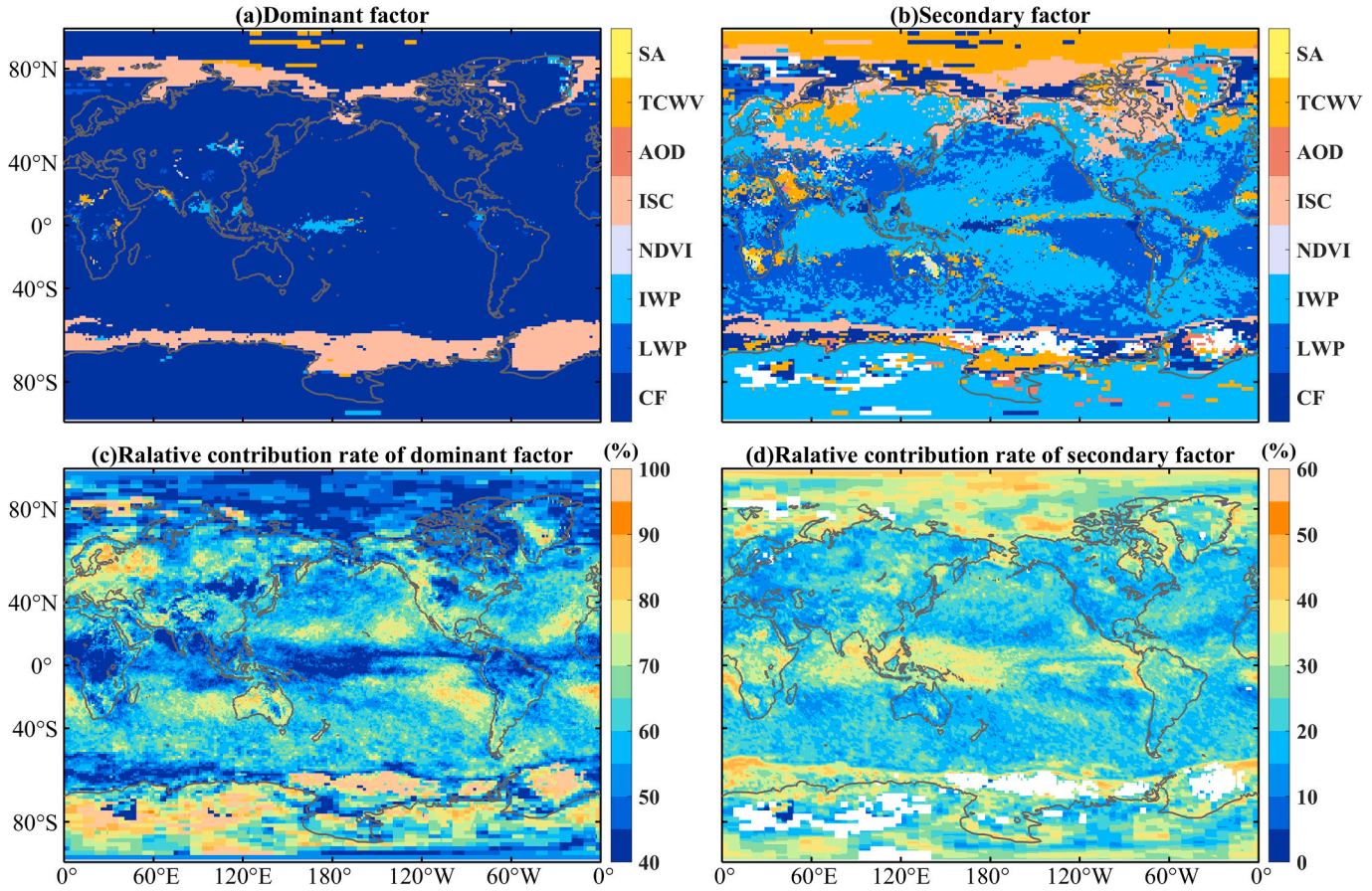

Fig. 12. The global distributions of (a) dominant and (b) secondary factors that explain the long-term variability of RSR and (c-d) their corresponding relative contributions [Adapted from Jian et al., 2018].

driving long-term changes in RSR across most mid-latitude regions, often contributing over 50 % (Fig. 12a and c). Notably, in the western Pacific warm pool, IWP emerges as the leading factor influencing RSR variations, with CF playing a secondary role. Interestingly, CF is the dominant factor in polar regions, rather than ISC or SA, which highlights the significant masking effect of cloud cover on the underlying surface (Fig. 12a) (Sledd and L'Ecuyer, 2019; Wu et al., 2020). Kato et al. (2006) demonstrated a correlation between TOA irradiance and CF in polar regions, suggesting that reductions in sea ice area can be partially offset by increases in CF. That is, cloud formation suppresses the positive feedback of ice albedo and partially compensates for albedo changes due to melting sea ice (He et al., 2019). In several typical marine and terrestrial stratocumulus regions and their surroundings, such as Namibian, Australian, Peruvian, Californian, Canarian, North Pacific, and Chinese Sratus, LWP is identified as the second dominant factor after CF (Fig. 12b). In contrast, in the northern Eurasian continent, the northern Indian Ocean, both sides of the equatorial western Pacific, as well as parts of South and North America, the eastern Atlantic, parts of the Southern Ocean, and Antarctica, IWP serves as the secondary factor that explains the long-term variability of RSR. It is important to note that clouds over Antarctica are predominantly ice clouds, supercooled liquid water clouds, or mixed-phase clouds (Lawson and Gettelman, 2014; Ricaud et al., 2024). The phase transitions among these different cloud types can influence the shortwave radiative effects (Lachlan-Cope, 2010; Lawson and Gettelman, 2014), thereby affecting variations in RSR. Please note that most of our findings are consistent with those of Jian et al. (2018). The main difference is that Jian et al. (2018) demonstrated that the SA plays a dominant role in the long-term variability of RSR near the South Pole, with a secondary role over the North Pole and Antarctic continent. In contrast, our study finds that the TCWV and IWP are the secondary contributors in the Arctic and Antarctic, respectively. These discrepancies primarily arise from the differences in the time periods, predictor variables (AOD and TCWV replacing clear-sky two-way atmospheric transmittance T^2), and datasets used (the RSR and SA data).

3.1.2. Impact of surface parameters on RSR changes

The contribution of the surface to the RSR at the TOA is affected by changes in surface conditions, which are determined by factors such as ISC, vegetation, and soil moisture. As demonstrated by Lv et al. (2022), an increase in ISC or a decrease in NDVI and soil moisture leads to a greater surface contribution to PA. Similarly, Li et al. (2018b) observed that a decline in global SA from 2002 to 2016 coincided with a reduction in snowpack area and an increase in seasonally integrated NDVI. As illustrated in Fig. 12, ISC is the dominant factor in the long-term variability of RSR in the continental margin oceans near 80°N and along the Antarctic coast, while it ranks as the second most influential factor in parts of the NH land and northeastern North America. As supported by Jian et al. (2018), ISC shows a positive correlation with PA in the high latitudes of the Southern Ocean and the Arctic, where the ice and snow are highly reflective and undergoing significant changes. In addition to the ongoing retreat of Arctic sea ice (Comiso et al., 2008; Hofer et al., 2017; Wang et al., 2022; Sumata et al., 2023), the decline in Antarctic sea ice coverage has also garnered significant attention (Turner et al., 2022; Purich and Doddridge, 2023). Historically, Antarctic sea ice was considered relatively stable, even experiencing periods of growth. However, since 2015, warming in the Southern Ocean has contributed to the melting of Antarctic sea ice, further exacerbated by albedo feedback effects, resulting in a record low sea ice extent in 2023 (Purich and Doddridge, 2023; Kuhlbrodt et al., 2024; Roach and Meier, 2024). Additionally, although our analysis shows that NDVI does not rank among the top two factors influencing long-term regional RSR changes (Fig. 12), it does have a direct impact on SA, which in turn affects RSR at the TOA. At high latitudes in the NH, a negative regression coefficient between NDVI anomalies and PA anomalies indicates that increased vegetation reduces the SA (Bounoua et al., 2000; Bonan, 2008; Li et al., 2018b). Notably, research suggests that China and India are leading global greening in the 21st century, with China primarily contributing through afforestation and India mainly through agricultural expansion (Chen et al., 2019). Increased vegetation can lower albedo, which may cause heating of the surface and atmosphere, further promoting vegetation growth (Bounoua et al., 2000; Chapin III et al., 2005). Nevertheless, global forest loss continues, such as, the Brazilian Amazon rainforest is experiencing significant annual declines (Ripple et al., 2023). Deforestation typically increases SA, but the net radiation effects vary by region (Jiao et al., 2017). In tropical areas, deforestation usually leads to a net warming effect at the TOA due to decreased evapotranspiration and cloud cover. Conversely, in high-latitude regions, particularly during winter, deforestation is expected to cause a cooling effect at the TOA (Bala et al., 2007; Betts et al., 2007; Bonan, 2008). Furthermore, deforestation can exacerbate land desertification, which increases SA and annual mean RSR (Calabrò and Magazù, 2016). In addition, anthropogenic activities significantly impact surface types and their albedo. The rapid expansion of urban areas alters surface properties, with urban buildings and roads generally exhibiting lower albedo than agricultural fields (Menon et al., 2010; Hu et al., 2016; Trlica et al., 2017). Statistics show that changes in the composition and physical properties of land cover due to urbanization have led to a decrease in SA, resulting in a positive radiative effect at the TOA of approximately 0.00017 W m^{-2} (equivalent to 0.18 Gt CO_2-eq) from 2001 to 2018 (Ouyang et al., 2022). Although this impact is relatively small, other potential impacts of urbanization cannot be ignored.

3.1.3. Impact of water vapor and aerosols on RSR changes

The atmospheric extinction ability is crucial for the clear-sky atmospheric component of the RSR (Jian et al., 2018), which is influenced by water vapor and aerosols. Water vapor primarily affects the RSR at the TOA by directly absorbing solar radiation (McDonald, 1960). As illustrated in Fig. 12b, TCWV is a secondary factor in the long-term variability of RSR in regions such as western Russia, Saudi Arabia, northern Greenland, and the Arctic Ocean. Notably, in the Arctic Ocean, TCWV often accounts for over 30 % of the variability in RSR (Fig. 12d). The reduction of Arctic sea ice may lead to increased heat flux from the ocean to the atmosphere, which elevates the water vapor content (Serreze et al., 2012; Ghatak and Miller, 2013; Ridley et al., 2023). Additionally, during winter, water vapor can be also transported from lower latitudes to the Arctic (Doyle et al., 2011; Kurita, 2011). This increased water vapor enhances downward longwave radiation and absorbs shortwave radiation, further warming the surface and accelerating ice and snow melting. This water vapor feedback is considered to amplify the Arctic amplification effect (Ghatak and Miller, 2013). In addition, although AOD is not among the top two factors affecting long-term RSR variability (Fig. 12), aerosols can directly absorb or scatter solar radiation depending on their types (McCormick and Ludwig, 1967; Bellouin et al., 2020) or indirectly influence RSR by altering cloud properties and consequently changing cloud albedo (Twomey, 1974; Twomey, 1977; Albrecht, 1989; Ackerman et al., 2004; Wang et al., 2024). Natural events such as volcanic eruptions and wildfires that release gases and aerosol particles, along with human activities that modify atmospheric composition, can decrease the transmittance of solar radiation in the atmosphere, thereby affecting RSR. Explosive volcanic eruptions can inject great amounts of sulfate aerosols into the stratosphere, potentially causing temporary cooling of the Earth (Robock, 2000). For example, the eruption of Mount Pinatubo in 1991 resulted in a high-albedo event that interrupted several years of global warming in surface temperatures (McCormick et al., 1995). In contrast to previous eruptions, the violent Hunga Tonga-Hunga Ha'apai eruption in 2022 not only injected volcanic ash into the stratosphere but also released a large quantity of water vapor (Millan et al., 2022; Schoeberl et al., 2023). As a result, the absorption of solar radiation by water vapor partially offset the reflection of volcanic ash, sulfates, and other aerosols, so the eruption did not significantly affect the global average RSR.

Furthermore, during the summer of 2019, widespread wildfires in Australia released substantial amounts of smoke and particulate matter into the stratosphere (Hirsch and Koren, 2021; Peterson et al., 2021), which significantly increased the AOD in the SH and enhanced the clear-sky atmospheric component. Notably, the smoke also darkened the New Zealand snowpack through long-range transport, leading to a reduction in SA (Pu et al., 2021). The anthropogenic increase in aerosol concentrations since industrialization has also played a significant role in the net cooling effect on the atmosphere (Bauer and Menon, 2012; Che et al., 2018). In this century, effective emission reductions in China, the United States, and Europe have resulted in a significant weakening trend in the clear-sky shortwave aerosol direct radiative effects in the NH (Loeb et al., 2021b), as well as a notable decreasing trend in the clear-sky atmospheric component of RSR (Li et al., 2024). In addition, regulations implemented by the International Maritime Organization to limit sulfur emissions from ships have led to a reduction in sulfate aerosols, which indirectly affects both the macro and microphysical characteristics of clouds, effectively decreasing the local albedo (Yuan et al., 2022; Diamond, 2023; Diamond et al., 2024).

3.2. Potential hypothesis for hemispheric symmetry maintenance mechanisms

As discussed in Section 2.3, hemispheric symmetry is a key characteristic of PA that arises from the cancellation of hemispheric asymmetries among three components. Is it merely a coincidental feature? Current research suggests otherwise. This symmetry, which has been observed since the inception of satellite monitoring, persists despite intensified climate change and a decline in RSR in both hemispheres (Jönsson and Bender, 2022; Li et al., 2024). However, robust observational evidence supporting the mechanisms that may maintain this symmetry remains limited. Considering that the cloud component not only dominates PA and its variations (Ramanathan, 1987; Ramanathan et al., 1989; Donohoe and Battisti, 2011), but also plays a crucial role in offsetting the clear-sky hemispheric albedo asymmetry, some hypotheses focus on how large-scale circulation regulates clouds to maintain hemispheric symmetry in PA. Many scholars have proposed related hypotheses, which are categorized into two types depicted in Fig. 11: the ITCZ shift hypothesis and the hemispheric baroclinic activity asymmetry hypothesis, which focuses on tropical and extratropical clouds, respectively.

3.2.1. ITCZ shift hypothesis

The ITCZ and the variations of tropical clouds controlled by it have received much attention. Paleoclimate studies have indicated that when the high-latitude ice sheets expand in one hemisphere, the ITCZ typically shifts toward the other hemisphere (Lea et al., 2003; Pahnke et al., 2007; Holbourn et al., 2010). This “tropical compensation mechanism” appears to partially offset the hemispheric albedo asymmetry caused by ice sheet expansion through changes in tropical cloud cover and RSR. Moreover, this mechanism, which is influenced by both atmospheric dynamics and ocean circulation, has been supported by climate model simulations (Chiang et al., 2003; Chiang and Bitz, 2005; Kang et al., 2008). Specifically, by conducting a simulation experiment based on an atmospheric circulation model of a slab-ocean planet, Voigt et al. (2014) generated the hemispheric asymmetry in the clear-sky albedo via perturbing sea SA in various regions. This setup allows us to investigate the response of planetary-scale atmospheric circulation and clouds to the hemispheric asymmetry in the clear-sky albedo. Their simulation indicated that the ITCZ tends to migrate toward the hemisphere with lower clear-sky albedo (or a darker surface, implying higher temperatures), accompanied by enhanced deep convection and the movement of upper-level tropical clouds. Consequently, the all-sky albedo of the darker hemisphere (with lower clear-sky albedo) increases, which reduces the albedo differences between hemispheres and promotes symmetry. However, they also found that the intense ITCZ movement may even lead to overcompensation, causing the darker hemisphere to reflect more shortwave radiation. From another perspective, Kang et al. (2008) conducted ocean mixed layer-atmosphere interaction experiments and revealed that the ITCZ is highly responsive to thermal forcing in the extratropics. In this context, the ITCZ may tend to shift toward the hemisphere with warmer extratropics, i.e. the NH. Despite this understanding, some researchers argue that the tropical compensation mechanism does not align with current observations. Specifically, Jönsson and Bender (2022) pointed out that the NH has a higher clear-sky albedo, and if the “tropical compensation mechanism” were valid, the ITCZ should be positioned in the SH; however, in fact, it has remained in the NH for a longer duration, thus failing to serve its compensatory role.

3.2.2. Hemispheric baroclinic activity asymmetry hypothesis

Recent research suggests that extratropical clouds play a crucial role in influencing the hemispheric symmetry of PA (Stephens et al., 2015; Bender et al., 2017; Datseris and Stevens, 2021; Diamond et al., 2022; Jönsson and Bender, 2022; Blanco et al., 2023; Crueger et al., 2023; Hadas et al., 2023). The extratropical regions not only exhibit the largest contribution to the hemispheric averaged cloud albedo, but also have the largest interhemispheric difference of cloud albedo (Bender et al., 2017; Datseris and Stevens, 2021). Thus, it is proposed that interhemispheric asymmetry of cloud albedo in extratropical regions, especially at mid-latitudes over oceans, is key to compensating the asymmetry in clear-sky albedo (Bender et al., 2017; Datseris and Stevens, 2021; Jönsson and Bender, 2022; Hadas et al., 2023). Several studies have attempted to explain the hemispheric differences in cloud properties from various perspectives, which may account for the hemispheric differences in cloud albedo, and serve as a potential source for the cloud compensation. For example, the storm tracks over the extratropical oceans of SH are highlighted to effectively compensate for the clear-sky hemispheric difference, as they are cloudier and brighter than those in the NH (Datseris and Stevens, 2021; Shaw et al., 2022). Especially, given the strong positive correlation between mid-latitude cloud-albedo and baroclinic activity, Hadas et al. (2023) pointed out that the observed hemispheric differences in cloud albedo can be well explained by differences in the number and intensity of cyclones and anticyclones in mid-latitudes. In their study, they indicated that the larger ocean coverage in the SH leads to higher baroclinicity, resulting in more frequent and intense synoptic weather systems, which contribute to more cloud cover and higher cloud albedo, and may effectively offset inter-hemispheric differences in clear-sky albedo. Furthermore, previous studies have shown that, according to observations, cloud amount and location of storm tracks significantly respond to greenhouse gas forcing and the resulting changes in the global temperature distribution, specifically manifested as the poleward shift and narrowing of the storm tracks (Bender et al., 2012). In a recent study, based on CMIP6 model simulations, Jönsson and Bender (2023) found that when carbon dioxide concentrations are abruptly quadrupled from pre-industrial levels, the NH albedo initially decreases, primarily due to the loss of Arctic sea ice, which leads to a deviation in hemispheric albedo differences from pre-industrial conditions. They further discovered that in some models, the SH’s extratropics can respond to the NH albedo decline by experiencing a reduction in cloud cover, which restored the hemispheric albedo difference to pre-industrial conditions through SH albedo decrease. However, Diamond et al. (2024) contested this view, arguing that the current hemispheric differences in clear-sky RSR are decreasing, and that the asymmetry of low clouds in extratropics is also declining, which may exacerbate the clear-sky asymmetry rather than provide compensation. Therefore, they contend that the cloud cover in the Southern Ocean cannot maintain all-sky symmetry over a decadal timescale, although it may be possible over longer timescales.

Overall, a single large-scale circulation system may only partially compensate for or exacerbate hemispheric asymmetry in clear-sky albedo. The hemispheric symmetry of PA is likely the result of fine-tuning

in cloud cover, cloud albedo, and cloud position by multiple planetary-scale circulation systems at different latitudes. This complex modulation process is vital for maintaining the stability of the Earth's climate system, highlighting the importance of energy transfer and circulation changes between the tropics and extratropics.

4. Model simulations of PA

4.1. Model performance

Climate models are essential tools for analyzing and predicting atmospheric and oceanic dynamics across various timescales, which have been widely used in critical research areas including climate sensitivity analysis and future climate projections (IPCC, 2013; Wang and Su, 2013; Eyring et al., 2016). Supported by the CMIP of the World Climate Research Programme (WCRP), the outputs of multiple models are publicly available in a standardized format for the climate community (Eyring et al., 2016). Despite advancements in simulating PA from CMIP phases three to six (CMIP3, CMIP5, CMIP6), general circulation models (GCMs) still exhibit obvious biases when compared to observational data (Bender et al., 2006; Lauer and Hamilton, 2013; Stephens et al., 2015; Jian et al., 2020). In this section, we primarily focus on the performance of CMIP models in reproducing the observational spatiotemporal distribution characteristics of PA and RSR, as well as their hemispheric symmetry features.

4.1.1. Simulation of basic characteristics of PA and RSR

We begin by reviewing the simulated performance of CMIP models regarding the characteristics of PA and RSR, as outlined in Section 2. The initial focus is on the global average and distributional characteristics of PA and RSR as simulated by these models. Previous studies have found that CMIP3 models generally overestimate the global mean PA compared to satellite observations (Bender et al., 2006; Donohoe and Battisti, 2011), and this overestimation continues into CMIP6 (Jian et al., 2020). Generally, the model ensemble mean can capture a spatial distribution of PA similar to observations, but there are still significant biases across various regions. For example, Jian et al. (2020) indicated that CMIP6 models overestimate the PA in regions such as the tropical Pacific and Indian Ocean, as well as the subtropical Pacific and Atlantic, which is attributed to an overestimation of cloud cooling effects. In the tropical Pacific, the incorrect representation of a double ITCZ structure by coupled climate models may lead to more cloud cover, potentially explaining the overestimation of PA (Lin, 2007; Hwang and Frierson, 2013). Additionally, challenges in modeling clouds over mid-latitude oceans have persisted across various CMIP phases (Trenberth and Fasullo, 2010; Hwang and Frierson, 2013; Grise and Polvani, 2014; Jönsson and Bender, 2022). Conversely, in some typical subtropical stratocumulus regions, models often underestimate PA, which aligns with the underestimation of CAF (Jian et al., 2020). These biases have persisted from CMIP3 (Bender et al., 2006) to CMIP5 (IPCC, 2013; Hinkelman, 2019). However, CMIP6 shows improvements in PA simulations in these areas, demonstrating better temporal correlation with observational data (Jian et al., 2020). These biases highlight the uncertainties in modeling cloud characteristics (Jian et al., 2020) and aerosol-cloud interaction (Bender et al., 2016). For instance, current climate models struggle to accurately simulate regional cloud distributions, leading to substantial biases in simulated shortwave irradiance (Stevens and Schwartz, 2012). Furthermore, inaccuracies in modeling the vertical structure of clouds and their overlapping characteristics significantly contribute to the uncertainties in cloud radiative effects (Li et al., 2015; Luo et al., 2023). Previous studies have also emphasized the importance of parameterizing mixed-phase clouds and supercooled water clouds (Tsushima et al., 2006; Hu et al., 2010; McCoy et al., 2015; Li et al., 2017), which are crucial for PA simulation over the Southern Ocean. Additionally, biases in CMIP6 model simulations of PA over land exhibit pronounced seasonal variations (Jian et al., 2020). For example, models significantly overestimate the PA over the TP, especially during the northern winter, primarily due to consistent overestimations of SA (Jian et al., 2020). Meanwhile, the significant underestimation of PA in Central Asia is closely related to the SA biases in the models, which persist from CMIP5 (Li et al., 2016) to CMIP6 (Jian et al., 2020). These findings indicate the need for further improvements in parameterization schemes, particularly concerning snow cover, dust aerosol, vegetation cover, and dust-cloud interactions in arid and semi-arid regions (Li et al., 2016).

Table 4
Mean hemispheric differences (NH-SH) of TOA RSR and its components for CERES and CMIP multi-model means (W m^{-2}). CERES for year 2001–2023, CMIP3 for 1980–1999, CMIP5 for 1986–2005, and CMIP6 for 1995–2014. All GCM values are derived from historical experiments. Note that our results differ slightly from those of Crueger et al., 2023, possibly due to different interpolation resolutions.

	CERES	CMIP6	CMIP5	CMIP3
$F^{\uparrow}_{TOA}$	0.02	0.92	1.16	0.66
$F^{\uparrow}_{surf}$	1.85	2.82	2.99	3.53
$F^{\uparrow}_{atm,clear}$	3.88	2.60	2.32	2.41
$F^{\uparrow}_{cloud}$	−5.71	−4.51	−4.15	−5.28

Next, we examine how well the models reproduce seasonal and interannual variability, as well as long-term trends in observed PA and RSR. Bender et al. (2006) noted that the CMIP3 models can well reproduce the seasonal cycle pattern of global mean PA, although they slightly overestimate PA during the NH summer and underestimate it in winter, which indicates challenges in simulating snow/ice cover and cloud cover. Similarly, Jian et al. (2020) evaluated the performance of CMIP6/AMIP climate models and found that they accurately simulate the annual cycle pattern of near-global (60°S-60°N) mean PA, yet consistently overestimate PA across all months. They noted that this overestimation is primarily attributed to biases in simulating the annual cycle of CAF. In addition, the overestimation of the interannual variability of RSR persists in most CMIP5 and CMIP6 models (Stephens et al., 2015; Jönsson and Bender, 2022). Regarding long-term trends, Jian et al. (2020) found a weaker decreasing trend in near-global mean PA from 2001 to 2014 across all seasons in CMIP6 compared to observations. Besides, while CMIP6 models effectively capture significant positive and negative PA trends over the ocean off the northeastern coast of Australia and the South Pacific Convergence Zone, they also simulate some unrealistic trends over both ocean and land, particularly in North America (Jian et al., 2020). These unrealistic trends can be attributed to the lack of accurate simulation of CF (Vignesh et al., 2020).

4.1.2. Simulation of hemispheric symmetry

In addition to the uncertainties in the spatiotemporal distribution and trends of PA, current state-of-the-art climate models face challenges in modeling the hemispheric symmetry of PA. We calculate the annual average hemispheric differences of all-sky RSR and its components for CMIP3 (1980–1999), CMIP5 (1986–2005), and CMIP6 (1995–2014) based on historical simulations, and compared the results with those from CERES EBAF (2001−2023), as presented in Table 4. For the mean hemispheric difference in all-sky total RSR, the model ensemble means are 0.66 W m^{-2}, 1.16 W m^{-2}, and 0.92 W m^{-2} for CMIP3, CMIP5, and CMIP6, respectively, which are significantly different from the CERES observation of 0.02 W m^{-2}. Notably, the mean hemispheric asymmetry in RSR has not shown systematic improvement across three CMIP phases (Stevens and Schwartz, 2012; Voigt et al., 2013; Stephens et al., 2015; Jönsson and Bender, 2022; Crueger et al., 2023), and is even the smallest in the earliest CMIP phase. Although some of this discrepancy can be attributed to biases in model parameterization, the analysis of CMIP model data from different periods also influences the results regarding hemispheric RSR differences. For example, the annual average hemispheric differences in RSR for the period 2001–2005 are 0.20 W m^{-2} for

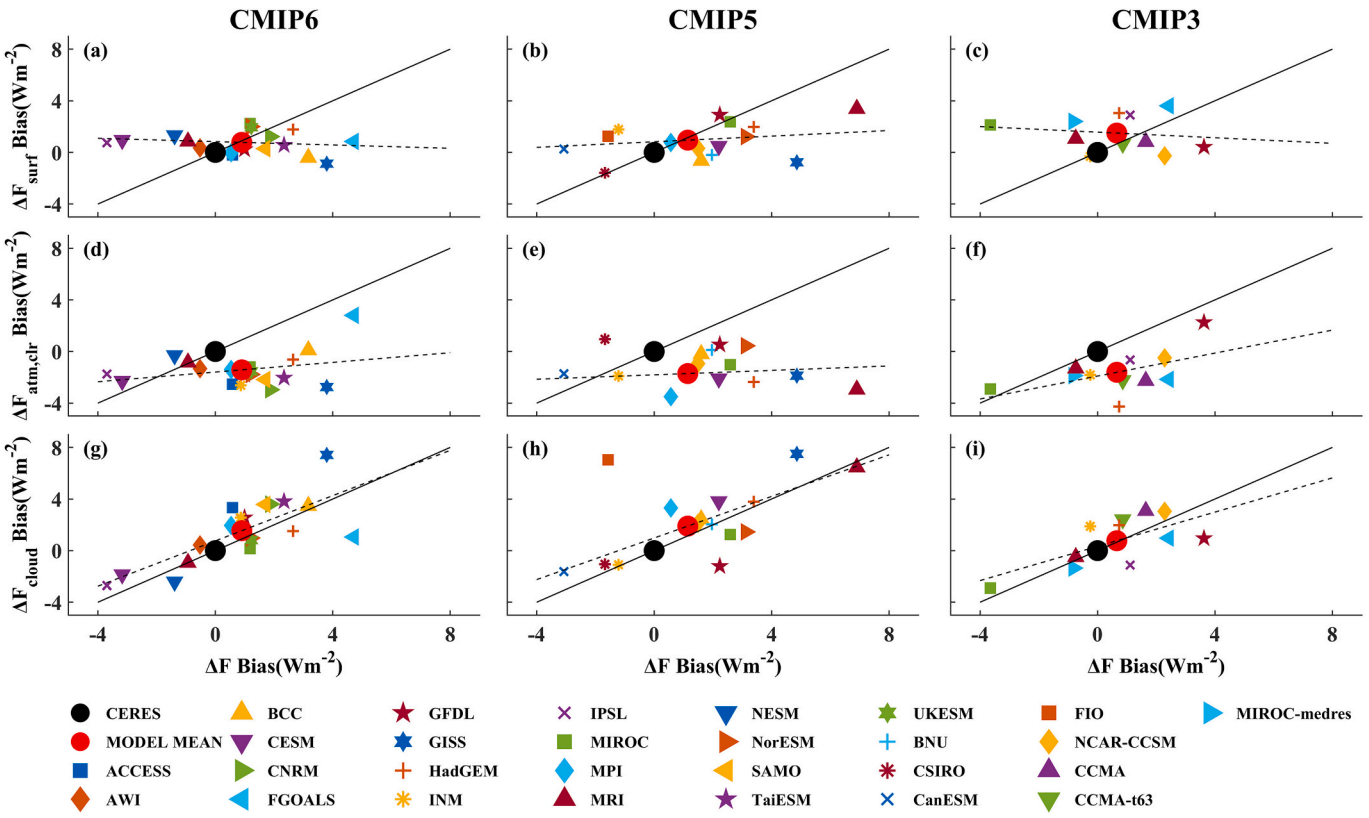

Fig. 13. Biases of hemispheric mean differences of RSR for the individual GCMs compared to CERES: all-sky total RSR vs (a-c) surface, (d-f) clear-sky atmospheric, and (g-i) cloud components for CMIP6 (left column), CMIP5 (middle column), and CMIP3 (right column). The solid line represents equality. The dashed line results from a linear regression of the points marking the individual GCMs. The red dot represents the CMIP mean, and the black dot represents CERES. [Adapted from (Crueger et al., 2023).] (For interpretation of the references to colour in this figure legend, the reader is referred to the web version of this article.)

CERES, 1.14 W m^{-2} for CMIP5, and 0.92 W m^{-2} for CMIP6. Furthermore, for the period 2001–2014, the annual average hemispheric differences in RSR for CERES and CMIP6 are 0.14 W m^{-2} and 0.79 W m^{-2}, respectively. In both of these same periods, CMIP6 exhibits smaller biases compared to CERES relative to the different periods presented in Table 4.

The challenges in capturing the hemispheric symmetry of PA may arise from the models' inability to accurately simulate the components of PA and quantify their contributions (Diamond et al., 2022), especially at local scales (Stephens et al., 2015). Compared to cloud and clear-sky atmospheric components, CMIP models have made great progress in simulating the surface component, with a reduction of mean hemispheric differences (Table 4). However, Crueger et al. (2023) found no improvement in the model-simulated surface component under clear-sky conditions from CMIP5 to CMIP6 compared to CERES. Therefore, they suggested that the reduction in the biases of the all-sky surface component in CMIP is primarily due to the presence of clouds, which mitigates the hemispheric asymmetry caused by the clear-sky surface. In Table 4, it is clear that the hemispheric asymmetry of the clear-sky atmospheric component simulated by CMIP is much lower than that observed in CERES, which may be due to the underestimation of anthropogenic aerosols in the NH or the overestimation of sea salt aerosols over the Southern Ocean in the models (Crueger et al., 2023). Besides, although CMIP models capture a larger cloud component in the SH compared to NH (resulting in a negative hemispheric difference), the hemispheric asymmetry of the cloud component remains relatively weak compared to CERES (Table 4). Fig. 13 illustrates the biases in the average hemispheric differences of the RSR compared to the three components of each GCM relative to CERES. It shows that these models not only fail to reproduce the hemispheric symmetry but also struggle to accurately determine which hemisphere is brighter (Voigt et al., 2013). There is a larger spread among different models in simulating hemispheric differences of the cloud component than in the surface and clear-sky atmospheric components. The correlation between the biases in the hemispheric differences of RSR and those of the surface or clear-sky atmospheric components is weak or even negative. However, the linear regression slope between the bias in hemispheric differences of RSR and those of the cloud component is close to 1, which indicates that the bias in total hemispheric RSR asymmetry is mainly due to the bias in the cloud component, especially in CMIP6. Regional analysis also indicated that the bias in the hemispheric differences in RSR across the three CMIP phases primarily originates from the cloud component in the tropics and around 60° (Crueger et al., 2023). Even though the NH tropics reflect more solar radiation than the SH tropics (Fig. 10c), CMIP6 models tend to exhibit a more symmetric tropical shortwave reflectance between the two hemispheres (Jönsson and Bender, 2022). The simulated biases in the extratropical regions (significantly negative in the SH and slightly positive in the NH) are the main contributors to the overall RSR asymmetry bias (Crueger et al., 2023). Additionally, hemispheric differences in RSR and its components across the three CMIP phases exhibit a latitudinal dependence similar to that of CERES, with CMIP6 demonstrating the best performance (Crueger et al., 2023).

In summary, while the spatiotemporal and hemispheric symmetry features of PA and RSR simulated by the CMIP6 model still show biases compared to CERES observations, improvements have been noted over the previous two phases. These enhancements primarily involve better reproduction of seasonal cycles (Jian et al., 2020) and more accurate simulation of regional and latitudinal distributions (Jian et al., 2020; Crueger et al., 2023). Future efforts should focus on improving parameterization schemes for atmospheric contributions, particularly cloud contributions, as they represent a significant source of inter-model spread in PA and RSR simulations (Donohoe and Battisti, 2011;

Södergren and McDonald, 2022; Crueger et al., 2023).

4.2. Future projection

Over the past two decades, the significant decline in TOA RSR has become a primary source of increased net radiation absorption and exacerbated EEI (Trenberth and Fasullo, 2009; Loeb et al., 2021a; Raghuraman et al., 2021; Hodnebrog et al., 2024; Loeb et al., 2024), contributing to changes in the climate system, as evidenced by rising surface temperature, rising sea levels, increased ocean heat content, and melting ice and snow (Hansen et al., 2005; Trenberth et al., 2014; Von Schuckmann et al., 2016; Forster et al., 2021; Loeb et al., 2021a). Against this backdrop, investigating the future evolution of PA and the maintenance or disruption of hemispheric symmetry may provide valuable insights for predicting energy budgets and climate change pathways.

In recent years, many studies have evaluated the possibility of future changes in RSR from different perspectives. For instance, Trenberth and Fasullo (2009) used CMIP3 data to trace the response of TOA radiation to the increase of greenhouse gases, such as carbon dioxide, from 1950 to 2100. They found that the increase of solar radiation absorption by the earth-atmosphere system in this century is attributed to a decrease in cloud cover in mid- and low-latitude regions. Specifically, there is a reduction in high cloud cover at low latitudes, while the reduction in mid-cloud cover is more pronounced in the subtropics and mid-latitudes. They also showed that low cloud cover will increase near 60°S, reflecting a poleward shift in storm tracks, while mid- to high-level clouds in polar regions also will increase. Furthermore, based on CMIP3 models, Bender (2011) investigated the anomalies in global average PA under scenarios where CO_2 levels increased by 1 % to quadrupling during the 20th century. All models demonstrated a decline in global average albedo, and as the forcing and temperature changes stabilized, the trend of decreasing albedo also tended to stabilize. They noted that the retreat of ice and snow, as well as changes in CF, significantly contributed to the decrease in albedo; however, there are substantial inter-model differences in the magnitude and sign of the cloud response. Besides, Diamond et al. (2022) analyzed the dynamic changes in clear-sky hemispheric asymmetry under various emission scenarios based on CMIP6. They demonstrated that under low-emission scenarios, reductions in anthropogenic aerosols could weaken the current clear-sky albedo asymmetry, while under high-emission scenarios, the reduction in snow and ice cover in the NH similarly diminishes this asymmetry. Recently, Hadas et al. (2023) projected a future decrease of mid-latitude cloud albedo in both hemispheres using the CMIP6 models. The reduction in the NH is attributed to a general decline in baroclinicity, while the decline in the SH is related to an increase in the skewness of the baroclinic activity distribution. In addition, Rugenstein and Hakuba (2023) focused on the responses of surface temperature and RSR to changes in carbon dioxide and aerosols. They pointed out that the albedo symmetry may be a function of the current climate state, including

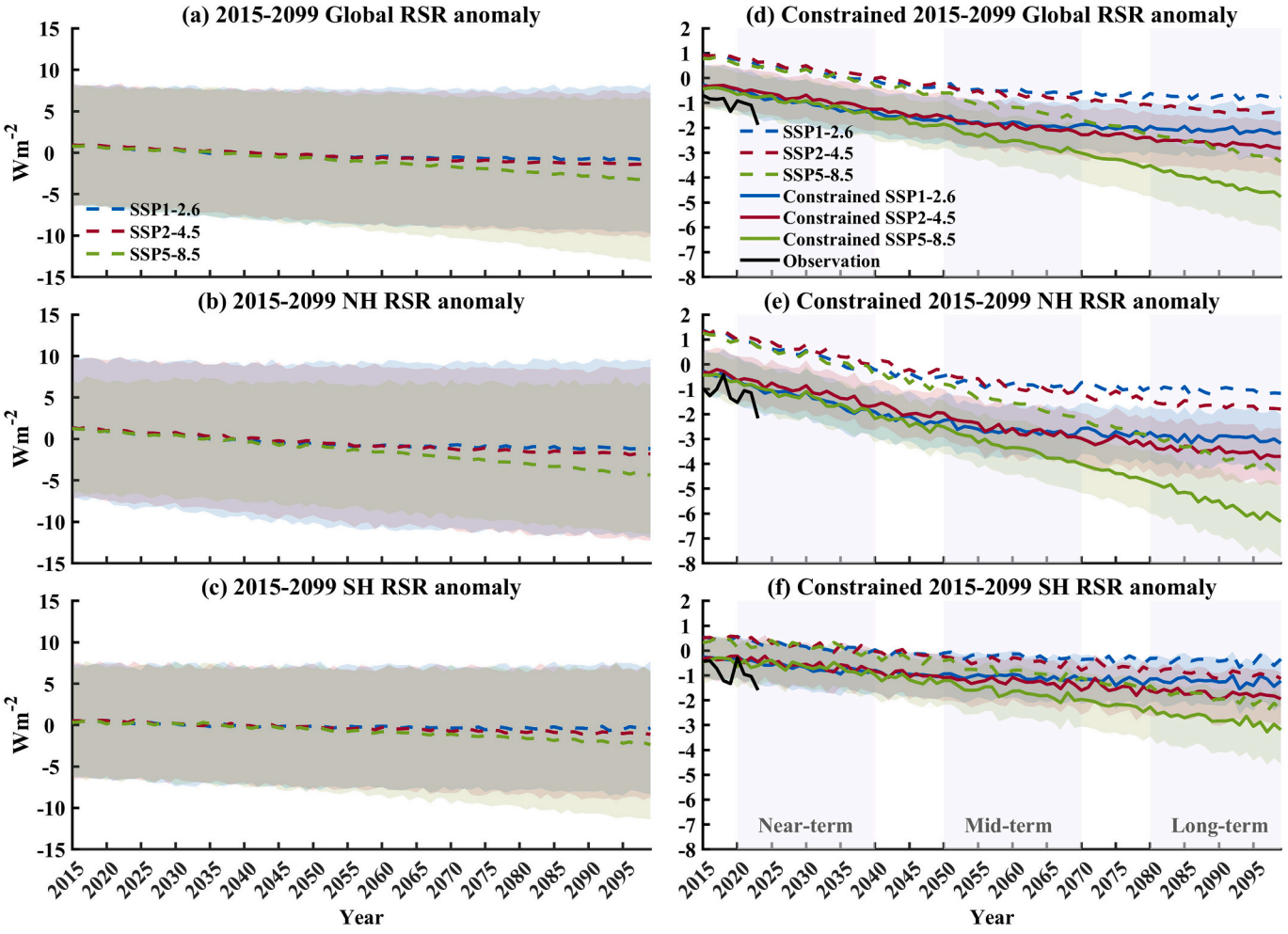

Fig. 14. Time series of RSR anomalies simulated by the CMIP6 model ensemble for 2015–2099 relative to the observation baseline (2001–2014): (a) global, (b) NH, and (c) SH. Dashed and solid lines represent the model anomalies under the SSP1–2.6 (blue), SSP2–4.5 (yellow), and SSP5–8.5 (red) scenarios before and after emergent constraint, respectively. The shaded areas indicate their uncertainty range. The solid black line is the observation (CERES-EBAF). (For interpretation of the references to colour in this figure legend, the reader is referred to the web version of this article.)

Table 5
Decadal trends of constrained RSR for the SH, NH, and globe based on CMIP6 for various time periods under different emission scenarios (W m^{-2} $decade^{-1}$).

Emission scenario	Time period	Global	NH	SH
SSP1–2.6	2015–2099	**−0.20**	**−0.30**	**−0.11**
	Near-term	**−0.43**	**−0.60**	**−0.25**
	Mid-term	**−0.14**	**−0.20**	**−0.09**
	Long-term	**−0.08**	−0.08	−0.07
SSP2–4.5	2015–2099	**−0.31**	**−0.42**	**−0.20**
	Near-term	**−0.38**	**−0.52**	**−0.24**
	Mid-term	**−0.28**	**−0.39**	**−0.14**
	Long-term	**−0.18**	**−0.22**	**−0.13**
SSP5–8.5	2015–2099	**−0.52**	**−0.70**	**−0.34**
	Near-term	**−0.42**	**−0.63**	**−0.19**
	Mid-term	**−0.53**	**−0.70**	**−0.34**
	Long-term	**−0.62**	**−0.83**	**−0.38**

Note. **Bold** indicates trend is above the 95 % confidence level.

hemispheric differences in surface temperatures and warming rates. Thus, they predicted that under strong carbon dioxide forcing and weak aerosol forcing conditions, the warming difference between the two hemispheres will intensify, with the warmer hemisphere (which here refers to the NH) becoming darker, indicating it may be possible for albedo to become hemispherically asymmetric in the future. Overall, the dynamics of clouds, snow, and ice cover, and carbon dioxide play a crucial yet uncertain role in the future evolution of albedo.

Despite the significant uncertainties and spread among current climate models, they remain a powerful tool for understanding future climate change. To reduce uncertainties in model simulations, we employ an emergent constraint approach (Cox et al., 2018; Hall et al., 2019; Brient, 2020; He et al., 2023) to constrain the projected future RSR under different Shared Socioeconomic Pathways (SSPs) (See Appendix C for detailed methodology and datasets). We establish a robust linear relationship between the historical simulated bias of RSR (2001–2014) and the future projections of annual mean RSR from CMIP6 models across three future scenarios (2015–2099), which allows us to derive constrained future RSR when the bias is zero. The constrained uncertainty range is determined by combining the uncertainty from the model regression with the uncertainty from observations, as detailed in Appendix C (He et al., 2023). Fig. 14 presents the time series of global and hemispheric annual anomalies in RSR from 2015 to 2099 (relative to observation climatology of 2001–2014) under the SSP1–2.6, SSP2–4.5, and SSP5–8.5 emission scenarios with and without applying constraints, along with their uncertainty ranges. Results indicate that the constrained RSR is generally lower than the original ones. Initially, the global and hemispheric average RSR are slightly higher than the baseline in 2015–2025, but after the constraints are applied, they fall below the baseline, which is more in line with observations. Notably, the constrained approach effectively reduces by about 76 % of the uncertainty range in future model simulations, which makes the projected results more reliable.

From 2015 to 2099, global and hemispheric RSR shows significant downward trends across all three emission scenarios (Table 5). Spatially, this decrease may be more pronounced across broad land areas and the North Pacific due to reduced cloud cover (Luo et al., 2023; Yamamoto et al., 2024), and along coastal regions of the poles due to sea ice melt. Conversely, increased RSR may occur in the equatorial Pacific and around 60°S due to increased high cloud cover (Luo et al., 2023). This could be related to the southward shift of the ITCZ (Mamalakis et al., 2021; Dhage and Widlansky, 2022) and storm tracks (Bender et al., 2012; Tselioudis et al., 2024) in response to warming. Notably, the constrained RSR anomalies in the NH differ more obviously from the unconstrained values (Fig. 14e) compared to those in the SH (Fig. 14f), suggesting greater model bias in this hemisphere. Additionally, the NH exhibits a faster decline in RSR, approximately two to three times that of the SH under the same emission scenarios (Table 5). Since the NH has more aerosol sources, emissions reductions may have a more pronounced effect in this hemisphere, leading to a faster decrease in RSR under the SSP1–2.6 scenario. Conversely, under high emission scenarios with higher global temperatures, the NH is likely to experience more rapid losses in Arctic sea ice and land ice cover compared to Antarctic sea ice (Diamond et al., 2022). Additionally, the NH is expected to see a more substantial reduction in low- and mid-level clouds over both land and ocean (Luo et al., 2023), which may further contribute to the decline in RSR. Therefore, the model ensemble average shows increased hemispheric asymmetry in RSR under the three scenarios. However, it remains uncertain whether the hemispheric symmetry of PA will be maintained in the future, as different models may exhibit varying cloud responses to warming. Furthermore, if the hemispheric symmetry of PA is indeed an inherent characteristic of the Earth-atmosphere system, the increasing hemispheric RSR differences noted in models suggest an urgent need to enhance the model simulation in the contributions of different RSR components, and the observed hemispheric PA symmetry can serve as a constraint to further reduce the simulation biases as well as improve model parameterization.

Furthermore, we categorize future periods into the near-term (2020–2040), mid-term (2050–2070), and long-term (2080–2099) to examine their differences. The trends of these different periods under different emission scenarios are shown in Table 5. The results indicate that the RSR under the three emission scenarios is quite similar in the near-term (Fig. 14d-f). In the mid-term, the global and hemispheric RSR under the SSP5–8.5 scenario diverge from the other two scenarios (Fig. 14d-f) and decrease at a faster rate (Table 5). The RSR for SSP2–4.5 and SSP1–2.6 show similar magnitude and variations, but the former declines more rapidly. In the long-term, higher emission scenarios exhibit lower global and hemispheric average RSR and faster downward trends. And under the SSP1–2.6 scenario, the downward trend of the long-term average RSR in the SH and the NH is not significant at the 95 % confidence level. Overall, the declining trend of RSR under SSP1–2.6 and SSP2–4.5 scenarios gradually slows from the beginning to the end of this century, while it accelerates under the SSP5–8.5 scenario (Table 5). Under high emission scenarios, while air pollution control measures have effectively reduced aerosols such as sulfate (Riahi et al., 2017; IPCC, 2021), the warming induced by the substantial emission of greenhouse gases may trigger multiple responses in clouds (Luo et al., 2023; Yamamoto et al., 2024) and the cryosphere (Diamond et al., 2022). The specific reasons behind this phenomenon remain unclear and require further investigation.

5. Discussion and outlook

PA and RSR are key parameters in the Earth's energy balance, shaping the global temperature distribution, atmospheric and ocean circulation, and multiple climate feedbacks, which are critical for maintaining the habitability of the planet. Therefore, a systematic understanding of the multi-temporal and spatial scale variability characteristics of Earth's PA and RSR and their driving mechanisms is essential for comprehending energy balance and climate change. Here, we systematically review the spatial and temporal evolution of the PA and RSR over the past two decades (Section 2), along with its impact factors and underlying mechanisms (Section 3). We also analyze the biases present in climate model simulations including the spatio-temporal characteristics of PA and the hemispherical symmetry characteristics (Section 4). The close relationship between clouds and energy balance is widely recognized, and accurately describing cloud feedback is a core uncertainty in climate modeling and crucial for climate predictions. By employing emergent constraint strategies, we effectively reduce uncertainty in future predictions of RSR on global and hemispheric scales (Section 4). Our results exhibit a significant downward trend in RSR throughout this century. In the long-term, this trend slows under the SSP1–2.6 and SSP2–4.5 emission scenarios, while it accelerates under the SSP5–8.5 scenario. Nevertheless, our current understanding remains limited, and many aspects require further exploration and investigation.

5.1. Is the hemispheric symmetry of PA also robust in paleoclimate?

As research into the hemispheric symmetry of PA deepens, a natural question arises: Has this characteristic existed throughout history, particularly under paleoclimatic conditions? If the answer is affirmative, it would strongly support the view that "hemispheric symmetry of PA is an inherent characteristic of the Earth system." However, key factors influencing PA, such as land-sea distribution, atmospheric gas composition, aerosol composition, and cloud distribution, have undergone significant changes over time. Namely, the fragmentation and drift of continental plates have shaped the current distribution of land and oceans (Wegener and Vogel, 1980; Romano and Cifelli, 2015); the gradual formation of permanent ice sheets at the poles has occurred (Robin, 2010); there has been a transition from natural aerosol distributions to increased anthropogenic pollution (Mahowald et al., 2024); and the distribution of cloud cover has changed significantly in response to variations in land-sea distribution and surface temperatures (Woods, 2005). These factors complicate our understanding of hemispheric differences in PA. In particular, it is still challenging to obtain the paleoclimatic radiation data on a global scale. Meanwhile, reconstructions of palaeo-cloud cover are very limited (Young et al., 2010; Helama et al., 2018; Young et al., 2019), and there exist significant uncertainties in cloud parameterization within paleoclimate models (Thompson and Barron, 1981; Young et al., 2010). For example, using an ensemble of climate simulations over the past 540 million years, Han et al. (2023) pointed out that, on geological timescales, the land-sea albedo contrast largely determines the hemispheric differences in solar radiation absorption, with clouds playing a minimal role, which is contradictory with our current understanding. Therefore, it is challenging to determine whether the hemispheric PA symmetry is robust in paleoclimate.

5.2. Radiation products with high spatial and temporal resolution and long-time records require higher accuracy

The relatively short observation record of CERES EBAF data limits the investigation of long-term variations in PA and RSR, as well as the evolution of hemispheric symmetry. Although the application of multispectral narrowband sensors and many innovative methods have significantly extended the observation records and improved the spatio-temporal resolution, the accuracy and consistency of these radiation products are still insufficient to support related studies. Li et al. (2024) have systematically analyzed the hemispheric RSR differences among several datasets, including Cloud_cci AVHRR PMv3, ISCCP, ERA5, and MERRA-2. Notably, only AVHRR can establish RSR hemispheric symmetry over a period exceeding 14 years within its uncertainty range, while the other datasets are unable to exhibit hemispheric symmetry under different symmetry criteria. They also assessed biases in these datasets compared to CERES EBAF and explored potential causes. The performance of different datasets was evaluated by calculating the Euclidean distance between indices of simulation and observation (DISO), which is calculated using time correlation coefficients, absolute deviations, and root mean square errors, with a lower value indicating better consistency with observation (Hu et al., 2022). Their results showed that the AVHRR dataset exhibits the lowest DISO value, suggesting greater consistency with CERES regarding hemispheric RSR symmetry. However, great biases are observed in the hemispheric differences of various components for AVHRR compared to CERES. For instance, in the NH, AVHRR data may misidentify high aerosol loads as clouds, resulting in a lower clear-sky atmospheric component compared to CERES and a lower hemispheric asymmetry of the clear-sky atmospheric component. In contrast, MERRA-2 performs the worst in terms of hemispheric symmetry of RSR among these datasets, exhibiting a large positive bias in cloud components relative to CERES in the tropics and SH mid-latitudes, which reflects its shortcomings in cloud parameterization and data assimilation (Hinkelman, 2019; Kuma et al., 2020; Yao et al., 2020). Furthermore, none of these datasets effectively captures the long-term trends of hemispheric mean RSR and its components. Regionally, both AVHRR and ISCCP display some spurious trends; the former is likely influenced by satellite orbital drift, which increases SZA due to delayed overpass times, while the latter may be related to changes in the geostationary satellite platform (Evan et al., 2007). Calibration is necessary before conducting trend analyses with these datasets. In summary, the parameterization schemes of the radiative transfer models used in these long-term radiation datasets require further improvement to enhance their usability.

5.3. Impact of Decreased Earth's PA and what can be done to stabilize it?

Over the past two decades, the increasing variability and significant decline in PA and RSR have intensified the climate crisis. On one hand, this decline has contributed to the rise in the EEI, indicating an increase in net energy absorption (Trenberth and Fasullo, 2009; Loeb et al., 2021a; Raghuraman et al., 2021; Hodnebrog et al., 2024; Loeb et al., 2024). On the other hand, it has amplified the increase in global average temperatures (Ripple et al., 2023; Nikolov and Zeller, 2024) and enhanced atmospheric instability in the NH (Chen and Dai, 2023). Consequently, the oceans are warming, sea levels are rising, and the melting of ice and snow in polar and high-altitude regions is accelerating (Swart et al., 2018; Hobbs et al., 2021; Turner et al., 2022; Purich and Doddridge, 2023; Huang et al., 2024; Kuhlbrodt et al., 2024; Roach and Meier, 2024). Meanwhile, the earth is experiencing extreme heat events, heat waves, and extreme precipitation events, all of which threaten human life and property (Luber and McGeehin, 2008; Horton et al., 2016; Hong et al., 2019; Gimeno et al., 2022; Ripple et al., 2023). Recent temperature anomalies have attracted widespread attention. In 2023, the global average surface temperature was 1.48 ± 0.06 K higher than the pre-industrial levels according to ERA5 (Goessling et al., 2024), exceeding the previous high record by 0.17 K. While earlier studies attributed this increase mainly to human greenhouse gas emissions and internal variability (IPCC, 2021), these factors alone cannot fully explain such extreme temperatures (IPCC, 2021; Raghuraman et al., 2024; Schmidt, 2024). A recent study pointed out that the record-low PA can account for 0.22 K (±0.04 K) of the 2023 temperature anomaly (Goessling et al., 2024). This perspective has been overlooked in previous research, yet it is crucial for understanding the intensifying extreme events we are currently facing. PA, temperature, and precipitation are interconnected climate factors, making it challenging to clearly distinguish their causal relationships. However, the ongoing decline in PA and its impact on extreme heat and precipitation is an urgent topic that needs to be addressed. More importantly, according to future projections (Fig. 14), the decline in RSR may continue throughout this century, highlighting the urgency of addressing this trend. In response to the escalating climate crisis, climate geoengineering has emerged as a topic of extensive discussion and controversy (Shepherd, 2009; Mercer et al., 2011). Solar Radiation Management is one of the major proposed approaches aimed at reducing the amount of solar radiation absorbed by the Earth, thereby offsetting the increased infrared radiation emissions resulting from global warming related to rising greenhouse gas levels (Wigley, 2006; Caldeira and Wood, 2008). Proposed methods include injecting sulfuric acid aerosol precursors into the stratosphere (Crutzen, 2006; Jones et al., 2010) and enhancing marine cloud brightness (Feingold et al., 2024), both of which aim to increase PA and reflect more solar radiation. While these methods may have some potential, they remain unproven and their possible negative impacts cannot be overlooked (Robock et al., 2008; Ricke et al., 2010). Given that the decline in global and hemispheric average RSR under low emission scenarios is much slower than that under high emission scenarios (Fig. 14), emission reduction may represent a more sustainable approach. Strategies such as transitioning to clean energy, enforcing strict emissions reductions, reforestation, and adopting agroecological practices, although they may not yield immediate results, offer sustainable solutions for restoring ecosystems and addressing the climate

crisis in the long term.

Declaration of competing interest

The authors declare that they have no known competing financial interests or personal relationships that could have appeared to influence the work reported in this paper.

Acknowledgements

This work was supported by the key Program of the National Natural Science Foundation of China (42430601); the National Natural Science Foundation of China (42305072); the China Postdoctoral Science Foundation (2023M731454) and Gansu Provincial Department of Education Outstanding Graduate Students "Innovation Star" Project (2025CXZX-075).

We would like to appreciate the CERES, and WCRP CMIP science teams for providing excellent and accessible data products that made this study possible. We would like to acknowledge freepik.com for supporting icons used in our schematics (www.freepik.com). We would like to thank the anonymous reviewers for their insightful comments and constructive suggestions, which have greatly improved the quality of this paper.

Appendix A. Detailed derivation of Eq. (1) and (2)

Based on the simplified radiative models, Donohoe and Battisti (2011) and Stephens et al. (2015) decomposed the all-sky RSR at the TOA into atmospheric and surface contributions (see the respective publications for detailed derivations):

$$F^{\uparrow}_{atm} \equiv Sr \tag{A1}$$

$$F^{\uparrow}_{surf} \equiv S\frac{\alpha_s t^2}{1-r\alpha_s} \tag{A2}$$

where, the intrinsic reflectance r and transmittance t of the atmosphere can be expressed as

$$r = \alpha_p - t\alpha_s T \tag{A3}$$

$$t = T\frac{1-\alpha_s\alpha_p}{1-\alpha_s{}^2T^2} \tag{A4}$$

To simplify the calculation, these quantities are expressed using directly available known variables. Substituting Eqs. (A3) and (A4) into (A1) yields:

$$F^{\uparrow}_{atm} = S\left(\alpha_p - T^2\alpha_s\frac{1-\alpha_s\alpha_p}{1-\alpha_s{}^2T^2}\right) \tag{A5}$$

Assuming that surface and atmospheric reflection and absorption processes are isotropic, the planetary albedo α_p, the transmittance of the whole Earth-atmosphere system T, and surface albedo α_s are defined as:

$$\alpha_p = \frac{F^{\uparrow}_{TOA}}{S} \tag{A6}$$

$$T = \frac{F^{\downarrow}_{S}}{S} \tag{A7}$$

$$\alpha_s = \frac{F^{\uparrow}_{S}}{F^{\downarrow}_{S}} \tag{A8}$$

Substituting these three eqs. (A6, A7, A8) into (A5) gives the expression for $F^{\uparrow}_{atm}$ solely in terms of the known TOA and surface shortwave radiative fluxes (Eq. (1) and (2)):

$$F^{\uparrow}_{atm} = \frac{S\left(SF^{\uparrow}_{TOA} - F^{\uparrow}_{S}F^{\downarrow}_{S}\right)}{S^2 - F^{\uparrow}_{S}{}^2}$$ ((A9, same as Eq. (1))

$$F^{\uparrow}_{surf} = F^{\uparrow}_{TOA} - F^{\uparrow}_{atm} = F^{\uparrow}_{TOA} - \frac{S\left(SF^{\uparrow}_{TOA} - F^{\uparrow}_{S}F^{\downarrow}_{S}\right)}{S^2 - F^{\uparrow}_{S}{}^2}$$ ((A10, same as Eq. (2))

Appendix B

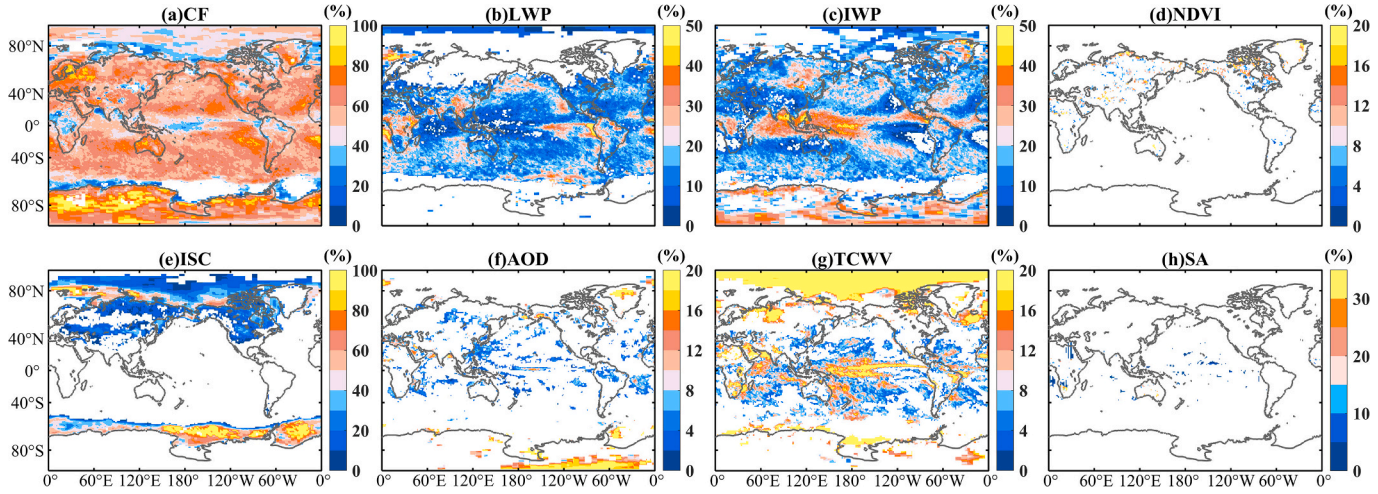

Fig. B1. The global distributions of the relative contributions of (a) CF, (b) LWP, (c) IWP, (d) NDVI, (e) ISC, (f) AOD, (g)TCWV and (h) SA to RSR from the stepwise multiple linear regression models [Adapted from Jian et al., 2018]. Those regions without values indicate that the variable is not considered as a predictor variable in the regression model

Appendix C. Emergent constraint

To predict future RSR in response to severe climate change risks, we analyze CMIP6 projections of RSR from 2015 to 2099 based on various emission scenarios that reflect policy impacts and socio-economic risks. SSP1–2.6 assumes a sustainable future, achieving a radiative stabilization of 2.6 Wm^{-2} beyond 2100. SSP2–4.5 represents an intermediate challenges scenario, stabilizing radiative forcing at 4.5 Wm^{-2} after 2100. In contrast, SSP5–8.5 depicts a highly challenging scenario characterized by heavy reliance on fossil fuels, resulting in a peak in emissions by 2080 and a radiative forcing of 8.5 Wm^{-2} by 2100. These emission scenarios offer valuable possibilities for estimating RSR, but climate predictions remain uncertain due to internal variability, model limitations, and scenario differences. To reduce the uncertainty of model simulation, we employ an observation-based emergent constraint method using linear regression. This approach minimizes projection uncertainty by identifying robust relationships between historical model simulations and future predictions.

Table C1
CMIP6 models used for emergent constraint in Fig. 14.

Model name	Model name
ACCESS_CM2	INM_CM4_8
ACCESS_ESM1_5	INM_CM5_0
BCC_CSM2_MR	IPSL_CM6A_LR
CESM2_WACCM	KIOST_ESM
CMCC_CM2_SR5	MIROC6
CanESM5	MPI_ESM1_2_HR
FGOALS_f3_L	MPI_ESM1_2_LR
IITM_ESM	MRI_ESM2_0
NorESM2_LM	TaiESM1

Specifically, we use the multi-year average bias of RSR between a model historical ensemble (18 GCMs from CMIP6: Table C1) from 2001 to 2014 and observations (CERES EBAF) as the independent variable (x), while the annual average RSR of the models under different scenarios (2015–2099) served as the dependent variable (y). A linear regression can be established:

$$y = ax + b$$

where a is the regression slope and b is the intercept. When $x = 0$ (i.e., bias is zero), the intercept is regarded as the constrained future RSR. Note specifically that the constraint is applied to absolute values of future RSR, rather than trends or changes in RSR, for which the global-mean bias in RSR provides only a weak constraint (not shown).

This study employs a bootstrap-based statistical framework to quantify the uncertainty in constrained climate model projections of future RSR. First, to address the parameter uncertainty, we perform 1000 bootstrap resamplings of the CMIP6 model ensemble, drawing a sample of the same size as the original ensemble (with replacement) each time. For each subsample, we refit a regression model relating historical biases to future annual-mean RSR, generating distributions of regression coefficients (a, b) that characterize the variability in model parameter estimation. Second, to assess the uncertainty in the observed climatology, we perform 1000 bootstrap resamplings of the RSR observational data (2001–2014), creating a probability distribution of the observed mean. By jointly considering parameter and observational uncertainties, we calculate the constrained future projections for each combination of parameter and observational bootstrap samples. Finally, we construct a probability density function using Gaussian kernel density estimation of the entire set of bootstrap results. The 5th and 95th percentiles are extracted to define the 90 % confidence interval, and its mean serves as the optimal estimate. Fig. C1 illustrates the effect of the constraint and displays the constrained uncertainty range. It shows the models' historical simulation biases (2001–2014) versus the future climatology of RSR (2015–2099), along with the constrained uncertainty range of the regression model and observation. The blue shading is the 90 % confidence interval of the linear regression obtained by bootstrapping the

18 models for 1000 times. The green shading is the probability density function derived from the difference between the observational climatology and the bootstrap samples of the observational data. It should be noted that the future climatology of RSR is used here only as a demonstration. In practice, our study constrains the annual mean RSR for each year from 2015 to 2099. The mean reduction in the uncertainty range of the future projected RSR estimates for the global/NH/SH, which correspond to reductions of 76.5 %, 76.0 %, 75.2 %/ 78.9 %, 78.5 %, 77.5 %/ 74.9 %, 74.3 %, 73.4 % under the SSP1–2.6, SSP2–4.5, and SSP5–8.5 scenarios.

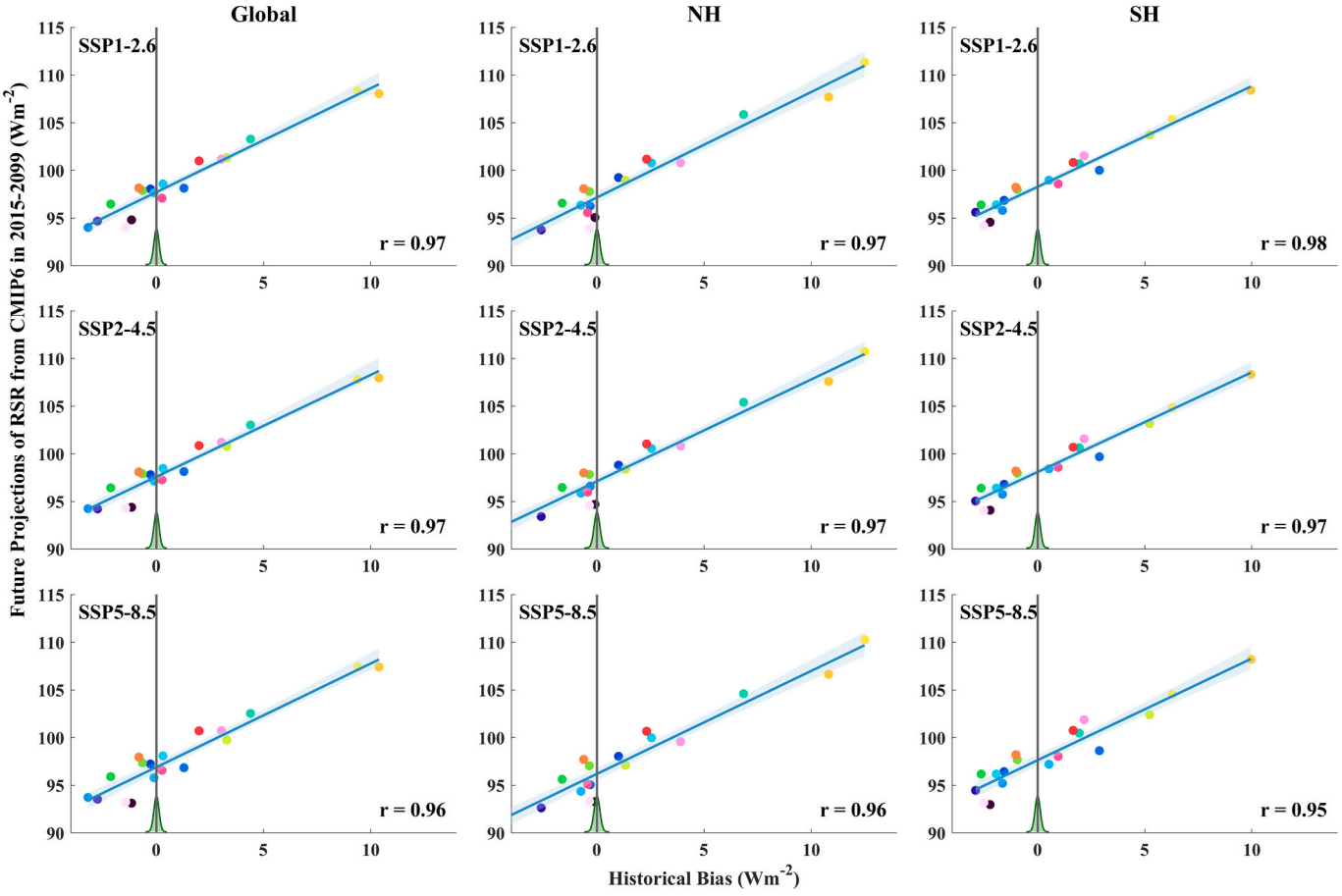

Fig. C1. Constrained projection of RSR in three future scenarios using observations. The colored dots show the historical biases in RSR (2001–2014) versus the future climatology of RSR (2015–2099) for the 18 models, across global, NH, and SH. The blue line indicates the constrained relationship and the blue shading indicates the 90 % confidence intervals estimated by bootstrap. "r" is the correlation coefficient ($p < 0.1$). The black vertical line marks zero bias and its probability density function is derived from the difference between the observational climatology and the bootstrap samples of the observational data for the period 2001–2014.

Data availability

Data will be made available on request.

References

Ackerman, A.S., Kirkpatrick, M.P., Stevens, D.E., Toon, O.B., 2004. The impact of humidity above stratiform clouds on indirect aerosol climate forcing. Nature 432 (7020), 1014–1017. https://doi.org/10.1038/nature03174.

Albrecht, B.A., 1989. Aerosols, cloud microphysics, and fractional cloudiness. Science 245 (4923), 1227–1230. https://doi.org/10.1126/science.245.4923.1227.

An, L., Che, H., Xue, M., Zhang, T., Wang, H., Wang, Y., Zhou, C., Zhao, H., Gui, K., Zheng, Y., 2018. Temporal and spatial variations in sand and dust storm events in East Asia from 2007 to 2016: Relationships with surface conditions and climate change. Sci. Total Environ. 633, 452–462. https://doi.org/10.1016/j.scitotenv.2018.03.068.

Andersen, H., Cermak, J., Zipfel, L., Myers, T.A., 2022. Attribution of observed recent decrease in low clouds over the Northeastern Pacific to cloud-controlling factors. Geophys. Res. Lett. 49 (3), e2021GL096498. https://doi.org/10.1029/2021GL096498.

Ångström, A., 1962. Atmospheric turbidity, global illumination and planetary albedo of the earth. Tellus 14 (4), 435–450. https://doi.org/10.3402/tellusa.v14i4.9570.

Bala, G., Caldeira, K., Wickett, M., Phillips, T., Lobell, D., Delire, C., Mirin, A., 2007. Combined climate and carbon-cycle effects of large-scale deforestation. Proc. Natl. Acad. Sci. 104 (16), 6550–6555. https://doi.org/10.1073/pnas.0608998104.

Bala, G., Caldeira, K., Nemani, R., Cao, L., Ban-Weiss, G., Shin, H.-J., 2011. Albedo enhancement of marine clouds to counteract global warming: impacts on the hydrological cycle. Clim. Dyn. 37, 915–931. https://doi.org/10.1007/s00382-011-1256-1.

Balmes, K.A., Fu, Q., 2020. The diurnally-averaged aerosol direct radiative effect and the use of the daytime-mean and insolation-weighted-mean solar zenith angles. J. Quant. Spectrosc. Radiat. Transf. 257, 107363. https://doi.org/10.1016/j.jqsrt.2020.107363.

Barkstrom, B.R., 1984. The earth radiation budget experiment (ERBE). Bull. Am. Meteorol. Soc. 65 (11), 1170–1185. https://doi.org/10.1175/1520-0477(1984)065%3C1170:TERBE%3E2.0.CO;2.

Barkstrom, B.R., Smith, G.L., 1986. The earth radiation budget experiment: Science and implementation. Rev. Geophys. 24 (2), 379–390. https://doi.org/10.1029/RG024i002p00379.

Barnes, C.A., Roy, D.P., 2008. Radiative forcing over the conterminous United States due to contemporary land cover land use albedo change. Geophys. Res. Lett. 35 (9). https://doi.org/10.1029/2008GL033567.

Bauer, S.E., Menon, S., 2012. Aerosol direct, indirect, semidirect, and surface albedo effects from sector contributions based on the IPCC AR5 emissions for preindustrial and present-day conditions. J. Geophys. Res. Atmos. 117 (D1). https://doi.org/10.1029/2011JD016816.

Bellouin, N., Quaas, J., Gryspeerdt, E., Kinne, S., Stier, P., Watson-Parris, D., Boucher, O., Carslaw, K.S., Christensen, M., Daniau, A.L., 2020. Bounding global aerosol radiative forcing of climate change. Rev. Geophys. 58 (1), e2019RG000660. https://doi.org/10.1029/2019RG000660.

Bender, F.A., 2011. Planetary albedo in strongly forced climate, as simulated by the CMIP3 models. Theor. Appl. Clim. 105, 529–535. https://doi.org/10.1007/s00704-011-0411-2.

Bender, F.A.-M., Rodhe, H., Charlson, R.J., Ekman, A.M., Loeb, N., 2006. 22 views of the global albedo—comparison between 20 GCMs and two satellites. Tellus A: Dyn. Meteorol. Oceanogr. 58 (3), 320–330. https://doi.org/10.1111/j.1600-0870.2006.00181.x.

Bender, F.A., Ramanathan, V., Tselioudis, G., 2012. Changes in extratropical storm track cloudiness 1983–2008: Observational support for a poleward shift. Clim. Dyn. 38, 2037–2053. https://doi.org/10.1007/s00382-011-1065-6.

Bender, F.A.-M., Engström, A., Karlsson, J., 2016. Factors controlling cloud albedo in marine subtropical stratocumulus regions in climate models and satellite observations. J. Clim. 29 (10), 3559–3587. https://doi.org/10.1175/JCLI-D-15-0095.1.

Bender, F.A.-M., Engström, A., Wood, R., Charlson, R.J., 2017. Evaluation of hemispheric asymmetries in marine cloud radiative properties. J. Clim. 30 (11), 4131–4147. https://doi.org/10.1175/JCLI-D-16-0263.1.

Benestad, R.E., 2006. Earth's Climate. Springer. https://doi.org/10.1007/3-540-30621-8_5.

Bergman, J.W., Salby, M.L., 1997. The role of cloud diurnal variations in the time-mean energy budget. J. Clim. 10 (5), 1114–1124. https://doi.org/10.1175/1520-0442(1997)010%3C1114:TROCDV%3E2.0.CO;2.

Betts, R.A., Falloon, P.D., Goldewijk, K.K., Ramankutty, N., 2007. Biogeophysical effects of land use on climate: Model simulations of radiative forcing and large-scale temperature change. Agric. For. Meteorol. 142 (2–4), 216–233. https://doi.org/10.1016/j.agrformet.2006.08.021.

Bhatti, Y.A., Revell, L.E., McDonald, A.J., 2022. Influences of Antarctic ozone depletion on southern ocean aerosols. J. Geophys. Res. Atmos. 127 (18), e2022JD037199. https://doi.org/10.1029/2022JD037199.

Blanco, J.E., Caballero, R., Datseris, G., Stevens, B., Bony, S., Hadas, O., Kaspi, Y., 2023. A cloud-controlling factor perspective on the hemispheric asymmetry of extratropical cloud albedo. J. Clim. 36 (6), 1793–1804. https://doi.org/10.1175/JCLI-D-22-0410.1.

Bonan, G.B., 2008. Forests and climate change: forcings, feedbacks, and the climate benefits of forests. Science 320 (5882), 1444–1449. https://doi.org/10.1126/science.1155121.

Boucher, O., 1998. On aerosol direct shortwave forcing and the Henyey–Greenstein phase function. J. Atmos. Sci. 55 (1), 128–134. https://doi.org/10.1175/1520-0469(1998)055%3C0128:OADSFA%3E2.0.CO;2.

Bounoua, L., Collatz, G., Los, S., Sellers, P., Dazlich, D., Tucker, C., Randall, D., 2000. Sensitivity of climate to changes in NDVI. J. Clim. 13 (13), 2277–2292. https://doi.org/10.1175/1520-0442(2000)013%3C2277:SOCTCI%3E2.0.CO;2.

Box, J., Fettweis, X., Stroeve, J., Tedesco, M., Hall, D., Steffen, K., 2012. Greenland ice sheet albedo feedback: thermodynamics and atmospheric drivers. Cryosphere 6 (4), 821–839. https://doi.org/10.5194/tc-6-821-2012.

Briegleb, B., Ramanathan, V., 1982. Spectral and diurnal variations in clear sky planetary albedo. J. Appl. Meteorol. 1962-1982, 1160–1171. http://www.jstor.org/stable/26180502.

Brient, F., 2020. Reducing uncertainties in climate projections with emergent constraints: Concepts, examples and prospects. Adv. Atmos. Sci. 37 (1), 1–15. https://doi.org/10.1007/s00376-019-9140-8.

Budyko, M.I., 1969. The effect of solar radiation variations on the climate of the Earth. tellus 21 (5), 611–619. https://doi.org/10.3402/tellusa.v21i5.10109.

Caesar, L., McCarthy, G., Thornalley, D., Cahill, N., Rahmstorf, S., 2021. Current Atlantic meridional overturning circulation weakest in last millennium. Nat. Geosci. 14 (3), 118–120. https://doi.org/10.1038/s41561-021-00699-z.

Cairns, B., 1995. Diurnal variations of cloud from ISCCP data. Atmos. Res. 37 (1–3), 133–146. https://doi.org/10.1016/0169-8095(94)00074-N.

Calabrò, E., Magazù, S., 2016. Correlation between increases of the annual global solar radiation and the ground albedo solar radiation due to desertification—a possible factor contributing to climatic change. Climate 4 (4), 64. https://doi.org/10.3390/cli4040064.

Caldeira, K., Wood, L., 2008. Global and Arctic climate engineering: numerical model studies. Philos. Trans. R. Soc. A Math. Phys. Eng. Sci. 366 (1882), 4039–4056. https://doi.org/10.1098/rsta.2008.0132.

Ceppi, P., Brient, F., Zelinka, M.D., Hartmann, D.L., 2017. Cloud feedback mechanisms and their representation in global climate models. Wiley Interdiscip. Rev. Clim. Chang. 8 (4), e465. https://doi.org/10.1002/wcc.465.

Chapin III, F.S., Sturm, M., Serreze, M.C., McFadden, J.P., Key, J., Lloyd, A.H., McGuire, A., Rupp, T.S., Lynch, A.H., Schimel, J.P., 2005. Role of land-surface changes in Arctic summer warming. Science 310 (5748), 657–660. https://doi.org/10.1126/science.1117368.

Che, H., Qi, B., Zhao, H., Xia, X., Eck, T.F., Goloub, P., Dubovik, O., Estelles, V., Cuevas-Agulló, E., Blarel, L., 2018. Aerosol optical properties and direct radiative forcing based on measurements from the China Aerosol Remote Sensing Network (CARSNET) in eastern China. Atmos. Chem. Phys. 18 (1), 405–425. https://doi.org/10.5194/acp-18-405-2018.

Che, H., Xia, X., Zhao, H., Li, L., Gui, K., Zheng, Y., Song, J., Qi, B., Zhu, J., Miao, Y., 2024. Aerosol optical and radiative properties and their environmental effects in China: a review. Earth Sci. Rev. 248, 104634. https://doi.org/10.1016/j.earscirev.2023.104634.

Chen, J., Dai, A., 2023. The atmosphere has become increasingly unstable during 1979–2020 over the Northern Hemisphere. Geophys. Res. Lett. 50 (20), e2023GL106125. https://doi.org/10.1029/2023GL106125.

Chen, C., Park, T., Wang, X., Piao, S., Xu, B., Chaturvedi, R.K., Fuchs, R., Brovkin, V., Ciais, P., Fensholt, R., 2019. China and India lead in greening of the world through land-use management. Nat. Sustain. 2 (2), 122–129. https://doi.org/10.1038/s41893-019-0220-7.

Chen, L., Ding, M., She, Y., Zhang, L., Zeng, Z., Jia, J., Zheng, Y., Tian, B., Zhu, K., Wang, X., 2024. Regional aerosol optical depth over Antarctica. Atmos. Res. 308, 107534. https://doi.org/10.1016/j.atmosres.2024.107534.

Chiang, J.C., Bitz, C.M., 2005. Influence of high latitude ice cover on the marine Intertropical Convergence Zone. Clim. Dyn. 25 (5), 477–496. https://doi.org/10.1007/s00382-005-0040-5.

Chiang, J.C., Biasutti, M., Battisti, D.S., 2003. Sensitivity of the Atlantic intertropical convergence zone to last glacial maximum boundary conditions. Paleoceanography 18 (4). https://doi.org/10.1029/2003PA000916.

Christopher, S.A., Zhang, J., 2002. Shortwave aerosol radiative forcing from MODIS and CERES observations over the oceans. Geophys. Res. Lett. 29 (18). https://doi.org/10.1029/2002GL014803, 6-1-6-4.

Clement, A.C., Burgman, R., Norris, J.R., 2009. Observational and model evidence for positive low-level cloud feedback. Science 325 (5939), 460–464. https://doi.org/10.1126/science.1171255.

Comiso, J.C., Parkinson, C.L., Gersten, R., Stock, L., 2008. Accelerated decline in the Arctic Sea ice cover. Geophys. Res. Lett. 35 (1). https://doi.org/10.1029/2007GL031972.

Cox, P.M., Huntingford, C., Williamson, M.S., 2018. Emergent constraint on equilibrium climate sensitivity from global temperature variability. Nature 553 (7688), 319–322. https://doi.org/10.1038/nature25450.

Cronin, T.W., 2014. On the choice of average solar zenith angle. J. Atmos. Sci. 71 (8), 2994–3003. https://doi.org/10.1175/JAS-D-13-0392.1.

Crueger, T., Schmidt, H., Stevens, B., 2023. Hemispheric albedo asymmetries across three phases of CMIP. J. Clim. 36 (15), 5267–5280. https://doi.org/10.1175/JCLI-D-22-0923.1.

Crutzen, P.J., 2006. Albedo enhancement by stratospheric sulfur injections: a contribution to resolve a policy dilemma? Clim. Chang. 77 (3–4), 211. https://doi.org/10.1007/s10584-006-9101-y.

Cui, T., Qing, S., Wei, T., Mu, B., Xiao, Y., Chen, Y., Bao, Y., Zhang, J., 2022. Decade-low aerosol levels over the Bohai and Yellow Seas amid the COVID-19 lockdown. Int. J. Appl. Earth Obs. Geoinf. 112, 102905. https://doi.org/10.1016/j.jag.2022.102905.

Datseris, G., Stevens, B., 2021. Earth's albedo and its symmetry. AGU Adv. 2 (3), e2021AV000440. https://doi.org/10.1029/2021AV000440.

Del Genio, A.D., Kiang, N.Y., Way, M.J., Amundsen, D.S., Sohl, L.E., Fujii, Y., Chandler, M., Aleinov, I., Colose, C.M., Guzewich, S.D., 2019. Albedos, equilibrium temperatures, and surface temperatures of habitable planets. Astrophys. J. 884 (1), 75. https://doi.org/10.3847/1538-4357/ab3be8.

Dey, S., Di Girolamo, L., 2011. A decade of change in aerosol properties over the Indian subcontinent. Geophys. Res. Lett. 38 (14). https://doi.org/10.1029/2011GL048153.

Dhage, L., Widlansky, M.J., 2022. Assessment of 21st century changing sea surface temperature, rainfall, and sea surface height patterns in the tropical Pacific Islands using CMIP6 greenhouse warming projections. Earth's Future 10 (4), e2021EF002524. https://doi.org/10.1029/2021EF002524.

Diamond, M.S., 2023. Detection of large-scale cloud microphysical changes within a major shipping corridor after implementation of the International Maritime Organization 2020 fuel sulfur regulations. Atmos. Chem. Phys. 23 (14), 8259–8269. https://doi.org/10.5194/acp-23-8259-2023.

Diamond, M.S., Gristey, J.J., Kay, J.E., Feingold, G., 2022. Anthropogenic aerosol and cryosphere changes drive Earth's strong but transient clear-sky hemispheric albedo asymmetry. Commun. Earth Environ. 3 (1), 206. https://doi.org/10.1038/s43247-022-00546-y.

Diamond, M.S., Gristey, J.J., Feingold, G., CSD, E, 2024. Testing Cloud Adjustment Hypotheses for the Maintenance of Earth's Hemispheric Albedo Symmetry with Observed Trends and Natural experiments. Geophys. Res. Lett. 51 (20), e2024GL111733. https://doi.org/10.1029/2024GL111733.

Doelling, D.R., Loeb, N.G., Keyes, D.F., Nordeen, M.L., Morstad, D., Nguyen, C., Wielicki, B.A., Young, D.F., Sun, M., 2013. Geostationary enhanced temporal interpolation for CERES flux products. J. Atmos. Ocean. Technol. 30 (6), 1072–1090. https://doi.org/10.1175/JTECH-D-12-00136.1.

Donohoe, A., Battisti, D.S., 2011. Atmospheric and surface contributions to planetary albedo. J. Clim. 24 (16), 4402–4418. https://doi.org/10.1175/2011JCLI3946.1.

Doyle, J., Lesins, G., Thackray, C., Perro, C., Nott, G., Duck, T., Damoah, R., Drummond, J., 2011. Water vapor intrusions into the High Arctic during winter. Geophys. Res. Lett. 38 (12). https://doi.org/10.1029/2011GL047493.

Engström, A., Bender, F.M., Charlson, R., Wood, R., 2015. The nonlinear relationship between albedo and cloud fraction on near-global, monthly mean scale in observations and in the CMIP5 model ensemble. Geophys. Res. Lett. 42 (21), 9571–9578. https://doi.org/10.1002/2015GL066275.

Evan, A.T., Heidinger, A.K., Vimont, D.J., 2007. Arguments against a physical long-term trend in global ISCCP cloud amounts. Geophys. Res. Lett. 34 (4), L04701. https://doi.org/10.1029/2006GL028083.

Eyring, V., Bony, S., Meehl, G.A., Senior, C.A., Stevens, B., Stouffer, R.J., Taylor, K.E., 2016. Overview of the coupled Model Intercomparison Project phase 6 (CMIP6) experimental design and organization. Geosci. Model Dev. 9 (5), 1937–1958. https://doi.org/10.5194/gmd-9-1937-2016.

Feingold, G., Ghate, V.P., Russell, L.M., Blossey, P., Cantrell, W., Christensen, M.W., Diamond, M.S., Gettelman, A., Glassmeier, F., Gryspeerdt, E., 2024. Physical science research needed to evaluate the viability and risks of marine cloud brightening. Sci. Adv. 10 (12), eadi8594. https://doi.org/10.1126/sciadv.adi8594.

Feng, J., Chan, E., Vet, R., 2020. Air quality in the eastern United States and Eastern Canada for 1990–2015: 25 years of change in response to emission reductions of SO 2 and NO x in the region. Atmos. Chem. Phys. 20 (5), 3107–3134. https://doi.org/10.5194/acp-20-3107-2020.

Forster, P., Storelvmo, T., Armour, K., Collins, W., Dufresne, J.-L., Frame, D., Lunt, D., Mauritsen, T., Palmer, M., Watanabe, M., 2021. The Earth's Energy Budget, Climate Feedbacks, and Climate Sensitivity.

Frierson, D.M., Hwang, Y.-T., Fučkar, N.S., Seager, R., Kang, S.M., Donohoe, A., Maroon, E.A., Liu, X., Battisti, D.S., 2013. Contribution of ocean overturning circulation to tropical rainfall peak in the Northern Hemisphere. Nat. Geosci. 6 (11), 940–944. https://doi.org/10.1038/NGEO1987.

Fu, Q., Cribb, M., Barker, H., Krueger, S., Grossman, A., 2000. Cloud geometry effects on atmospheric solar absorption. J. Atmos. Sci. 57 (8), 1156–1168. https://doi.org/10.1175/1520-0469(2000)057<1156:CGEOAS>2.0.CO;2.

Garreaud, R., Muñoz, R., 2004. The diurnal cycle in circulation and cloudiness over the subtropical Southeast Pacific: a modeling study. J. Clim. 17 (8), 1699–1710. https://doi.org/10.1175/1520-0442(2004)017,1699:TDCICA.2.0.CO;2.

Ghatak, D., Miller, J., 2013. Implications for Arctic amplification of changes in the strength of the water vapor feedback. J. Geophys. Res. Atmos. 118 (14), 7569–7578. https://doi.org/10.1002/jgrd.50578.

Gimeno, L., Sorí, R., Vazquez, M., Stojanovic, M., Algarra, I., Eiras-Barca, J., Gimeno-Sotelo, L., Nieto, R., 2022. Extreme precipitation events. Wiley Interdiscip. Rev. Water 9 (6), e1611. https://doi.org/10.1002/wat2.1611.

Goessling, H.F., Rackow, T., Jung, T., 2024. Recent global temperature surge intensified by record-low planetary albedo. Science eadq7280. https://doi.org/10.1126/science.adq7280.

Grassl, H., Newiger, M., 1982. Changes of local planetary albedo by aerosol particles. Stud. Environ. Sci. Elsevier 313–320. https://doi.org/10.1016/S0166-1116(08)71018-5.

Grise, K.M., Polvani, L.M., 2014. Southern Hemisphere cloud–dynamics biases in CMIP5 models and their implications for climate projections. J. Clim. 27 (15), 6074–6092. https://doi.org/10.1175/JCLI-D-14-00113.1.

Gristey, J.J., Chiu, J.C., Gurney, R.J., Morcrette, C.J., Hill, P.G., Russell, J.E., Brindley, H. E., 2018. Insights into the diurnal cycle of global Earth outgoing radiation using a numerical weather prediction model. Atmos. Chem. Phys. 18 (7), 5129–5145. https://doi.org/10.5194/acp-18-5129-2018.

Gryspeerdt, E., Smith, T.W., O'Keeffe, E., Christensen, M.W., Goldsworth, F.W., 2019. The impact of ship emission controls recorded by cloud properties. Geophys. Res. Lett. 46 (21), 12547–12555. https://doi.org/10.1029/2019GL084700.

Gui, K., Che, H., Zheng, Y., Wang, Y., Zhang, L., Zhao, H., Li, L., Zhong, J., Yao, W., Zhang, X., 2021a. Seasonal variability and trends in global type-segregated aerosol optical depth as revealed by MISR satellite observations. Sci. Total Environ. 787, 147543. https://doi.org/10.1016/j.scitotenv.2021.147543.

Gui, K., Che, H., Zheng, Y., Zhao, H., Yao, W., Li, L., Zhang, L., Wang, H., Wang, Y., Zhang, X., 2021b. Three-dimensional climatology, trends, and meteorological drivers of global and regional tropospheric type-dependent aerosols: insights from 13 years (2007–2019) of CALIOP observations. Atmos. Chem. Phys. 21 (19), 15309–15336. https://doi.org/10.5194/acp-21-15309-2021.

Gupta, G., Ratnam, M.V., Madhavan, B., Narayanamurthy, C., 2022. Long-term trends in Aerosol Optical Depth obtained across the globe using multi-satellite measurements. Atmos. Environ. 273, 118953. https://doi.org/10.1016/j.atmosenv.2022.118953.

Hadas, O., Datseris, G., Blanco, J., Bony, S., Caballero, R., Stevens, B., Kaspi, Y., 2023. The role of baroclinic activity in controlling Earth's albedo in the present and future climates. Proc. Natl. Acad. Sci. 120 (5), e2208778120. https://doi.org/10.1073/pnas.2208778120.

Hall, A., Cox, P., Huntingford, C., Klein, S., 2019. Progressing emergent constraints on future climate change. Nat. Clim. Chang. 9 (4), 269–278. https://doi.org/10.1038/s41558-019-0436-6.

Han, J., Nie, J., Hu, Y., Boos, W.R., Liu, Y., Yang, J., Yuan, S., Li, X., Guo, J., Lan, J., 2023. Continental drift shifts tropical rainfall by altering radiation and ocean heat transport. Sci. Adv. 9 (10), eadf7209. https://doi.org/10.1126/sciadv.adf7209.

Hanna, E., 2007. Radiative forcing of climate change: expanding the concept and addressing uncertainties. By the National Research Council (NRC). National Academies Press, Washington DC, USA, 2005. 207 pp. Paperback Weather. 62 (4), 109–119. https://rmets.onlinelibrary.wiley.com/doi/10.1002/wea.8.

Hansen, J., Nazarenko, L., Ruedy, R., Sato, M., Willis, J., Del Genio, A., Koch, D., Lacis, A., Lo, K., Menon, S., 2005. Earth's energy imbalance: Confirmation and implications. Science 308 (5727), 1431–1435. https://doi.org/10.1126/science.1110252.

Hartmann, D.L., Doelling, D., 1991. On the net radiative effectiveness of clouds. J. Geophys. Res. Atmos. 96 (D1), 869–891. https://doi.org/10.1029/90JD02065.

Hartmann, D.L., Tank, A.M.K., Rusticucci, M., Alexander, L.V., Brönnimann, S., Charabi, Y.A.R., Dentener, F.J., Dlugokencky, E.J., Easterling, D.R., Kaplan, A., 2013. Observations: atmosphere and surface, climate change 2013 the physical science basis: Working group I contribution to the fifth assessment report of the intergovernmental panel on climate change. Cambridge University Press, pp. 159–254.

He, M., Hu, Y., Chen, N., Wang, D., Huang, J., Stamnes, K., 2019. High cloud coverage over melted areas dominates the impact of clouds on the albedo feedback in the Arctic. Sci. Rep. 9 (1), 9529. https://doi.org/10.1038/s41598-019-44155-w.

He, Y., Yang, K., Wild, M., Wang, K., Tong, D., Shao, C., Zhou, T., 2023. Constrained future brightening of solar radiation and its implication for China's solar power. Natl. Sci. Rev. 10 (1), nwac242. https://doi.org/10.1093/nsr/nwac242.

Helama, S., Arppe, L., Timonen, M., Mielikäinen, K., Oinonen, M., 2018. A 7.5 ka chronology of stable carbon isotopes from tree rings with implications for their use in palaeo-cloud reconstruction. Glob. Planet. Chang. 170, 20–33. https://doi.org/10.1016/j.gloplacha.2018.08.002.

Held, I.M., Soden, B.J., 2000. Water vapor feedback and global warming. Annu. Rev. Energy Environ. 25 (1), 441–475. https://doi.org/10.1146/annurev.energy.25.1.441.

Hinkelman, L.M., 2019. The global radiative energy budget in MERRA and MERRA-2: Evaluation with respect to CERES EBAF data. J. Clim. 32 (6), 1973–1994. https://doi.org/10.1175/JCLI-D-18-0445.1.

Hirsch, E., Koren, I., 2021. Record-breaking aerosol levels explained by smoke injection into the stratosphere. Science 371 (6535), 1269–1274. https://doi.org/10.1126/science.abe1415.

Hobbs, W.R., Roach, C., Roy, T., Sallée, J.-B., Bindoff, N., 2021. Anthropogenic temperature and salinity changes in the Southern Ocean. J. Clim. 34 (1), 215–228. https://doi.org/10.1175/JCLI-D-20-0454.1.

Hodnebrog, Ø., Myhre, G., Jouan, C., Andrews, T., Forster, P.M., Jia, H., Loeb, N.G., Olivié, D.J., Paynter, D., Quaas, J., 2024. Recent reductions in aerosol emissions have increased Earth's energy imbalance. Commun. Earth Environ. 5 (1), 166. https://doi.org/10.1038/s43247-024-01324-8.

Hofer, S., Tedstone, A.J., Fettweis, X., Bamber, J.L., 2017. Decreasing cloud cover drives the recent mass loss on the Greenland Ice Sheet. Sci. Adv. 3 (6), e1700584. https://doi.org/10.1126/sciadv.1700584.

Holbourn, A., Kuhnt, W., Regenberg, M., Schulz, M., Mix, A., Andersen, N., 2010. Does Antarctic glaciation force migration of the tropical rain belt? Geology 38 (9), 783–786. https://doi.org/10.1130/G31043.1.

Hong, G., Heygster, G., Rodriguez, C.A.M., 2006. Effect of cirrus clouds on the diurnal cycle of tropical deep convective clouds. J. Geophys. Res. Atmos. 111 (D6). https://doi.org/10.1029/2005JD006208.

Hong, C., Zhang, Q., Zhang, Y., Davis, S.J., Tong, D., Zheng, Y., Liu, Z., Guan, D., He, K., Schellnhuber, H.J., 2019. Impacts of climate change on future air quality and human health in China. Proc. Natl. Acad. Sci. 116 (35), 17193–17200. https://doi.org/10.1073/pnas.1812881116.

Horton, R.M., Mankin, J.S., Lesk, C., Coffel, E., Raymond, C., 2016. A review of recent advances in research on extreme heat events. Curr. Clim. Chang. Rep. 2, 242–259. https://doi.org/10.1007/s40641-016-0042-x.

Hotaling, S., Lutz, S., Dial, R.J., Anesio, A.M., Benning, L.G., Fountain, A.G., Kelley, J.L., McCutcheon, J., Skiles, S.M., Takeuchi, N., 2021. Biological albedo reduction on ice sheets, glaciers, and snowfields. Earth Sci. Rev. 220, 103728. https://doi.org/10.1016/j.earscirev.2021.103728.

House, F.B., Gruber, A., Hunt, G.E., Mecherikunnel, A.T., 1986. History of satellite missions and measurements of the Earth radiation budget (1957–1984). Rev. Geophys. 24 (2), 357–377. https://doi.org/10.1029/RG024i002p00357.

Hu, Y., Stamnes, K., 1993. An accurate parameterization of the radiative properties of water clouds suitable for use in climate models. J. Clim. 6 (4), 728–742. https://doi.org/10.1175/1520-0442(1993)006<0728:AAPOTR>2.0.CO;2.

Hu, Y., Rodier, S., Xu, K.M., Sun, W., Huang, J., Lin, B., Zhai, P., Josset, D., 2010. Occurrence, liquid water content, and fraction of supercooled water clouds from combined CALIOP/IIR/MODIS measurements. J. Geophys. Res. Atmos. 115 (D4). https://doi.org/10.1029/2009JD012384.

Hu, Y., Jia, G., Pohl, C., Zhang, X., van Genderen, J., 2016. Assessing surface albedo change and its induced radiation budget under rapid urbanization with Landsat and GLASS data. Theor. Appl. Clim. 123, 711–722. https://doi.org/10.1007/s00704-015-1385-2.

Hu, Z., Chen, D., Chen, X., Zhou, Q., Peng, Y., Li, J., Sang, Y., 2022. CCHZ-DISO: a timely new assessment system for data quality or model performance from Da Dao Zhi Jian. Geophys. Res. Lett. 49 (23), e2022GL100681. https://doi.org/10.1029/2022GL100681.

Hu, Z.-Z., McPhaden, M.J., Huang, B., Zhu, J., Liu, Y., 2024. Accelerated warming in the North Pacific since 2013. Nat. Clim. Chang. 14 (9), 929–931. https://doi.org/10.1038/s41558-024-02088-x.

Huang, B., Yin, X., Carton, J.A., Chen, L., Graham, G., Hogan, P., Smith, T., Zhang, H.M., 2024. Record high sea surface temperatures in 2023. Geophys. Res. Lett. 51 (14), e2024GL108369. https://doi.org/10.1029/2024GL108369.

Hunt, G.E., Kandel, R., Mecherikunnel, A.T., 1986. A history of presatellite investigations of the earth's radiation budget. Rev. Geophys. 24 (2), 351–356. https://doi.org/10.1029/RG024i002p00351.

Hwang, Y.-T., Frierson, D.M., 2013. Link between the double-Intertropical Convergence Zone problem and cloud biases over the Southern Ocean. Proc. Natl. Acad. Sci. 110 (13), 4935–4940. https://doi.org/10.1073/pnas.1213302110.

IPCC, A, 2013. Climate change 2013: the physical science basis. In: Contribution of working group I to the fifth assessment report of the intergovernmental panel on climate change, 1535.

IPCC, A, 2021. Climate change 2021: the physical science basis. In: Masson-Delmotte, V., Zhai, P., Pirani, A., Connors, S.L., Péan, C., Berger, S., Caud, N., Chen, Y., Goldfarb, L., Gomis, M.I., Huang, M., Leitzell, K., Lonnoy, E., Matthews, J.B.R., Maycock, T.K., Waterfield, T., Yelekçi, O., Yu, R., Zhou, B. (Eds.), Contribution of Working Group I to the Sixth Assessment Report of the Intergovernmental Panel on climate Change, p. 2391. https://doi.org/10.1017/9781009157896, 2(1).

Jenkins, M., Dai, A., 2021. The impact of Sea-Ice loss on Arctic climate feedbacks and their role for Arctic Amplification. Geophys. Res. Lett. 48 (15), e2021GL094599. https://doi.org/10.1029/2021GL094599.

Jian, B., Li, J., Wang, G., He, Y., Han, Y., Zhang, M., Huang, J., 2018. The Impacts of Atmospheric and Surface Parameters on Long-Term Variations in the Planetary Albedo. J. Clim. 31 (21), 8705–8718. https://doi.org/10.1175/jcli-d-17-0848.1.

Jian, B., Li, J., Zhao, Y., He, Y., Wang, J., Huang, J., 2020. Evaluation of the CMIP6 planetary albedo climatology using satellite observations. Clim. Dyn. 54 (11−12), 5145–5161. https://doi.org/10.1007/s00382-020-05277-4.

Jiao, T., Williams, C.A., Ghimire, B., Masek, J., Gao, F., Schaaf, C., 2017. Global climate forcing from albedo change caused by large-scale deforestation and reforestation: quantification and attribution of geographic variation. Clim. Chang. 142, 463–476. https://doi.org/10.1007/s10584-017-1962-8.

Jiao, P., Wang, J., Chen, X., Ruan, J., Ye, X., Alavi, A.H., 2021. Next-generation remote sensing and prediction of sand and dust storms: State-of-the-art and future trends. Int. J. Remote Sens. 42 (14), 5277–5316. https://doi.org/10.1080/01431161.2021.1912433.

Jin, Q., Grandey, B.S., Rothenberg, D., Avramov, A., Wang, C., 2018. Impacts on cloud radiative effects induced by coexisting aerosols converted from international shipping and maritime DMS emissions. Atmos. Chem. Phys. 18 (22), 16793–16808. https://doi.org/10.5194/acp-18-16793-2018.

Jones, A., Haywood, J., Boucher, O., Kravitz, B., Robock, A., 2010. Geoengineering by stratospheric SO 2 injection: results from the Met Office HadGEM2 climate model and comparison with the Goddard Institute for Space Studies ModelE. Atmos. Chem. Phys. 10 (13), 5999–6006. https://doi.org/10.5194/acp-10-5999-2010.

Jönsson, A., Bender, F.A.-M., 2022. Persistence and variability of Earth's interhemispheric albedo symmetry in 19 years of CERES EBAF observations. J. Clim. 35 (1), 249–268. https://doi.org/10.1175/JCLI-D-20-0970.1.

Jönsson, A.R., Bender, F.A.-M., 2023. The implications of maintaining Earth's hemispheric albedo symmetry for shortwave radiative feedbacks. Earth Syst. Dynam. 14 (2), 345–365. https://doi.org/10.5194/esd-14-345-2023.

Kahn, R.A., Gaitley, B.J., 2015. An analysis of global aerosol type as retrieved by MISR. J. Geophys. Res. Atmos. 120 (9), 4248–4281. https://doi.org/10.1002/2015JD023322.

Kang, S.M., Held, I.M., Frierson, D.M., Zhao, M., 2008. The response of the ITCZ to extratropical thermal forcing: Idealized slab-ocean experiments with a GCM. J. Clim. 21 (14), 3521–3532. https://doi.org/10.1175/2007JCLI2146.1.

Kashiwase, H., Ohshima, K.I., Nihashi, S., Eicken, H., 2017. Evidence for ice-ocean albedo feedback in the Arctic Ocean shifting to a seasonal ice zone. Sci. Rep. 7 (1), 8170. https://doi.org/10.1038/s41598-017-08467-z.

Kato, S., 2009. Interannual variability of the global radiation budget. J. Clim. 22 (18), 4893–4907. https://doi.org/10.1175/2009JCLI2795.1.

Kato, S., Loeb, N.G., Minnis, P., Francis, J.A., Charlock, T.P., Rutan, D.A., Clothiaux, E.E., Sun-Mack, S., 2006. Seasonal and interannual variations of top-of-atmosphere irradiance and cloud cover over polar regions derived from the CERES data set. Geophys. Res. Lett. 33 (19). https://doi.org/10.1029/2006GL026685.

Kato, S., Rose, F.G., Rutan, D.A., Thorsen, T.J., Loeb, N.G., Doelling, D.R., Huang, X., Smith, W.L., Su, W., Ham, S.-H., 2018. Surface irradiances of edition 4.0 clouds and the earth's radiant energy system (CERES) energy balanced and filled (EBAF) data product. J. Clim. 31 (11), 4501–4527. https://doi.org/10.1175/JCLI-D-17-0523.1.

Kellogg, W.W., 1975. Climatic feedback mechanisms involving the polar regions. Clim. Arctic. 111, 116.

Kilbourne, K.H., Wanamaker, A.D., Moffa-Sanchez, P., Reynolds, D.J., Amrhein, D.E., Butler, P.G., Gebbie, G., Goes, M., Jansen, M.F., Little, C.M., 2022. Atlantic circulation change still uncertain. Nat. Geosci. 15 (3), 165–167. https://doi.org/10.1038/s41561-022-00896-4.

Klein, S.A., Hartmann, D.L., Norris, J.R., 1995. On the relationships among low-cloud structure, sea surface temperature, and atmospheric circulation in the summertime Northeast Pacific. J. Clim. 8 (5), 1140–1155. https://doi.org/10.1175/1520-0442(1995)008%3C1140:OTRALC%3E2.0.CO;2.

Kopp, G., 2016. Magnitudes and timescales of total solar irradiance variability. J. Space Weather Space Clim. 6, A30. https://doi.org/10.1051/swsc/2016025.

Kravitz, B., Caldeira, K., Boucher, O., Robock, A., Rasch, P.J., Alterskjaer, K., Karam, D. B., Cole, J.N., Curry, C.L., Haywood, J.M., 2013. Climate model response from the geoengineering model intercomparison project (GeoMIP). J. Geophys. Res. Atmos. 118 (15), 8320–8332. https://doi.org/10.1002/jgrd.50646.

Krishna Moorthy, K., Suresh Babu, S., Manoj, M., Satheesh, S., 2013. Buildup of aerosols over the Indian Region. Geophys. Res. Lett. 40 (5), 1011–1014. https://doi.org/10.1002/grl.50165.

Kuhlbrodt, T., Swaminathan, R., Ceppi, P., Wilder, T., 2024. A glimpse into the future: the 2023 ocean temperature and sea ice extremes in the context of longer-term climate change. Bull. Am. Meteorol. Soc. 105 (3), E474–E485. https://doi.org/10.1175/BAMS-D-23-0209.1.

Kuma, P., McDonald, A.J., Morgenstern, O., Alexander, S.P., Cassano, J.J., Garrett, S., Halla, J., Hartery, S., Harvey, M.J., Parsons, S., 2020. Evaluation of Southern Ocean cloud in the HadGEM3 general circulation model and MERRA-2 reanalysis using ship-based observations. Atmos. Chem. Phys. 20 (11), 6607–6630. https://doi.org/10.5194/acp-20-6607-2020.

Kuniyal, J.C., Guleria, R.P., 2019. The current state of aerosol-radiation interactions: a mini review. J. Aerosol Sci. 130, 45–54. https://doi.org/10.1016/j.jaerosci.2018.12.010.

Kurita, N., 2011. Origin of Arctic water vapor during the ice-growth season. Geophys. Res. Lett. 38 (2). https://doi.org/10.1029/2010GL046064.

Lachlan-Cope, T., 2010. Antarctic clouds. Polar Res. 29 (2), 150–158. https://doi.org/10.1111/j.1751-8369.2010.00148.x.

Lambeck, K., 2004. Sea-level change through the last glacial cycle: geophysical, glaciological and palaeogeographic consequences. Comptes rendus. Géosci. 336 (7–8), 677–689. https://doi.org/10.1016/j.crte.2003.12.017.

Lauer, A., Hamilton, K., 2013. Simulating clouds with global climate models: a comparison of CMIP5 results with CMIP3 and satellite data. J. Clim. 26 (11), 3823–3845. https://doi.org/10.1175/JCLI-D-12-00451.1.

Lawson, R.P., Gettelman, A., 2014. Impact of Antarctic mixed-phase clouds on climate. Proc. Natl. Acad. Sci. 111 (51), 18156–18161. https://doi.org/10.1073/pnas.1418197111.

Lea, D.W., Pak, D.K., Peterson, L.C., Hughen, K.A., 2003. Synchroneity of tropical and high-latitude Atlantic temperatures over the last glacial termination. Science 301 (5638), 1361–1364. https://doi.org/10.1126/science.1088470.

Letu, H., Nagao, T.M., Nakajima, T.Y., Riedi, J., Ishimoto, H., Baran, A.J., Shang, H., Sekiguchi, M., Kikuchi, M., 2018. Ice cloud properties from Himawari-8/AHI next-generation geostationary satellite: Capability of the AHI to monitor the DC cloud generation process. IEEE Trans. Geosci. Remote Sens. 57 (6), 3229–3239. https://doi.org/10.1109/TGRS.2018.2882803.

Li, J., Huang, J., Stamnes, K., Wang, T., Lv, Q., Jin, H., 2015. A global survey of cloud overlap based on CALIPSO and CloudSat measurements. Atmos. Chem. Phys. 15 (1), 519–536. https://doi.org/10.5194/acp-15-519-2015.

Li, Y., Wang, T., Zeng, Z., Peng, S., Lian, X., Piao, S., 2016. Evaluating biases in simulated land surface albedo from CMIP5 global climate models. J. Geophys. Res. Atmos. 121 (11), 6178–6190. https://doi.org/10.1002/2016JD024774.

Li, J., Lv, Q., Zhang, M., Wang, T., Kawamoto, K., Chen, S., Zhang, B., 2017. Effects of atmospheric dynamics and aerosols on the fraction of supercooled water clouds. Atmos. Chem. Phys. 17 (3), 1847–1863. https://doi.org/10.5194/acp-17-1847-2017.

Li, J., Lv, Q., Jian, B., Zhang, M., Zhao, C., Fu, Q., Kawamoto, K., Zhang, H., 2018a. The impact of atmospheric stability and wind shear on vertical cloud overlap over the Tibetan Plateau. Atmos. Chem. Phys. 18 (10), 7329–7343. https://doi.org/10.5194/acp-18-7329-2018.

Li, Q., Ma, M., Wu, X., Yang, H., 2018b. Snow cover and vegetation-induced decrease in global Albedo from 2002 to 2016. J. Geophys. Res. Atmos. 123 (1), 124–138. https://doi.org/10.1002/2017jd027010.

Li, R., Mei, X., Chen, L., Wang, L., Wang, Z., Jing, Y., 2020. Long-term (2005–2017) view of atmospheric pollutants in Central China using multiple satellite observations. Remote Sens 12 (6), 1041. https://doi.org/10.3390/rs12061041.

Li, M., Shen, F., Sun, X., 2021. 2019–2020 Australian bushfire air particulate pollution and impact on the South Pacific Ocean. Sci. Rep. 11 (1), 12288. https://doi.org/10.1038/s41598-021-91547-y.

Li, R., Jian, B., Li, J., Wen, D., Zhang, L., Wang, Y., Wang, Y., 2024. Understanding the trends in reflected solar radiation: a latitude-and month-based perspective. Atmos. Chem. Phys. 24 (17), 9777–9803. https://doi.org/10.5194/acp-24-9777-2024.

Liang, S., Wang, D., He, T., Yu, Y., 2019. Remote sensing of earth's energy budget: Synthesis and review. Int. J. Digital Earth. 12 (7), 737–780. https://doi.org/10.1080/17538947.2019.1597189.

Lin, J.-L., 2007. The double-ITCZ problem in IPCC AR4 coupled GCMs: Ocean–atmosphere feedback analysis. J. Clim. 20 (18), 4497–4525. https://doi.org/10.1175/JCLI4272.1.

Liou, K.-N., 1976. On the absorption, reflection and transmission of solar radiation in cloudy atmospheres. J. Atmos. Sci. 33 (5), 798–805. https://doi.org/10.1175/1520-0469(1976)033%3C0798:OTARAT%3E2.0.CO;2.

Liu, W., Fedorov, A.V., Xie, S.-P., Hu, S., 2020. Climate impacts of a weakened Atlantic Meridional Overturning Circulation in a warming climate. Sci. Adv. 6 (26), eaaz4876 doi:10.1126%2Fsciadv.aaz4876.

Loeb, N.G., Priestley, K.J., Kratz, D.P., Geier, E.B., Green, R.N., Wielicki, B.A., Hinton, P. O.R., Nolan, S.K., 2001. Determination of unfiltered radiances from the Clouds and the Earth's Radiant Energy System instrument. J. Appl. Meteorol. 40 (4), 822–835. https://doi.org/10.1175/1520-0450(2001)040<0822:DOURFT>2.0.CO;2.

Loeb, N.G., Manalo-Smith, N., Kato, S., Miller, W.F., Gupta, S.K., Minnis, P., Wielicki, B. A., 2003. Angular distribution models for top-of-atmosphere radiative flux estimation from the Clouds and the Earth's Radiant Energy System instrument on the Tropical Rainfall measuring Mission satellite. Part I: Methodology. J. Appl. Meteorol. Climatol. 42 (2), 240–265. https://doi.org/10.1175/1520-0450(2003)042<0240:ADMFTO>2.0.CO;2.

Loeb, N.G., Wielicki, B.A., Rose, F.G., Doelling, D.R., 2007. Variability in global top-of-atmosphere shortwave radiation between 2000 and 2005. Geophys. Res. Lett. 34 (3), L03704. https://doi.org/10.1029/2006GL028196.

Loeb, N.G., Wielicki, B.A., Doelling, D.R., Smith, G.L., Keyes, D.F., Kato, S., Manalo-Smith, N., Wong, T., 2009. Toward optimal closure of the Earth's top-of-atmosphere radiation budget. J. Clim. 22 (3), 748–766. https://doi.org/10.1175/2008JCLI2637.1.

Loeb, N.G., Doelling, D.R., Wang, H., Su, W., Nguyen, C., Corbett, J.G., Liang, L., Mitrescu, C., Rose, F.G., Kato, S., 2018a. Clouds and the earth's radiant energy system (CERES). energy balanced and filled (EBAF) top-of-atmosphere (TOA) edition-4.0 data product J. Clim. 31 (2), 895–918. https://doi.org/10.1175/JCLI-D-17-0208.1.

Loeb, N.G., Thorsen, T.J., Norris, J.R., Wang, H., Su, W., 2018b. Changes in Earth's energy budget during and after the "pause" in global warming: An observational perspective. Climate 6 (3), 62. https://doi.org/10.3390/cli6030062.

Loeb, N.G., Wang, H., Rose, F.G., Kato, S., Smith, W.L., Sun-Mack, S., 2019. Decomposing shortwave top-of-atmosphere and surface radiative flux variations in terms of surface and atmospheric contributions. J. Clim. 32 (16), 5003–5019. https://doi.org/10.1175/JCLI-D-18-0826.1.

Loeb, N.G., Rose, F.G., Kato, S., Rutan, D.A., Su, W., Wang, H., Doelling, D.R., Smith, W. L., Gettelman, A., 2020a. Toward a consistent definition between satellite and model clear-sky radiative fluxes. J. Clim. 33 (1), 61–75. https://doi.org/10.1175/JCLI-D-19-0381.1.

Loeb, N.G., Wang, H., Allan, R.P., Andrews, T., Armour, K., Cole, J.N., Dufresne, J.L., Forster, P., Gettelman, A., Guo, H., 2020b. New generation of climate models track recent unprecedented changes in Earth's radiation budget observed by CERES. Geophys. Res. Lett. 47 (5), e2019GL086705. https://doi.org/10.1029/2019GL086705.

Loeb, N.G., Johnson, G.C., Thorsen, T.J., Lyman, J.M., Rose, F.G., Kato, S., 2021a. Satellite and ocean data reveal marked increase in Earth's heating rate. Geophys. Res. Lett. 48 (13), e2021GL093047. https://doi.org/10.1029/2021GL093047.

Loeb, N.G., Su, W., Bellouin, N., Ming, Y., 2021b. Changes in clear-sky shortwave aerosol direct radiative effects since 2002. J. Geophys. Res. Atmos. 126 (5), e2020JD034090. https://doi.org/10.1029/2020JD034090.

Loeb, N.G., Mayer, M., Kato, S., Fasullo, J.T., Zuo, H., Senan, R., Lyman, J.M., Johnson, G.C., Balmaseda, M., 2022. Evaluating twenty-year trends in Earth's energy flows from observations and reanalyses. J. Geophys. Res. Atmos. 127 (12), e2022JD036686. https://doi.org/10.1029/2022JD036686.

Loeb, N.G., Ham, S.-H., Allan, R.P., Thorsen, T.J., Meyssignac, B., Kato, S., Johnson, G.C., Lyman, J.M., 2024. Observational assessment of changes in earth's energy imbalance since 2000. Surv. Geophys. 1–27. https://doi.org/10.1007/s10712-024-09838-8.

Lu, Y., Khalil, M., 1996. The distribution of solar radiation in the earth's atmosphere: the effects of ozone, aerosols and clouds. Chemosphere 32 (4), 739–758. https://doi.org/10.1016/0045-6535(96)00028-8.

Luber, G., McGeehin, M., 2008. Climate change and extreme heat events. Am. J. Prev. Med. 35 (5), 429–435. https://doi.org/10.1016/j.amepre.2008.08.021.

Luo, H., Quaas, J., Han, Y., 2023. Examining cloud vertical structure and radiative effects from satellite retrievals and evaluation of CMIP6 scenarios. Atmos. Chem. Phys. 23 (14), 8169–8186. https://doi.org/10.5194/acp-23-8169-2023.

Lv, M., Song, Y., Li, X., Wang, M., Qu, Y., 2022. Spatiotemporal characteristics and driving factors of global planetary albedo: an analysis using the Geodetector method. Theor. Appl. Clim, 1–16. https://doi.org/10.1007/s00704-021-03858-9.

Mahowald, N.M., Li, L., Albani, S., Hamilton, D.S., Kok, J.F., 2024. Opinion: the importance of historical and paleoclimate aerosol radiative effects. Atmos. Chem. Phys. 24 (1), 533–551. https://doi.org/10.5194/acp-24-533-2024.

Mamalakis, A., Randerson, J.T., Yu, J.-Y., Pritchard, M.S., Magnusdottir, G., Smyth, P., Levine, P.A., Yu, S., Foufoula-Georgiou, E., 2021. Zonally contrasting shifts of the tropical rain belt in response to climate change. Nat. Clim. Chang. 11 (2), 143–151. https://doi.org/10.1038/s41558-020-00963-x.

Marshall, J., Donohoe, A., Ferreira, D., McGee, D., 2014. The ocean's role in setting the mean position of the Inter-Tropical Convergence Zone. Clim. Dyn. 42, 1967–1979. https://doi.org/10.1007/s00382-013-1767-z.

McCormick, R.A., Ludwig, J.H., 1967. Climate modification by atmospheric aerosols. Science 156 (3780), 1358–1359. https://doi.org/10.1126/science.156.3780.1358.

McCormick, M.P., Thomason, L.W., Trepte, C.R., 1995. Atmospheric effects of the Mt Pinatubo eruption. Nature 373 (6513), 399–404. https://doi.org/10.1038/373399a0.

McCoy, D.T., Burrows, S.M., Wood, R., Grosvenor, D.P., Elliott, S.M., Ma, P.-L., Rasch, P. J., Hartmann, D.L., 2015. Natural aerosols explain seasonal and spatial patterns of Southern Ocean cloud albedo. Sci. Adv. 1 (6), e1500157. https://doi.org/10.1126/sciadv.1500157.

McDonald, J.E., 1960. Direct absorption of solar radiation by atmospheric water vapor. J. Atmos. Sci. 17 (3), 319–328. https://doi.org/10.1175/1520-0469(1960)017<0319:DAOSRB>2.0.CO;2.

Menon, S., Akbari, H., Mahanama, S., Sednev, I., Levinson, R., 2010. Radiative forcing and temperature response to changes in urban albedos and associated CO2 offsets. Environ. Res. Lett. 5 (1), 014005. https://doi.org/10.1088/1748-9326/5/1/014005.

Mercer, A.M., Keith, D.W., Sharp, J.D., 2011. Public understanding of solar radiation management. Environ. Res. Lett. 6 (4), 044006. https://doi.org/10.1088/1748-9326/6/4/044006.

Miinalainen, T., Kokkola, H., Lehtinen, K.E., Kühn, T., 2021. Comparing the radiative forcings of the anthropogenic aerosol emissions from Chile and Mexico. J. Geophys. Res. Atmos. 126 (10), e2020JD033364. https://doi.org/10.1080/16000889.2020.1821512.

Millan, L., Santee, M.L., Lambert, A., Livesey, N.J., Werner, F., Schwartz, M.J., Pumphrey, H.C., Manney, G.L., Wang, Y., Su, H., 2022. The Hunga Tonga-Hunga Ha'apai hydration of the stratosphere. Geophys. Res. Lett. 49 (13), e2022GL099381. https://doi.org/10.1029/2022GL099381.

Minnis, P., Trepte, Q.Z., Sun-Mack, S., Chen, Y., Doelling, D.R., Young, D.F., Spangenberg, D.A., Miller, W.F., Wielicki, B.A., Brown, R.R., 2008. Cloud detection in nonpolar regions for CERES using TRMM VIRS and Terra and Aqua MODIS data. IEEE Trans. Geosci. Remote Sens. 46 (11), 3857–3884. https://doi.org/10.1029/2011JD016422.

Myhre, G., Myhre, A., 2003. Uncertainties in radiative forcing due to surface albedo changes caused by land-use changes. J. Clim. 16 (10), 1511–1524. https://doi.org/10.1175/1520-0442-16.10.1511.

Nikolov, N., Zeller, K.F., 2024. Roles of Earth's Albedo Variations and Top-of-the-Atmosphere Energy Imbalance in recent Warming: New Insights from Satellite and Surface Observations. Geomatics 4 (3), 311–341. https://doi.org/10.3390/geomatics4030017.

Noël, B., Van De Berg, W., Van Meijgaard, E., Kuipers Munneke, P., Van De Wal, R., Van Den Broeke, M., 2015. Evaluation of the updated regional climate model RACMO2. 3: summer snowfall impact on the Greenland Ice Sheet. Cryosphere 9 (5), 1831–1844. https://doi.org/10.5194/tc-9-1831-2015.

North, G.R., Cahalan, R.F., Coakley Jr., J.A., 1981. Energy balance climate models. Rev. Geophys. 19 (1), 91–121. https://doi.org/10.1029/RG019i001p00091.

Ouyang, Z., Sciusco, P., Jiao, T., Feron, S., Lei, C., Li, F., John, R., Fan, P., Li, X., Williams, C.A., 2022. Albedo changes caused by future urbanization contribute to global warming. Nat. Commun. 13 (1), 3800. https://doi.org/10.1038/s41467-022-31558-z.

Pahnke, K., Sachs, J.P., Keigwin, L., Timmermann, A., Xie, S.P., 2007. Eastern tropical Pacific hydrologic changes during the past 27,000 years from D/H ratios in alkenones. Paleoceanography 22 (4). https://doi.org/10.1029/2007PA001468.

Pan, X., Ichoku, C., Chin, M., Bian, H., Darmenov, A., Colarco, P., Ellison, L., Kucsera, T., da Silva, A., Wang, J., 2020. Six global biomass burning emission datasets: intercomparison and application in one global aerosol model. Atmos. Chem. Phys. 20 (2), 969–994. https://doi.org/10.5194/acp-20-969-2020.

Park, J.M., McComiskey, A.C., Painemal, D., Smith Jr., W.L., 2024. Long-term trends in aerosols, low clouds, and large-scale meteorology over the Western North Atlantic from 2003 to 2020. J. Geophys. Res. Atmos. 129 (11), e2023JD039592. https://doi.org/10.1029/2023JD039592.

Peng, Y., Lohmann, U., 2003. Sensitivity study of the spectral dispersion of the cloud droplet size distribution on the indirect aerosol effect. Geophys. Res. Lett. 30 (10). https://doi.org/10.1029/2003GL017192.

Peng, C., Zeng, J., Chen, K.-S., Li, Z., Ma, H., Zhang, X., Shi, P., Wang, T., Yi, L., Bi, H., 2023. Global spatiotemporal trend of satellite-based soil moisture and its influencing factors in the early 21st century. Remote Sens. Environ. 291, 113569. https://doi.org/10.1016/j.rse.2023.113569.

Perkins, S., 2019. Albedo is a simple concept that plays complicated roles in climate and astronomy. Proc. Natl. Acad. Sci. 116 (51), 25369–25371. https://doi.org/10.1073/pnas.1918770116.

Peterson, D.A., Fromm, M.D., McRae, R.H., Campbell, J.R., Hyer, E.J., Taha, G., Camacho, C.P., Kablick III, G.P., Schmidt, C.C., DeLand, M.T., 2021. Australia's Black Summer pyrocumulonimbus super outbreak reveals potential for increasingly extreme stratospheric smoke events. npj Clim. Atmos. Sci. 4 (1), 38. https://doi.org/10.1038/s41612-021-00192-9.

Picard, G., Domine, F., Krinner, G., Arnaud, L., Lefebvre, E., 2012. Inhibition of the positive snow-albedo feedback by precipitation in interior Antarctica. Nat. Clim. Chang. 2 (11), 795–798. https://doi.org/10.1038/nclimate1590.

Pincus, R., Baker, M.B., 1994. Effect of precipitation on the albedo susceptibility of clouds in the marine boundary layer. Nature 372 (6503), 250–252. https://doi.org/10.1038/372250a0.

Pinker, R., Grodsky, S., Zhang, B., Busalacchi, A., Chen, W., 2017. ENSO impact on surface radiative fluxes as observed from space. J. Geophys. Res.: Oceans. 122 (10), 7880–7896. https://doi.org/10.1002/2017JC012900.

Protat, A., Delanoë, J., Plana-Fattori, A., May, P., O'Connor, E., 2010. The statistical properties of tropical ice clouds generated by the West African and Australian monsoons, from ground-based radar–lidar observations. Q. J. R. Meteorol. Soc. 136 (S1), 345–363. https://doi.org/10.1002/qj.490.

Pu, W., Cui, J., Wu, D., Shi, T., Chen, Y., Xing, Y., Zhou, Y., Wang, X., 2021. Unprecedented snow darkening and melting in New Zealand due to 2019–2020 Australian wildfires. Fundam. Res. 1 (3), 224–231. https://doi.org/10.1016/j.fmre.2021.04.001.

Purich, A., Doddridge, E.W., 2023. Record low Antarctic Sea ice coverage indicates a new sea ice state. Commun. Earth Environ. 4 (1), 314. https://doi.org/10.1038/s43247-023-00961-9.

Qu, X., Hall, A., 2005. Surface contribution to planetary albedo variability in cryosphere regions. J. Clim. 18 (24), 5239–5252. https://doi.org/10.1175/JCLI3555.1.

Raghuraman, S.P., Paynter, D., Ramaswamy, V., 2021. Anthropogenic forcing and response yield observed positive trend in Earth's energy imbalance. Nat. Commun. 12 (1), 4577. https://doi.org/10.1038/s41467-021-24544-4.

Raghuraman, S.P., Soden, B., Clement, A., Vecchi, G., Menemenlis, S., Yang, W., 2024. The 2023 global warming spike was driven by the El Niño–Southern Oscillation. Atmos. Chem. Phys. 24 (19), 11275–11283. https://doi.org/10.5194/acp-24-11275-2024.

Rahmstorf, S., Box, J.E., Feulner, G., Mann, M.E., Robinson, A., Rutherford, S., Schaffernicht, E.J., 2015. Exceptional twentieth-century slowdown in Atlantic Ocean overturning circulation. Nat. Clim. Chang. 5 (5), 475–480 doi:10.1038%2Fnclimate2554.

Ramanathan, V., 1987. The role of earth radiation budget studies in climate and general circulation research. J. Geophys. Res. Atmos. 92 (D4), 4075–4095. https://doi.org/10.1029/JD092iD04p04075.

Ramanathan, V., Cess, R., Harrison, E., Minnis, P., Barkstrom, B., Ahmad, E., Hartmann, D., 1989. Cloud-radiative forcing and climate: results from the Earth Radiation Budget Experiment. Science 243 (4887), 57–63. https://doi.org/10.1126/science.243.4887.57.

Rantanen, M., Karpechko, A.Y., Lipponen, A., Nordling, K., Hyvärinen, O., Ruosteenoja, K., Vihma, T., Laaksonen, A., 2022. The Arctic has warmed nearly four times faster than the globe since 1979. Commun. Earth Environ. 3 (1), 168. https://doi.org/10.1038/s43247-022-00498-3.

Reddington, C.L., Morgan, W.T., Darbyshire, E., Brito, J., Coe, H., Artaxo, P., Scott, C.E., Marsham, J., Spracklen, D.V., 2019. Biomass burning aerosol over the Amazon: analysis of aircraft, surface and satellite observations using a global aerosol model. Atmos. Chem. Phys. 19 (14), 9125–9152. https://doi.org/10.5194/acp-19-9125-2019.

Reisen, F., Meyer, C.M., Keywood, M.D., 2013. Impact of biomass burning sources on seasonal aerosol air quality. Atmos. Environ. 67, 437–447. https://doi.org/10.1016/j.atmosenv.2012.11.004.

Riahi, K., Van Vuuren, D.P., Kriegler, E., Edmonds, J., O'neill, B.C., Fujimori, S., Bauer, N., Calvin, K., Dellink, R., Fricko, O., 2017. The Shared Socioeconomic Pathways and their energy, land use, and greenhouse gas emissions implications: An overview. Glob. Environ. Chang. 42, 153–168. https://doi.org/10.1016/j.gloenvcha.2016.05.009.

Ricaud, P., Durand, P., Grigioni, P., Del Guasta, M., Camporeale, G., Roy, A., Attié, J.-L., Bognar, J., 2024. In situ observations of supercooled liquid water clouds over Dome C, Antarctica, by balloon-borne sondes. Atmos. Meas. Tech. 17 (17), 5071–5089. https://doi.org/10.5194/amt-17-5071-2024.

Ricke, K.L., Morgan, M.G., Allen, M.R., 2010. Regional climate response to solar-radiation management. Nat. Geosci. 3 (8), 537–541. https://doi.org/10.1038/NGEO915.

Ridley, J., Blockley, E., Ringer, M., 2023. Arctic Sea Ice Causes Seasonal differences in the Response of Arctic Water Vapor to climate Warming in the CMIP6 Model, HadGEM3-GC3. 1. Geophys. Res. Lett. 50 (13), e2022GL102541. https://doi.org/10.1029/2022GL102541.

Ripple, W.J., Wolf, C., Gregg, J.W., Rockström, J., Newsome, T.M., Law, B.E., Marques, L., Lenton, T.M., Xu, C., Huq, S., 2023. The 2023 state of the climate report: Entering uncharted territory. Bioscience 73 (12), 841–850. https://doi.org/10.1093/biosci/biad080.
Roach, L.A., Meier, W.N., 2024. Sea ice in 2023. Nat. Rev. Earth Environ. 5 (4), 235–237. https://doi.org/10.1038/s43017-024-00542-0.
Robin, G.D.Q., 2010. The Climatic Record in Polar Ice Sheets. Cambridge University Press.
Robock, A., 2000. Volcanic eruptions and climate. Rev. Geophys. 38 (2), 191–219. https://doi.org/10.1029/1998RG000054.
Robock, A., Oman, L., Stenchikov, G.L., 2008. Regional climate responses to geoengineering with tropical and Arctic SO2 injections. J. Geophys. Res. Atmos. 113 (D16). https://doi.org/10.1029/2008JD010050.
Romano, M., Cifelli, R.L., 2015. 100 years of continental drift. Science 350 (6263), 915–916. https://doi.org/10.1126/science.aad6230.
Rozendaal, M.A., Leovy, C.B., Klein, S.A., 1995. An observational study of diurnal variations of marine stratiform cloud. J. Clim. 8 (7), 1795–1809. https://doi.org/10.1175/1520-0442(1995)008%3C1795:AOSODV%3E2.0.CO;2.
Rugenstein, M., Hakuba, M., 2023. Connecting hemispheric asymmetries of planetary albedo and surface temperature. Geophys. Res. Lett. 50 (6), e2022GL101802. https://doi.org/10.1029/2022GL101802.
Rutan, D.A., Smith, G.L., Wong, T., 2014. Diurnal variations of albedo retrieved from earth radiation budget experiment measurements. J. Appl. Meteorol. Climatol. 53 (12), 2747–2760. https://doi.org/10.1175/JAMC-D-13-0119.1.
Schmidt, G., 2024. Climate models can't explain 2023's huge heat anomaly — we could be in uncharted territory. Nature 627, 467. https://doi.org/10.1038/d41586-024-00816-z.
Schoeberl, M.R., Wang, Y., Ueyama, R., Dessler, A., Taha, G., Yu, W., 2023. The estimated climate impact of the Hunga Tonga-Hunga Ha'apai eruption plume. Geophys. Res. Lett. 50 (18), e2023GL104634. https://doi.org/10.1029/2023GL104634.
Screen, J.A., Simmonds, I., 2010. The central role of diminishing sea ice in recent Arctic temperature amplification. Nature 464 (7293), 1334–1337. https://doi.org/10.1038/nature09051.
Seinfeld, J.H., Bretherton, C., Carslaw, K.S., Coe, H., DeMott, P.J., Dunlea, E.J., Feingold, G., Ghan, S., Guenther, A.B., Kahn, R., 2016. Improving our fundamental understanding of the role of aerosol− cloud interactions in the climate system. Proc. Natl. Acad. Sci. 113 (21), 5781–5790. https://doi.org/10.1073/pnas.1514043113.
Serreze, M.C., Barrett, A.P., Stroeve, J., 2012. Recent changes in tropospheric water vapor over the Arctic as assessed from radiosondes and atmospheric reanalyses. J. Geophys. Res. Atmos. 117 (D10). https://doi.org/10.1029/2011JD017421.
Shao, Y., Klose, M., Wyrwoll, K.H., 2013. Recent global dust trend and connections to climate forcing. J. Geophys. Res. Atmos. 118 (19). https://doi.org/10.1002/jgrd.50836, 11,107-11,118.
Shaw, T.A., Miyawaki, O., Donohoe, A., 2022. Stormier Southern Hemisphere induced by topography and ocean circulation. Proc. Natl. Acad. Sci. 119 (50), e2123512119. https://doi.org/10.1073/pnas.2123512119.
Shepherd, J.G., 2009. Geoengineering the Climate: Science, Governance and Uncertainty. Royal Society. https://royalsociety.org/topics-policy/publications/2009/geoengineeringclimate/.
Shi, L., Zhang, J., Yao, F., Zhang, D., Guo, H., 2021. Drivers to dust emissions over dust belt from 1980 to 2018 and their variation in two global warming phases. Sci. Total Environ. 767, 144860. https://doi.org/10.1016/j.scitotenv.2020.144860.
Sledd, A., L'Ecuyer, T., 2019. How much do clouds mask the impacts of Arctic Sea ice and snow cover variations? Different perspectives from observations and reanalyses. Atmosphere 10 (1), 12. https://doi.org/10.3390/atmos10010012.
Smeed, D.A., Josey, S., Beaulieu, C., Johns, W., Moat, B.I., Frajka-Williams, E., Rayner, D., Meinen, C.S., Baringer, M.O., Bryden, H.L., 2018. The North Atlantic Ocean is in a state of reduced overturning. Geophys. Res. Lett. 45 (3), 1527–1533. https://doi.org/10.1002/2017GL076350.
Smith, G.L., Rutan, D., Charlock, T.P., Bess, T.D., 1990. Annual and interannual variations of absorbed solar radiation based on a 10-year data set. J. Geophys. Res. Atmos. 95 (D10), 16639–16652. https://doi.org/10.1029/JD095iD10p16639.
Södergren, A.H., McDonald, A.J., 2022. Quantifying the role of atmospheric and surface albedo on polar amplification using satellite observations and CMIP6 model output. J. Geophys. Res. Atmos. 127 (12). https://doi.org/10.1029/2021jd035058.
Spiegel, D.S., Menou, K., Scharf, C.A., 2008. Habitable climates. Astrophys. J. 681 (2), 1609. https://doi.org/10.1086/588089.
Stephens, G.L., O'Brien, D., Webster, P.J., Pilewski, P., Kato, S., Li, J.-L., 2015. The albedo of Earth. Rev. Geophys. 53 (1), 141–163. https://doi.org/10.1002/2014rg000449.
Stephens, G.L., Hakuba, M.Z., Hawcroft, M., Haywood, J.M., Behrangi, A., Kay, J.E., Webster, P.J., 2016. The curious nature of the hemispheric symmetry of the Earth's water and energy balances. Curr. Clim. Chang. Rep. 2, 135–147. https://doi.org/10.1007/s40641-016-0043-9.
Stephens, G.L., Hakuba, M.Z., Kato, S., Gettelman, A., Dufresne, J.-L., Andrews, T., Cole, J.N., Willen, U., Mauritsen, T., 2022. The changing nature of Earth's reflected sunlight. Proc. Royal Soc. A. 478 (2263), 20220053. https://doi.org/10.1098/rspa.2022.0053.
Stevens, B., Schwartz, S.E., 2012. Observing and modeling Earth's energy flows. Surv. Geophys. 33, 779–816. https://doi.org/10.1007/s10712-012-9184-0.
Su, W., Corbett, J., Eitzen, Z., Liang, L., 2015. Next-generation angular distribution models for top-of-atmosphere radiative flux calculation from CERES instruments: Methodology. Atmos. Meas. Tech. 8 (2), 611–632. https://doi.org/10.5194/amt-8-611-2015.
Sud, Y., Smith, W., 1985. Influence of local land-surface processes on the Indian monsoon: a numerical study. J. Appl. Meteorol. Climatol. 24 (10), 1015–1036. https://doi.org/10.1175/1520-0450(1985)024%3C1015:IOLLSP%3E2.0.CO;2.
Sumata, H., de Steur, L., Divine, D.V., Granskog, M.A., Gerland, S., 2023. Regime shift in Arctic Ocean sea ice thickness. Nature 615 (7952), 443–449. https://doi.org/10.1038/s41586-022-05686-x.
Sun, W., Videen, G., Kato, S., Lin, B., Lukashin, C., Hu, Y., 2011. A study of subvisual clouds and their radiation effect with a synergy of CERES, MODIS, CALIPSO, and AIRS data. J. Geophys. Res. Atmos. 116 (D22). https://doi.org/10.1029/2011JD016422.
Swart, N.C., Gille, S.T., Fyfe, J.C., Gillett, N.P., 2018. Recent Southern Ocean warming and freshening driven by greenhouse gas emissions and ozone depletion. Nat. Geosci. 11 (11), 836–841. https://doi.org/10.1038/s41561-018-0226-1.
Sweeney, A.J., Fu, Q., Po-Chedley, S., Wang, H., Wang, M., 2023. Internal variability increased Arctic amplification during 1980–2022. Geophys. Res. Lett. 50 (24), e2023GL106060. https://doi.org/10.1029/2023GL106060.
Tang, Z., Tian, J., Zhang, Y., Zhang, X., Zhang, J., Ma, N., Li, X., Song, P., 2022. Anthropogenic aerosols dominated the decreased solar radiation in eastern China over the last five decades. J. Clean. Prod. 380, 135150. https://doi.org/10.1016/j.jclepro.2022.135150.
Tao, M., Wang, L., Chen, L., Wang, Z., Tao, J., 2020. Reversal of aerosol properties in Eastern China with rapid decline of anthropogenic emissions. Remote Sens 12 (3), 523. https://doi.org/10.3390/rs12030523.
Taylor, K., Crucifix, M., Braconnot, P., Hewitt, C., Doutriaux, C., Broccoli, A., Mitchell, J., Webb, M., 2007. Estimating shortwave radiative forcing and response in climate models. J. Clim. 20 (11), 2530–2543. https://doi.org/10.1175/JCLI4143.1.
Thompson, S.L., Barron, E.J., 1981. Comparison of cretaceous and present earth albedos: Implications for the causes of paleoclimates. J. Geol. 89 (2), 143–167. https://doi.org/10.1086/628577.
Tie, X., Cao, J., 2009. Aerosol pollution in China: present and future impact on environment. Particuology 7 (6), 426–431. https://doi.org/10.1016/j.partic.2009.09.003.
Tomasi, C., Petkov, B., Stone, R.S., Benedetti, E., Vitale, V., Lupi, A., Mazzola, M., Lanconelli, C., Herber, A., von Hoyningen-Huene, W., 2010. Characterizing polar atmospheres and their effect on Rayleigh-scattering optical depth. J. Geophys. Res. Atmos. 115 (D2). https://doi.org/10.1029/2009JD012852.
Trenberth, K.E., 2015. Has there been a hiatus? Science 349 (6249), 691–692. https://doi.org/10.1126/science.aac9225.
Trenberth, K.E., Fasullo, J.T., 2009. Global warming due to increasing absorbed solar radiation. Geophys. Res. Lett. 36 (7). https://doi.org/10.1029/2009GL037527.
Trenberth, K.E., Fasullo, J.T., 2010. Simulation of present-day and twenty-first-century energy budgets of the southern oceans. J. Clim. 23 (2), 440–454. https://doi.org/10.1175/2009JCLI3152.1.
Trenberth, K.E., Fasullo, J.T., Balmaseda, M.A., 2014. Earth's energy imbalance. J. Clim. 27 (9), 3129–3144. https://doi.org/10.1175/JCLI-D-13-00294.1.
Trlica, A., Hutyra, L., Schaaf, C., Erb, A., Wang, J., 2017. Albedo, land cover, and daytime surface temperature variation across an urbanized landscape. Earth's Future 5 (11), 1084–1101. https://doi.org/10.1002/2017EF000569.
Tselioudis, G., Rossow, W.B., Bender, F., Oreopoulos, L., Remillard, J., 2024. Oceanic cloud trends during the satellite era and their radiative signatures. Clim. Dyn. 62 (9), 9319–9332. https://doi.org/10.1007/s00382-024-07396-8.
Tsushima, Y., Emori, S., Ogura, T., Kimoto, M., Webb, M., Williams, K., Ringer, M., Soden, B., Li, B., Andronova, N., 2006. Importance of the mixed-phase cloud distribution in the control climate for assessing the response of clouds to carbon dioxide increase: a multi-model study. Clim. Dyn. 27, 113–126. https://doi.org/10.1007/s00382-006-0127-7.
Turner, J., Holmes, C., Caton Harrison, T., Phillips, T., Jena, B., Reeves-Francois, T., Fogt, R., Thomas, E.R., Bajish, C., 2022. Record low Antarctic Sea ice cover in February 2022. Geophys. Res. Lett. 49 (12), e2022GL098904. https://doi.org/10.1029/2022GL098904.
Twomey, S., 1974. Pollution and the planetary albedo. Atmos. Environ. (1967). 8 (12), 1251–1256. https://doi.org/10.1016/0004-6981(74)90004-3.
Twomey, S., 1977. The influence of pollution on the shortwave albedo of clouds. J. Atmos. Sci. 34 (7), 1149–1152. https://doi.org/10.1175/1520-0469(1977)034<1149:TIOPOT>2.0.CO;2.
Upadhyay, R.K., 2020. Markers for global climate change and its impact on social, biological and ecological systems: a review. Am. J. Clim. Chang. 9 (03), 159. https://doi.org/10.4236/ajcc.2020.93012.
Vignesh, P.P., Jiang, J.H., Kishore, P., Su, H., Smay, T., Brighton, N., Velicogna, I., 2020. Assessment of CMIP6 cloud fraction and comparison with satellite observations. Earth Space Sci. 7 (2), e2019EA000975. https://doi.org/10.1029/2019EA000975.
Voigt, A., Stevens, B., Bader, J., Mauritsen, T., 2013. The observed hemispheric symmetry in reflected shortwave irradiance. J. Clim. 26 (2), 468–477. https://doi.org/10.1175/JCLI-D-12-00132.1.
Voigt, A., Stevens, B., Bader, J., Mauritsen, T., 2014. Compensation of hemispheric albedo asymmetries by shifts of the ITCZ and tropical clouds. J. Clim. 27 (3), 1029–1045. https://doi.org/10.1175/JCLI-D-13-00205.1.
Von Schuckmann, K., Palmer, M., Trenberth, K.E., Cazenave, A., Chambers, D., Champollion, N., Hansen, J., Josey, S., Loeb, N., Mathieu, P.-P., 2016. An imperative to monitor Earth's energy imbalance. Nat. Clim. Chang. 6 (2), 138–144. https://doi.org/10.1038/NCLIMATE2876.
Vonder Haar, T.H., Suomi, V.E., 1971. Measurements of the earth's radiation budget from satellites during a five-year period. Part I: Extended time and space means. J. Atmos. Sci. 28 (3), 305–314. https://doi.org/10.1175/1520-0469(1971)028<0305:MOTERB>2.0.CO;2.

Wang, H., Su, W., 2013. Evaluating and understanding top of the atmosphere cloud radiative effects in Intergovernmental Panel on climate Change (IPCC) Fifth Assessment Report (AR5) coupled Model Intercomparison Project phase 5 (CMIP5) models using satellite observations. J. Geophys. Res. Atmos. 118 (2), 683–699. https://doi.org/10.1029/2012JD018619.

Wang, Y., Huang, X., Liang, H., Sun, Y., Feng, Q., Liang, T., 2018. Tracking snow variations in the Northern Hemisphere using multi-source remote sensing data (2000–2015). Remote Sens 10 (1), 136. https://doi.org/10.3390/rs10010136.

Wang, X., Liu, Y., Key, J.R., Dworak, R., 2022. A new perspective on four decades of changes in Arctic Sea ice from satellite observations. Remote Sens 14 (8), 1846. https://doi.org/10.3390/rs14081846.

Wang, Y., Li, J., Fang, F., Zhang, P., He, J., Pöhlker, M.L., Henning, S., Tang, C., Jia, H., Wang, Y., 2024. In-situ observations reveal weak hygroscopicity in the Southern Tibetan Plateau: implications for aerosol activation and indirect effects. npj Clim. Atmos. Sci. 7 (1), 77. https://doi.org/10.1038/s41612-024-00629-x.

Watson-Parris, D., Christensen, M.W., Laurenson, A., Clewley, D., Gryspeerdt, E., Stier, P., 2022. Shipping regulations lead to large reduction in cloud perturbations. Proc. Natl. Acad. Sci. 119 (41), e2206885119. https://doi.org/10.1073/pnas.2206885119.

Wegener, A., Vogel, A., 1980. Die entstehung der kontinente und ozeane. Walter de Gruyter GmbH & Co KG.

Weijer, W., Cheng, W., Drijfhout, S.S., Fedorov, A.V., Hu, A., Jackson, L.C., Liu, W., McDonagh, E.L., Mecking, J.V., Zhang, J., 2019. Stability of the Atlantic Meridional Overturning Circulation: a review and synthesis. J. Geophys. Res.: Oceans. 124 (8), 5336–5375. https://doi.org/10.1029/2019JC015083.

Wielicki, B.A., Barkstrom, B.R., Harrison, E.F., Lee III, R.B., Smith, G.L., Cooper, J.E., 1996. Clouds and the Earth's Radiant Energy System (CERES): An earth observing system experiment. Bull. Am. Meteorol. Soc. 77 (5), 853–868. https://doi.org/10.1175/1520-0477(1996)077<0853:CATERE>2.0.CO;2.

Wielicki, B.A., Wong, T., Loeb, N., Minnis, P., Priestley, K., Kandel, R., 2005. Changes in Earth's albedo measured by satellite. Science 308 (5723), 825. https://doi.org/10.1126/science.1106484.

Wigley, T.M., 2006. A combined mitigation/geoengineering approach to climate stabilization. Science 314 (5798), 452–454. https://doi.org/10.1126/science.1131728.

Wild, M., Liepert, B., 2010. The Earth radiation balance as driver of the global hydrological cycle. Environ. Res. Lett. 5 (2), 025203. https://doi.org/10.1088/1748-9326/5/2/025203.

Wilson, C., Mitchell, J., 1986. Diurnal variation and cloud in a general circulation model. Q. J. R. Meteorol. Soc. 112 (472), 347–369. https://doi.org/10.1002/qj.49711247205.

Wood, R., 2012. Stratocumulus clouds. Mon. Weather Rev. 140 (8), 2373–2423. https://doi.org/10.1175/MWR-D-11-00121.1.

Woods, A.D., 2005. Paleoceanographic and paleoclimatic context of early Triassic time. C.R. Palevol. 4 (6–7), 463–472. https://doi.org/10.1016/j.crpv.2005.07.003.

Wu, D.L., Lee, J.N., Kim, K.-M., Lim, Y.-K., 2020. Interannual variations of TOA albedo over the Arctic, Antarctic and Tibetan plateau in 2000–2019. Remote Sens 12 (9), 1460. https://doi.org/10.3390/rs12091460.

Xiao, D., Ren, H.-L., 2023. A regime shift in North Pacific annual mean sea surface temperature in 2013/14. Front. Earth Sci. 10, 987349. https://doi.org/10.3389/feart.2022.987349.

Yamamoto, A.L.C., Corrêa, M.D.P., Torres, R.R., Martins, F.B., Godin-Beekmann, S., 2024. Total ozone content, total cloud cover, and aerosol optical depth in CMIP6: simulations performance and projected changes. Theor. Appl. Clim. 155 (3), 2453–2471. https://doi.org/10.1007/s00704-023-04821-6.

Yan, X.H., Boyer, T., Trenberth, K., Karl, T.R., Xie, S.P., Nieves, V., Tung, K.K., Roemmich, D., 2016. The global warming hiatus: Slowdown or redistribution? Earth's Future 4 (11), 472–482. https://doi.org/10.1002/2016EF000417.

Yang, K., Koike, T., Fujii, H., Tamura, T., Xu, X., Bian, L., Zhou, M., 2004. The daytime evolution of the atmospheric boundary layer and convection over the Tibetan Plateau: observations and simulations. J. Meteorol. Soc. Japan. Ser. II. 82 (6), 1777–1792. https://doi.org/10.2151/jmsj.82.1777.

Yang, Y., Zhao, C., Fan, H., 2020. Spatiotemporal distributions of cloud properties over China based on Himawari-8 advanced Himawari imager data. Atmos. Res. 240, 104927. https://doi.org/10.1016/j.atmosres.2020.104927.

Yang, X., Zhao, C., Yang, Y., Fan, H., 2021. Long-term multi-source data analysis about the characteristics of aerosol optical properties and types over Australia. Atmos. Chem. Phys. 21 (5), 3803–3825. https://doi.org/10.5194/acp-21-3803-2021.

Yao, B., Liu, C., Yin, Y., Liu, Z., Shi, C., Iwabuchi, H., Weng, F., 2020. Evaluation of cloud properties from reanalyses over East Asia with a radiance-based approach. Atmos. Meas. Tech. 13 (3), 1033–1049. https://doi.org/10.5194/amt-13-1033-2020.

Yin, J., Porporato, A., 2017. Diurnal cloud cycle biases in climate models. Nat. Commun. 8 (1), 2269. https://doi.org/10.1038/s41467-017-02369-4.

Young, G.H., McCarroll, D., Loader, N.J., Kirchhefer, A.J., 2010. A 500-year record of summer near-ground solar radiation from tree-ring stable carbon isotopes. The Holocene 20 (3), 315–324. https://doi.org/10.1177/0959683609351902.

Young, G.H., Gagen, M.H., Loader, N.J., McCarroll, D., Grudd, H., Jalkanen, R., Kirchhefer, A., Robertson, I., 2019. Cloud cover feedback moderates Fennoscandian summer temperature changes over the past 1,000 years. Geophys. Res. Lett. 46 (5), 2811–2819. https://doi.org/10.1029/2018GL081046.

Yu, H., Yang, Y., Wang, H., Tan, Q., Chin, M., Levy, R.C., Remer, L.A., Smith, S.J., Yuan, T., Shi, Y., 2020. Interannual variability and trends of combustion aerosol and dust in major continental outflows revealed by MODIS retrievals and CAM5 simulations during 2003–2017. Atmos. Chem. Phys. 20 (1), 139–161. https://doi.org/10.5194/acp-20-139-2020.

Yuan, T., Song, H., Wood, R., Wang, C., Oreopoulos, L., Platnick, S.E., von Hippel, S., Meyer, K., Light, S., Wilcox, E., 2022. Global reduction in ship-tracks from sulfur regulations for shipping fuel. Sci. Adv. 8 (29), eabn7988. https://doi.org/10.1126/sciadv.abn7988.

Zarnetske, P.L., Gurevitch, J., Franklin, J., Groffman, P.M., Harrison, C.S., Hellmann, J. J., Hoffman, F.M., Kothari, S., Robock, A., Tilmes, S., 2021. Potential ecological impacts of climate intervention by reflecting sunlight to cool Earth. Proc. Natl. Acad. Sci. 118 (15), e1921854118. https://doi.org/10.1073/pnas.1921854118.

Zeng, N., Yoon, J., 2009. Expansion of the world's deserts due to vegetation-albedo feedback under global warming. Geophys. Res. Lett. 36 (17). https://doi.org/10.1029/2009GL039699.

Zhang, Y., Rossow, W., 1997. Estimating meridional energy transports by the atmospheric and oceanic general circulations using boundary fluxes. J. Clim. 10 (9), 2358–2373. https://doi.org/10.1175/1520-0442(1997)010<2358:EMETBT>2.0.CO;2.

Zhang, R., Wang, H., Fu, Q., Rasch, P.J., Wang, X., 2019. Unraveling driving forces explaining significant reduction in satellite-inferred Arctic surface albedo since the 1980s. Proc. Natl. Acad. Sci. 116 (48), 23947–23953. https://doi.org/10.1073/pnas.1915258116.

Zhao, B., Jiang, J.H., Gu, Y., Diner, D., Worden, J., Liou, K.-N., Su, H., Xing, J., Garay, M., Huang, L., 2017. Decadal-scale trends in regional aerosol particle properties and their linkage to emission changes. Environ. Res. Lett. 12 (5), 054021. https://doi.org/10.1088/1748-9326/aa6cb2.

Zhao, Y., Xin, Z., Ding, G., 2018. Spatiotemporal variation in the occurrence of sand-dust events and its influencing factors in the Beijing-Tianjin Sand Source Region, China, 1982–2013. Reg. Environ. Chang. 18, 2433–2444. https://doi.org/10.1007/s10113-018-1365-z.

Zhao, C., Chen, Y., Li, J., Letu, H., Su, Y., Chen, T., Wu, X., 2019. Fifteen-year statistical analysis of cloud characteristics over China using Terra and Aqua Moderate Resolution Imaging Spectroradiometer observations. Int. J. Climatol. 39 (5), 2612–2629. https://doi.org/10.1002/joc.5975.

Zheng, B., Tong, D., Li, M., Liu, F., Hong, C., Geng, G., Li, H., Li, X., Peng, L., Qi, J., 2018. Trends in China's anthropogenic emissions since 2010 as the consequence of clean air actions. Atmos. Chem. Phys. 18 (19), 14095–14111. https://doi.org/10.5194/acp-18-14095-2018.

Zhou, C., Zelinka, M.D., Klein, S.A., 2017. Analyzing the dependence of global cloud feedback on the spatial pattern of sea surface temperature change with a G reen's function approach. J. Adv. Model. Earth Syst. 9 (5), 2174–2189. https://doi.org/10.1002/2017MS001096.

Zhou, Y., Wu, T., Zhou, Y., Zhang, J., Zhang, F., Su, X., Jie, W., Zhao, H., Zhang, Y., Wang, J., 2023. Can global warming bring more dust? Clim. Dyn. 61 (5), 2693–2715. https://doi.org/10.1007/s00382-023-06706-w.